ASSEMBLY OF GLUCOSE-DERIVED AMPHIPHILIC POLYMERS IN AQUEOUS SOLUTION: TOWARDS FUNCTIONAL AND DEGRADABLE SUPRAMOLECULAR NANOMATERIALS

A Dissertation

by

MEI DONG

Submitted to the Office of Graduate and Professional Studies of
Texas A&M University
in partial fulfillment of the requirements for the degree of

DOCTOR OF PHILOSOPHY

Chair of Committee,	Karen L. Wooley
Committee Members,	Lei Fang
	Micah J. Green
	Matthew T. Sheldon
Head of Department,	Simon W. North

December 2020

Major Subject: Chemistry

ABSTRACT

Polymer self-assembly and co-assembly have emerged as a powerful platform for the fabrication of functional nanomaterials. This dissertation research focuses on the self-assembly of degradable and functional glucose-derived polymers with high structural tailorability and complexity, as well as their co-assembly with magnetic inorganic nanoparticles towards biomedical and environmental applications.

Topological parameters in macromolecules, *e.g.*, architectures, side chain and backbone lengths, and chemical constituents, have been demonstrated to be crucial in the construction of supramolecular assemblies. Therefore, a series of amphiphilic diblock copolymers were designed and synthesized with varied architectures, chemical compositions, side chain and backbone lengths. Corresponding nanostructures with different morphologies and sizes were afforded through a solvent-exchange self-assembly process. It is found that the transition in the nanoscopic features of those nanostructures, *i.e.* morphology and size, is mostly governed by variation in the volume fraction of amphiphilic polymers.

In order to better understand the effect of fundamental molecular parameters on the supramolecular assembly of specific amphiphilic block copolymers, coil-brush block copolymer was selected as an intriguing candidate in the bottlebrush polymer family, due to its unique structure comprising of both rigid brush segments and flexible linear segments. Thus, experimental and computational self-assembly of coil-brush copolymers were studied, and found to generate two phase diagrams with a remarkable qualitative agreement, in terms of the structurally-dependent morphologies.

There has been growing interest in the fabrication of functional nanomaterials by self-assembly and co-assembly of polymers. Well-defined micellar nanocomposites prepared by hybridization of glucose-derived polycarbonates and magnetic iron oxide nanoparticles have been developed to address the crude oil contamination in aquatic environment. This functional nanomaterial is designed as a recyclable nanoscopic carrier of hydrophobic pollutants, and also able to degrade into environmentally benign small molecules in the long term.

Fundamental study of self-assembly and co-assembly behavior of amphiphilic polymers and their applications in functional material design have been discussed in this dissertation, suggesting a great potential in incorporation of various functions in nanomaterials by modification of polymer compositions and structures in a creative way.

DEDICATION

I dedicate this work to my parents and grandparents for their endless love and support, my beloved Fanglue and friends Yue and Xiaozhou for their joyful companionship during this bittersweet journey.

ACKNOWLEDGEMENTS

Firstly, I would like to sincerely thank my committee chair, Dr. Karen L. Wooley, for her continuous support and invaluable guidance for my Ph. D. study over the past five years. It's not only her insightful vision and outstanding establishment in polymer science that have a profound influence on me, but also her dedication to details and pursuit of accuracy have shaped my attitudes towards scientific research. One of the most memorable lessons that she taught me is to always dig into those tiny "unusual things", which can actually make a big difference. All the lessons, advice, praise and criticism I received from Dr. Wooley will be the lifelong gifts that I'll treasure forever.

Also, special thanks should go to my committee members, Dr. Lei Fang, Dr. Micah J. Green, and Dr. Matthew T. Sheldon for their inspirational ideas, valuable advice and kind help with my research and graduate study towards the completion of this dissertation.

Besides, this dissertation cannot be made possible without the significant contribution of many brilliant researchers, with whom I have been working for multiple collaborative projects during my entire Ph. D. study. I would like to thank (in no particular order): Dr. Arthi Jayaraman and her student Mr. Michiel G. Wessels for their great contribution in simulation studies; Dr. William P. Johnson and his student Mr. Cesar Ron for five years of fruitful collaboration; Dr. Darrin J. Pochan and his student Ms. Jee Young Lee for their tremendous help in cryogenic TEM imaging.

Last but not least, I'm very grateful to spend five years working with all the former and current group members within Wooley Group: Dr. Lu Su, Dr. Rachel A. Letteri, Dr. Yingchao Chen, Dr. Ashlee A. Jahnke, Mr. Justin A. Smolen, Dr. Fuwu Zhang, Dr. Xiang

Zhu, Dr. Jennifer S. Zigmond, Dr. Jeniree A. Flores Delgado, Dr. Samantha L. Kristufek, Dr. Jingwei Fan, Dr. Hai Wang, Dr. Richen Li, Dr. Xun He, Dr. Yi-Yun Tsao, Dr. Simcha E. Felder, Dr. Kevin T. Wacker, Dr. Eric E. Leonhardt, Dr. Chris H. Komatsu, Ms. Jessica H. Huang, Dr. Yue Song, Dr. Yen-Nan Lin, Dr. Nari Kang, Mr. Tan P. Nguyen, Ms. Mariela Vazquez, Mr. David K. Tran, Ms. Mahsa Minaeian, Mr. Benjamin Demor, Ms. Yidan Shen, Ms. Ching Pang, Ms. Ami Patel, Ms. Brooke Versaw, Ms. Sherry Melton.

Finally, I would like to thank my family and friends for their unconditional love and support.

CONTRIBUTORS AND FUNDING SOURCES

Contributors

This dissertation was supervised by a committee of researchers at Texas A&M University: Dr. Karen L. Wooley (advisor) of the Departments of Chemistry, Chemical Engineering, and Materials Science and Engineering; Dr. Kevin Burgess (former committee member) of the Department of Chemistry; Dr. Lei Fang (committee member) of the Departments of Chemistry and Material Science and Engineering; Dr. Micah J. Green (committee member) of the Department of Chemical Engineering; Dr. Matthew T. Sheldon (committee member) of the Departments of Chemistry and Material Science and Engineering.

In Chapter II, synthesis of monomers was performed with the help of Ms. Yidan Shen and Dr. Yue Song. Operation of tensiometer was performed with the help of Dr. Nari Kang and Ms. Yidan Shen.

In Chapter III, all the simulation work was done by Mr. Michiel G. Wessels (Department of Chemical and Biomolecular Engineering, University of Delaware). Cryogenic TEM characterization was performed by Ms. Jee Young Lee (Department of Materials Science and Engineering, University of Delaware). TEM tomography was performed by Dr. Hansoo Kim from Microscopy and Imaging Center, Texas A&M University. AFM measurements were carried out with the help of Mr. Fanglue Wu. DLS measurements were carried out with the help of Mr. Fangqing Xia. Dr. Guorong Sun and Dr. Yi-Yun Timothy Tsao are acknowledged for helpful discussions. Matrix-assisted laser desorption ionization time-of-flight mass spectrometry experiments were performed by Laboratory for Biological Mass Spectrometry of Texas A&M University.

In Chapter IV, Enbridge Energy Partners, L.P. is acknowledged for their generous donation of the West Texas crude oil, *via* Mr. Jonathan Sanders. SQUID measurements were carried out with the help of Dr. Haomiao Xie. STEM-EDS mapping studies were performed with the help of Dr. Jialuo Li and Dr. Hong-Cai Zhou.

All other work conducted for the thesis (or) dissertation was completed by the student independently.

Funding Sources

The work in Chapter II, III, IV were made possible by financial support from the National Science Foundation under grant numbers CHE-1610311, DMREF-1629094, DMREF-1629156, DMR-1507429, DMR-1905818, and the Welch Foundation through the W. T. Doherty-Welch Chair in Chemistry under grant number A-0001. We also acknowledge the support for the simulation work through the use of information technologies resources at the University of Delaware, specifically the Farber high-performance computing resources and the National Science Foundation Small Business Innovation Research (NSF-SBIR) program under grant number 1632486 and the Robert A. Welch Foundation through a Welch Endowed Chair to H.C.Z. (A-0030), which supported the STEM element mapping analyses.

NOMENCLATURE

AFM	Atomic force microscopy
$CDCl_3$	Deuterated chloroform
conc.	Concentration
conv.	Conversion
COSY	Homonuclear correlation spectroscopy
$Đ$	Dispersity index
D_{av}	Average diameter
D_2O	Deuterium oxide
DCM	Dichloromethane
$D_{\mathrm{h(number)}}$	Number-average hydrodynamic diameter
$D_{\mathrm{h(intensity)}}$	Intensity-average hydrodynamic diameter
$D_{\mathrm{h(volume)}}$	Volume-average hydrodynamic diameter
DLS	Dynamic light scattering
DMF	*N*,*N*-Dimethylformamide
DP_{n}	Degree of polymerization
DSC	Differential scanning calorimetry
ESI-MS	Electrospray ionization mass spectrometry
FT-IR (ATR)	Fourier-transform infrared (attenuated total reflection)
MALDI-Tof	Matrix-assisted laser desorption ionization time-of-flight mass spectrometry
M_{n}	Number average molar mass

$M_{\text{n, NMR}}$	Number average molar mass determined by end group analysis by ^{1}H NMR spectroscopy of the polymer
$M_{\text{n, SEC}}$	Number average molar mass determined by size exclusion chromatography
M_{w}	Weight average molar mass
MWCO	Molecular weight cutoff
NEt_3	Triethylamine
NMR	Nuclear magnetic resonance
PDLLA	Poly(D,L-lactide)s
PEG	Poly(ethylene glycol)
PGC	Poly(glucose carbonate)s
PTA	Phosphotungstic acid
ROMP	Ring-opening metathesis polymerization
ROP	Ring-opening polymerization
SEC	Size exclusion chromatography
TBD	1,5,7-Triazabicyclo[4.4.0]dec-5-ene
TEM	Transmission electron microscopy
T_{g}	Glass transition temperature
TGA	Thermogravimetric analysis
THF	Tetrahydrofuran

TABLE OF CONTENTS

LIST OF FIGURES

Page

LIST OF TABLES

Page

CHAPTER I

INTRODUCTION

Self-assembly of Amphiphilic Block Copolymers in Solutions

Molecular self-assembly is a ubiquitous process in nature and lies beneath the construction of essential structures for life.[1-2] It has long been of great interest towards a wide range of applications, such as fabrication of artificial nanostructures to mimic nature's mechanisms. Thus, both biological and synthetic building blocks, for instance, amphiphilic polymers, have undergone extensive self-assembly research.[3]

Amphiphilic block copolymers are built from two different kinds of polymer blocks covalently connected together, with an affinity for both hydrophilic and hydrophobic environments. This dual affiliation gives the amphiphilic molecules a unique preferential orientation compared with simple homopolymers.

Self-assembled amphiphilic block copolymers tend to adopt an autonomously self-organized orientation, which is attributed to a large amount of amphiphilic polymer chains oriented towards a minimal contact between blocks and adjustment to interfacial properties of the polymer-solvent system at interfaces and in bulk solutions.

The general rule governing the self-assembly behavior of well-defined amphiphilic block copolymer and resulting morphology is regarding a dimensionless "packing parameter", p,[4-7] that defined in the equation below:

$$p = \frac{v}{a_o l_c}$$

where v stands for the volume of the hydrophobic chains; a_o stands for the optimal area of the head group; and l_c stands for the length of the hydrophobic tail, as shown in **Figure I-1**. According to the reported studies,[4-7] in general, the higher the packing parameter p, the lower the curvature of the interface between hydrophilic and hydrophobic blocks. For the packing mode with a low interface curvature, it is likely to generate bilayer morphology, such as vesicles,[8] bilayer tubules,[9] octopus (or jelly fish),[8, 10] *etc*. Whereas, the extensively reported conventional spherical micelles are likely to be obtained from the amphiphilic polymers with a packing mode of a high interface curvature.

Moreover, it is reported that one of the key features for the nanoscale assemblies is their tendency to be kinetically trapped in non-equilibrium states, which means that the morphologies they adopt also highly depend on the kinetics of self-assembly process.[11] In recent years, there has been a variety of representative examples in processing approaches that offer higher level of tailorability to the nanoscopic structures.[12-17] Therefore, although it will be a challenge to determine the global equilibrium and fully explore the morphology

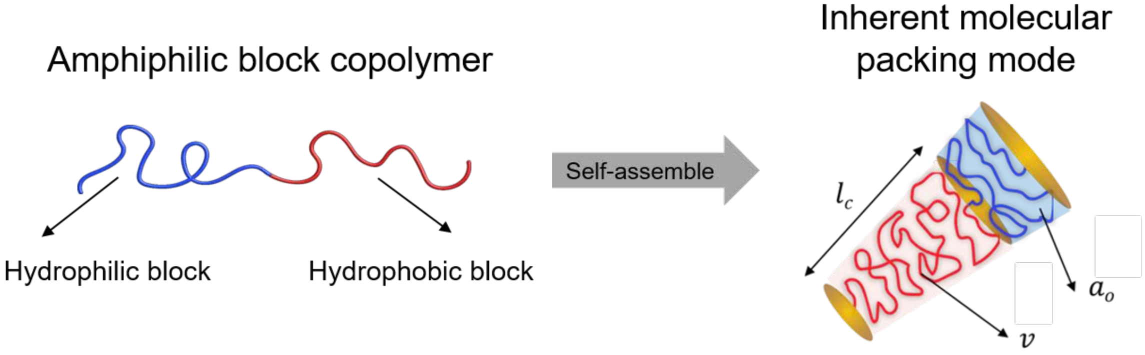

Figure I-1 Dimensionless packing parameter, $p = \frac{v}{a_o l_c}$, is defined as a measurement that indicates the inherent molecular packing mode of the self-assembled amphiphilic block copolymers library, it also offers considerable potential to tune the kinetic routes during self-assembly, thereby achieving a remarkable control over the resulting morphologies.

Self-assembly of amphiphilic polymers into nano-objects with tunable morphologies

Early assembly studies involved mostly conventional spherical nanostructures, however, there is a significant multiplicity of the possible morphologies, indicating that nanostructures assembled from amphiphilic block copolymers deserve further investigation (**Figure I-2**).[18] For examples, unique difference in blood circulation times, biodistribution, and cell internalization between nanoscopic assemblies with different morphologies have been observed.[19-21] Rod-shaped nano-objects, derived from poly(acrylic acid)-*b*-poly(*p*-hydroxystyrene) (PAA-*b*-P*p*HS), have been reported have higher capacity of doxorubicin (DOX) loading and greater extent of release under the dynamic dialysis conditions.[22] Cylindrical nanoparticle system based upon poly(acrylic acid)-*b*-poly(methyl acrylate)-*b*-polystyrene (PAA-*b*-PMA-*b*-PS) suggested to be a better

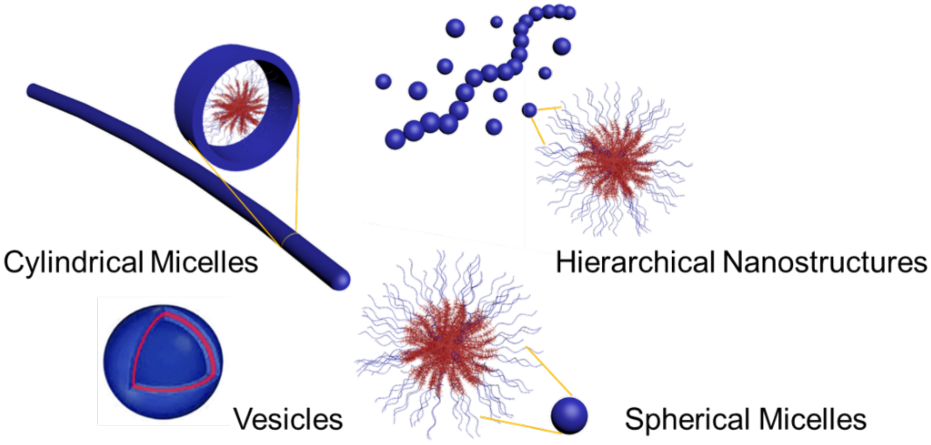

Figure I-2 Schematic illustration of diverse nanostructures obtained from self-assembly of amphiphilic copolymers candidate for cell internalization when the mechanism involved a receptor-mediated endocytic process.[20] Also, poly(L-lactide)-*b*-poly(acrylic acid) (PLLA-*b*-PAA) cylindrical micelles were fabricated with different dimensions and demonstrated to be able to induce an inflammatory response more efficiently than shorter particles and their spherical counterparts.[23] Besides, polymeric vesicles, also known as polymersomes, are self-assembled from amphiphilic block or grafted copolymers to form hollow nanostructures surrounded by a polymeric bilayer membrane or complicated interdigitated and amphiphilic membrane structures, which consist of an aqueous interior.[24] Encapsulation of both hydrophobic and hydrophilic agents, such as anticancer drugs, DNA, RNA, and vaccines, is realized by the hollow bilayer or compartmentalized structure of polymersomes for biomedical applications.[25] Therefore, manipulation of the morphology of nanostructures originating from the same parent amphiphilic block copolymer and their corresponding properties or potential applications are of great interest.

Our group has investigated the self-assembly behavior of synthetic amphiphilic polymers towards a variety of nanoscopic objects, such as spherical micelles, cylindrical nanoparticles, nanorods, Janus particles, vesicles, *etc.* SCKs,[26-27] defined as the polymeric micelles that are crosslinked through the shell region of the particle, are expected to provide stability by circumventing the limitations that the critical micelle concentration (CMC) poses. These polymeric materials have found particular interest, owing to their well-defined structures, core-shell morphology with tunable cargo-shell space and chemical functionality within a nanoscopic framework.[22] The applications of SCKs derived from various platforms mainly focus on drug loading and release, antimicrobial, environmental remediation, *etc*. The hydrophobic core facilitates encapsulation of the cargo agents, while the hydrophilic shell shields the cargo from its surroundings and provide enhanced solubility.[28] The control over the drug-release kinetics by manipulating the physical properties of the SCKs has been demonstrated.[28-30]

Bottlebrush copolymers and their self-assembly in solutions

Due to the relatively simple architecture, the self-assembled morphologies formed from linear amphiphilic block copolymers are limited to some extent. Polymers of higher complexity, such as bottlebrush polymers, dendrimeric polymers, star-shaped polymers, *etc*., are attractive candidates with tunable molecular parameters, thereby enabling controllable formation of diverse nanoscopic structures.

Notably, bottlebrush polymers are a type of grafted polymers with macromolecular side chains attached to a linear backbone.[31] Their shape-persistent nature, spatial dimensions, multicompartment structures, and tunable architectures provide access to nanostructures often unattainable from linear polymers.[32] Besides, the close proximity of side chains in cylindrical polymer brushes, particularly at high grafting densities, avoid entanglement and adopt an extended conformation, allowing access to unique polymer architectures.[33-

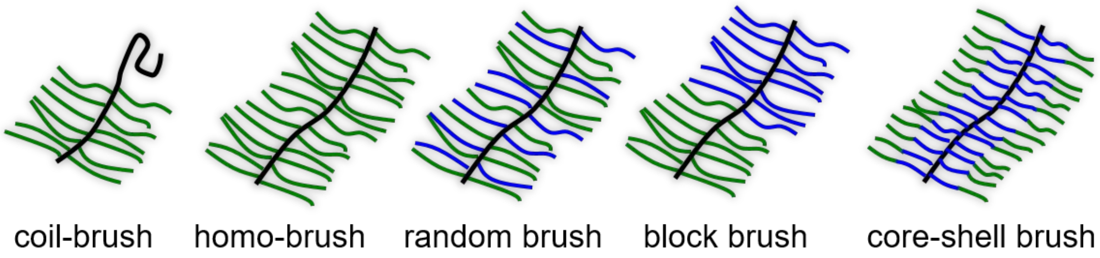

Figure I-3 Typical architectures of bottlebrush polymers

[35] Because of their extended conformation, these molecular bottlebrushes exhibit a rigid nature, therefore generating a wide spectrum of polymer building blocks with same chemical composition but distinct physicochemical property.

Similar to amphiphilic linear copolymers, amphiphilic bottlebrush copolymers are able to self-assemble into nanoscopic structures in solutions according to their amphiphilic ratio. The resulting nanostructures typically have a larger size than those obtained from linear copolymers, and also, advanced functionalities can be incorporated into the nanosegregated backbone and side chain domains, rendering the creation of complex and hierarchical nanomaterials.[31, 36]

Co-assembly of polymers and inorganic nanoparticles towards hybrid nanomaterials

Hybrid nanomaterials constructed *via* the co-assembly of functional polymers and inorganic nanoparticles are of great interest due to their size-dependent physicochemical properties and multifunctionalities. The hybridization of organic and inorganic contents on the nanoscale is often the smallest domain size possible to enable the retention of useful properties similar to the bulk state.[37] Inorganic nanoparticles have been found with diversified intriguing properties, such as optical, electrical, and magnetic properties, arising from the quantum confinement effects and surface effects brought from their unique size- and shape-dependent nature.[38-40] To enhance the structural stability of the functional inorganic nanoparticles, polymeric materials have been utilized for encapsulation of nanoparticles into their self-assembled aggregates. Therefore, by combining the functionalities from parent constituents, new properties are generated to meet further requirements in various innovative applications.[41-42] In addition to improved structural stability, there are also numerous other benefits by forming hybrid nanomaterials, such as reducing toxicity, achieving multifunctionality, improving collective properties, serving as template for cavity formation, *etc.*[41]

In order to fabricate composite nanomaterials, different constituent components and co-assembly approaches have been investigated.[43-46] During a typical co-assembly process, polymers and inorganic nanoparticles are spontaneously connected and integrated *via* specific interactions, *e.g.* hydrophobic interaction, van der Waals interaction, electrostatic interaction, molecular surface forces, entropic effects, and so forth. For instances, emulsion polymerization in presence of nanoparticles has been for encapsulation, thereby kinetically trapping numerous surface-modified iron oxide nanoparticles within the polymeric matrix during free-radical polymerization. Also, magnetic nanocomposites have also been prepared by physically loading inorganic nanoparticles, or metal salt precursors into homopolymer, or amphiphilic block copolymers assembled in solid state or solution state. Besides, core-shell nanoparticles have also been reported with distinct magnetic nanoparticles trapped inside the organic core,[47] which enables the synthesis and modification to the properties of magnetic nanocomposites by control of the copolymer shell structure and composition.

In our group, silver-polyphosphoester and silver-polylactide nanoparticles have been developed and investigated as cancer therapeutics, antimicrobial and for other biomedical applications.[48-49] While towards development of recyclable materials for remediation of water contaminated with complex pollutants, magnetic shell-crosslinked knedel-like

(MSCK) nanoparticles and magnetically active hybrid networks (MHNs) have been reported, which are fabricated from covalently or non-covalently conjugated amphiphilic PAA-*b*-PS SCK nanoparticles and magnetic iron oxide nanoparticles.[50-51]

Degradable Polymers Derived from Natural Products

Despite of all the fascinating properties shown by self-assembled polymer nanostructures and co-assembled hybrid organic-inorganic nano-objects, their long-term applications towards sustainable development of materials are highly restricted due to the toxicity of inorganic nanoparticles as well as the persistency of nondegradable polymers, which have led to severe damage to the ecosystem. Therefore, it is particularly demanding to develop and employ nontoxic inorganic nanoparticles and degradable polymer materials to construct sustainable nanomaterials for further generations.

Degradable polymer is a class of polymer that can break down into small segments when exposed to certain conditions, such as physical (*e.g.* photodegradable polymer), chemical (*e.g.* hydrolysable polymer), biological (*e.g.* biodegradable polymer) conditions, *etc*. These polymers can be both naturally and synthetically produced. Examples of natural degradable polymers include polysaccharides, proteins, *etc.* Poly(glycolic acid) and poly(lactic acid) blends used for suture and garbage bag manufacturing, respectively, are commercially available examples of synthetic polymer materials. Introducing polymer degradation into existing commercial polymers in a controllable way relieves the threat to the environment, brought by the persistent nondegradable polymers.

Various examples of synthesis of polymeric materials originating from natural products have been designed through synthetic organic chemical transformations, *i.e.* functional group interconversion, protection/deprotection series, or installation of functional groups.[52-55] Our group has been actively devoted to design and develop degradable and biocompatible polymers originated from natural products, such as neolignan polymers derived from honokiol and magnolol,[56] quercetin-based polymers,[57] polycarbonates derived from quinic acid,[58] *etc.* Recently, an organocatalyzed ring-opening polymerization methodology was developed for preparation of polycarbonates derived from glucose.[59-62] These sugar-based polycarbonates are of great interest as engineer materials owing to their origination from renewable resources as well as their potential to carry additional functionality and relatively high glass transition temperatures.[63-66]

Scope of this Dissertation

The overall emphasis of this dissertation is to design and develop functional and degradable nanomaterials by self-assembly or co-assembly of the glucose-derived amphiphilic block copolymers and magnetic inorganic nanoparticles. An integrated study of polymer synthesis, self-assembly and co-assembly in aqueous solutions, nanomaterial characterization and data analysis has been done.

In Chapter II, a series of bottlebrush polymers with varied side chain length, backbone length, side chain chemistry as well as macromolecular architecture were designed and synthesized by a combination of “grafting-through” and “grafting to” polymerization strategies, followed by the investigation of their self-assembly behaviors mainly by TEM and DLS measurements. Diverse supramolecular nanostructures were afforded owing to the significant control over dimensional structures of bottlebrush block copolymers. It was found that variation of the volume fraction dictated the morphology transition of the nanostructures obtained from those amphiphilic bottlebrush block copolymers. In addition, PGC and PDLLA were utilized as building blocks for the construction of degradable and biocompatible nanomaterials with a potential to break down into natural by-products. Their structural and spatial differences also affect the resulting morphology of the corresponding self-assembled amphiphilic bottlebrushes.

In Chapter III, we investigated the fundamental molecular parameters that guide the supramolecular assembly of glucose-based amphiphilic coil-brush block polymers in aqueous solution and elucidated architecture-morphology relationships through experimental and simulation tools. Well-defined coil-brush polymers were synthesized through ring-opening polymerizations (ROP) of glucose carbonates to afford norbornenyl-functionalized poly(glucose carbonate) (NB-PGC) macromonomers, followed by sequential ring-opening metathesis polymerizations (ROMP) of norbornene *N*-hydroxysuccinimidyl (NHS) esters and the NB-PGC macromonomers. Variation of the macromonomer length and grafting through ROMP conditions allowed for a series of coil-brush polymers to be synthesized with differences in the brush and coil dimensions, independently, where the side-chain graft length and brush backbone were used to tune the brush, and the coil block length was used to vary the coil. Hydrolysis of the NHS moieties gave the amphiphilic coil-brush polymers, where the hydrophilic-hydrophobic ratios were dependent on the brush and coil relative dimensions. Experimental assembly in solution was studied and found to yield a variety of structurally-dependent nanostructures. Simulations were conducted on the solution assembly of coil-brush polymers, where the polymers were represented by a coarse-grained model and the solvent represented implicitly. There is qualitative agreement in the phase diagrams obtained from simulations and experiments, in terms of the morphologies of the assembled nanoscopic structures achieved as a function of coil-brush design parameters (*e.g.*, brush and coil lengths, composition). The simulations further showed the chain conformations adopted by the coil-brush polymers and the packing within these assembled nanoscopic structures. This work enables the predictive design of nanostructures from this glucose-based coil-brush polymer platform while providing a fundamental understanding of interactions within solution assembly of complex polymer building blocks.

In Chapter IV, we designed and fabricated a nanoscopic sugar-based magnetic hybrid material that is capable of tackling environmental pollution posed by marine oil spills, while minimizing potential secondary problems that may occur from microplastic contamination. These readily-defined magnetic nanocomposites were constructed through co-assembly of magnetic iron oxide nanoparticles (MIONs) and a degradable amphiphilic polymer, poly(ethylene glycol)-*b*-dopamine-functionalized poly(ethyl propargyl glucose carbonate)-*b*-poly(ethyl glucose carbonate), PEG-*b*-PGC[(EPC-MPA)-*co*-(EPC-DOPA)]-*b*-PGC(EC), driven by supramolecular co-assembly in water with enhanced interactions provided *via* complexation between dopamine and MIONs. The composite nanoscopic assemblies possessed a *pseudo*-micellar structure, with MIONs trapped within the polymer framework. The triblock terpolymer was synthesized by sequential ring-opening polymerizations (ROPs) of two glucose-derived carbonate monomers, initiated by a PEG macroinitiator. Dopamine anchoring groups were subsequently installed by first introducing carboxylic acid groups using a thiol-yne click reaction, followed by amidation with dopamine. The resulting amphiphilic triblock terpolymers and MIONs were co-assembled to afford hybrid nanocomposites using solvent exchange processes from organic solvent to water. In combination with hydrophobic interactions, the linkage between dopamine and iron oxide stabilized the overall nanoscopic structure to allow for the establishment of a uniform globular morphology, whereas attempts at co-assembly with the triblock terpolymer precursor, lacking dopamine side chains, failed to afford well-defined nanostructures. The magnetic hybrid nanoparticles demonstrated high oil sorption capacities, *ca.* 8 times their initial dry weight, attributed, in part, to large surface areas leading to effective contact between the nanomaterials and hydrocarbon pollutants. Moreover, the naturally-derived polymer framework undergoes hydrolytic degradation to break down into byproducts that include glucose, ethanol and dopamine if not recovered after deployment, alleviating concerns of potential microplastic generation and persistence.

CHAPTER II

SELF-ASSEMBLY BEHAVIOR OF GLUCOSE- AND LACTIDE-BASED LINEAR, STAR-SHAPED, AND BOTTLEBRUSH AMPHIPHILIC BLOCK COPOLYMERS

Introduction

Functional bottlebrush polymers, or molecular brushes, have gained great attention in recent years because of their unique physiochemical properties and supramolecular assembly behaviors.[33-34, 67] Towards the synthesis of theses macromolecules, three representative approaches, *i.e.*, “grafting-through”, “grafting-onto”, and “grafting-from”, have been developed to achieve well-defined bottlebrush polymers. By employing pre-synthesized macromonomers containing a polymerizable chain end, “grafting-through” strategy has its particular advantages on significant structural control and quantitative grafting efficiency throughout the entire macromolecular framework. Bottlebrush polymers prepared by this approach possess uniform polymeric side chains and 100% grafting density, leading to well-controlled chemical compositions and relative concentric and lengthwise dimensions.[67] One typical synthetic strategy for grafting-through approach is ring-opening metathesis polymerization (ROMP), by which norbornenyl-ended macromonomers are polymerized with highly reactive and broad functional group tolerant ruthenium-based catalyst (Grubbs G3 catalyst) in a well-controlled manner to yield complex polymers with specific topological control.[68-69] Besides, “Grafting-to” approach has not been widely reported for the synthesis of the molecular brushes since the steric congestion causes difficulty in affording high grafting density.[70] However, a reactive polymeric side chain with a “slimmer” structure, *e.g.* poly(ethylene glycol) (PEG) and a highly reactive "grafting site" are likely to help decrease the steric hindrance and assure a efficient coupling reaction, thereby affording a versatile platform for post-polymerization modification.

Owing to the unique architecture of bottlebrush polymers, especially as multicompartment nanomaterials, amphiphilicity can be imparted in deferent ways, such as core-shell, Janus-like, blocky, *etc.* There is increasing exploitation of such macromolecular architectures for the preparation of soft material.[71] Previously, Neiser *et al.* had used giant rod-coil amphiphilic block copolymers to achieve micelle formation.[72] Li *et al.* reported the synthesis of poly(acrylic acid) and polystyrene-containing bottlebrush amphiphiles with core-shell and blocky architectures, and investigated their self-assembly in aqueous solutions.[73-74] Fenyves *et al.* demonstrated shape-dependent aqueous assembly of nonionic bottlebrush block copolymer surfactants containing hydrophilic poly(ethylene oxide) (PEO) and hydrophobic polylactide (PLA) branches.[71] Bottlebrush symmetry was varied modularly through synthetic strategy, affording uniform spherical as well as long cylindrical micelles, which is imaged by cryogenic transmission electron microscopy (cryo-TEM), providing a better correlation between molecular shape and observed morphologies. The shape-morphology relationships become an advantageous tool guiding the rational design and fabrication of highly tunable nanostructures. Besides, the demonstrated biodegradability of PGC and PDLLA as well as biocompatibility of PEO own advantages towards biomedical applications.

In order to better understand the effect of each topological components on their supramolecular assembly and how they coordinate with each other when dispersing in water, a series of bottlebrushes with varied side chain length, backbone length, side chain chemistry as well as macromolecular architecture were designed and synthesized. The combination of "grafting-through" and "grafting to" polymerization strategies for the hydrophobic and hydrophilic bottle brushes, respectively, provided significant structural control and facile simultaneous incorporation of multiple functional moieties. Variation of the volume fraction dictated the morphology of the nano-objects formed from the amphiphilic bottlebrushes upon assembly in aqueous solution. The construction of complex, functional nanoparticles from PGC- and PDLLA-based materials with the potential to break down into natural by-products not only provides important fundamental knowledge, but also for numerous (bio)applications, due to the inherent versatility and ease of compositional and morphological manipulation.

Materials and Methods

Materials

The bicyclic glucose-based carbonate monomer, methyl-2,3-*O*-ethyloxycarbonyl-4,6-*O*-carbonyl-α-d-glucopyranoside (GC)[75] and the Grubbs' G3 catalyst[76], were synthesized according to previously-published procedures. DL-Lactide (LA) was purchased from TCI America (Portland, OR) and purified by recrystallization from ethyl acetate. α-Methoxy-ω-amino polyethylene glycol (PEG) was purchased from Rapp Polymere GmbH (Tübingen, Germany). 1,5,7-Triazabicyclo[4.4.0]dec-5-ene (TBD) was received from TCI America (Portland, OR), degassed, and stored in a glovebox under Ar atmosphere. Other chemicals and reagents were purchased from Sigma-Aldrich, Co. (St. Louis, MO) and were used as received, unless otherwise noted. Dichloromethane (DCM) and *N*,*N*-

dimethyl formamide (DMF) were dried using a solvent purification system (J. C. Meyer Solvent Systems, Inc., Laguna Beach, CA). Nanopure water (18 MΩ·cm) was obtained from a Milli-Q water filtration system (Millipore Corp, USA). Dialysis membrane tubing with a molar mass cut off (MWCO) of 6-8 kDa was purchased from Spectrum Laboratories, Inc. (Rancho Dominguez, CA) and soaked for 5 min in nanopure water at room temperature (rt) before use. Column chromatography was performed on a CombiFlash Rf4x (Teledyne ISCO) with RediSep Rf columns (Teledyne ISCO).

Instrumentation

^{1}H NMR and ^{13}C NMR spectra were recorded on Varian Inova 500 spectrometer (Varian, Inc., Palo Alto, CA) interfaced to a UNIX computer using the VnmrJ software. Chemical shifts for ^{1}H NMR and ^{13}C NMR signals were referenced to the solvent resonance frequencies. Fourier transform infrared (FT-IR) spectra were recorded on an IR Prestige 21 system, equipped with a diamond attenuated total reflection (ATR) lens (Shimadzu Corp., Japan), and analyzed using IRsolution v. 1.40 software.

Size exclusion chromatography (SEC) was used to determine polymer molar mass and molar mass distribution (or dispersity, $Đ$). Polymer solutions were prepared at a known concentration (3-5 mg/mL) and 200 µL of an injection volume was used. After filtration through a 0.45 µm PTFE filter, the polymer samples were passed through the SEC system equilibrated at 40°C in tetrahydrofuran (THF) as the mobile phase with the flow rate of 1 mL/min. SEC was conducted on a Waters 1515HPLC (Waters Chromatography, Inc.) equipped with a differential refractive index (RI) detector (Wyatt Technology, Optilab T-rEX), a multi-angle laser light scattering (MALLS) detector (Wyatt Technology, DAWN

HELEOS II, 658 nm) using ASTRA software (Wyatt Technology; the dn/dc values of the analyzed polymers were determined from the differential refractometer response based on sample concentration, assuming 100% mass recovery), and three-column series (Phenogel 5 µm; 100 Angstroms (Å), 104 Å, and Linear (2); 300×4.6 millimeters (mm) columns; Phenomenex, Inc.).

Glass transition temperatures (T_g) were measured by differential scanning calorimetry (DSC) on a Mettler-Toledo DSC3/700/1190 (Mettler-Toledo, Inc., Columbus, OH) under a nitrogen gas atmosphere. Measurements were performed with a heating and cooling rate of 10 °C/min, and three heating and cooling cycles were conducted. Measurements were analyzed using Mettler-Toledo STAR^e v. 15.00a software. The T_g was taken as the midpoint of the inflection tangent of the third heating scan.

Thermogravimetric analysis (TGA) was performed under Ar atmosphere using a Mettler-Toledo TGA2/1100/464, with a heating rate of 10 °C/min. Data were analyzed using Mettler-Toledo STAR^e v. 15.00a software.

Transmission electron microscopy (TEM) images were collected on a JEOL 1200EX operated at 100 kV, and micrographs were recorded using an SIA-15C CCD camera. Samples for TEM were prepared as follows: 20 µL of polymer solution in nanopure water (1 mg/mL) was deposited onto a carbon-coated copper grid, and after 1 min, excess solution was quickly wicked away by a piece of filter paper. The samples were then negatively stained with a 1 wt% phosphotungstic acid (PTA) aqueous solution (20 µL). After 30 s, excess staining solution was quickly wicked away by a piece of filter paper and the samples were left to dry under ambient conditions prior to imaging.

Dynamic light scattering (DLS) measurements were conducted using a Zetasizer Nano ZS instrument (Malvern Panalytical Ltd., Malvern, United Kingdom) equipped with a laser diode operating at 633 nm. Scattered light was detected at 175° and analyzed using a log correlator for a 0.5 mL of sample in a disposable cell (capacity = 0.9 mL). The photomultiplier aperture and attenuator were adjusted automatically. The particle size distribution and distribution averages were calculated using particle size distribution analysis routines in Zetasizer 7.13 software. Number of accumulations and measurement duration were adjusted automatically. All measurements were repeated 3 times. The average diameter of the particles is reported as the intensity-, volume- and number-average particle diameter from three measurements.

Experimental Procedures

Synthesis of the Hydrophilic Precursor Monomer, Bicyclo[2.2.1]hept-5-ene-exo-2-carboxylic acid N-hydroxysuccinimide Ester (NB-NHS Ester). In a 25 mL Schlenk flask charged with a stir bar, the *exo*-5-norbornenecarboxylic acid (283 mg, 2.05 mmol, 1.0 eq.), *N*-hydroxysuccinimide (320 mg, 2.78 mmol, 1.4 eq.), and *N*-(3-dimethylaminopropyl)-*N*'-ethylcarbodiimide hydrochloride (EDCI·HCl) (470 mg, 3.03 mmol, 1.5 eq.) were allowed to stir in 10 mL anhydrous DCM for 20 h under nitrogen flow at room temperature. The reaction mixture was concentrated under reduced pressure, and *N*-hydroxysuccinimidyl (NHS) ester was purified by flash chromatography (100% DCM as eluent) to afford NB-NHS ester as a white powder (482 mg, 1.70 mmol, 83% yield). ^{1}H NMR (500 MHz, $CDCl_3$) δ ppm 6.19 (dd, *J* = 6, 3 Hz, 1H), 6.13 (dd, *J* = 6, 3 Hz, 1H), 3.25 (s, 1H), 2.99 (s, 1H), 2.81 (d, *J* = 4 Hz, 5H), 2.49 (dd, *J* = 9, 4 Hz, 1H), 2.03 (dt, *J* =

12, 4 Hz, 1H), 1.59 – 1.47 (m, 2H), 1.43 (d, *J* = 9 Hz, 1H). ^{13}C NMR (126 MHz, $CDCl_3$) δ ppm 171.63, 169.37, 138.62, 138.53, 135.26, 47.10, 46.39, 41.76, 40.29, 30.95, 25.61. FT-IR (ATR, cm^{-1}) 3071-2876, 1806, 1779, 1736, 1331, 1200, 1060, 947, 841, 710, 644. HRMS: calculated $[M+H]^+$ for $C_{12}H_{13}NO_4H^+$: 236.0923, found: 236.0896.

General Procedure for Synthesis of Hydrophobic PGC Macromonomers, exo-Norbornene-terminated Poly(glucose carbonate)s (NB-PGCs):

Synthesis of macromonomer NB-PGC$_{12}$. To the recrystallized glucose carbonate GC(EC) monomer (100 mg, 0.275 mmol) in DCM (1 mL) was added norbornene methanol (2.3 μL, 2.4 mg, 0.019 mmol). The catalyst 1,3,5-triazabicyclo[4.4.0]dec-5-ene (TBD) (2 mol% to monomer, 0.8 mg, 0.006 mmol) was added with stirring at -78 °C for 5 minutes. The reaction was quenched by excess amount of acetic acid in DCM. The polymer was then precipitated 3 times into ice cold diethyl ether and dried under vacuum. $M_{n\,(NMR)}$ = 4.5 kDa. ^{1}H NMR (400 MHz, $CDCl_3$) δ ppm 6.02 (t, *J* = 3.1 Hz), 5.33 – 5.12 (m), 4.99 – 4.88 (m), 4.88 – 4.71 (m), 4.71 – 4.55 (m), 4.32 – 4.17 (m), 4.15 (s), 4.20 – 4.02 (m), 4.02 – 3.93 (m), 3.38 – 3.31 (m), 1.32 – 1.17 (m).

General Procedure for Synthesis of Hydrophobic PLA Macromonomers, exo-Norbornene-terminated Poly(D,L-lactide)s (NB-PDLLAs):

Synthesis of hydrophobic macromonomer NB-g-PDLLA$_{60}$: To the d, l-lactide monomer (0.690 mmol, 100 mg) in DCM (1 mL) was added *exo*-5-norbornene-2-methanol (0.016 mmol, 2.1 mg, 2.0 μL). The catalyst 1,3,5-triazabicyclo[4.4.0]dec-5-ene (TBD) (2 mol% to monomer, 0.014 mmol, 1.9 mg) was added with stirring at -78 °C for 10 minutes. The reaction was quenched by excess amount of acetic acid in DCM and evaporated for analysis by GPC-MALLS without purification. The polymer was then precipitated 3 times into ice cold methanol and dried under vacuum. $M_{n\ (NMR)}$ = 9 kDa, $M_{n\ (SEC)}$ = 4 kDa, $M_{w\ (SEC)}$ = 6 kDa, ^{1}H NMR (400 MHz, $CDCl_3$) δ ppm 6.01 (d, J = 2 Hz), 5.10 (qd, J = 7, 4 Hz), 4.29 (q, J = 7 Hz), 1.50 (dd, J = 11, 6 Hz), 1.46 (s). ^{13}C NMR (101 MHz, $CDCl_3$) δ ppm 169.62, 169.36, 135.66, 77.35, 77.03, 76.71, 69.19, 69.02, 16.76, 16.66.

Synthesis of hydrophobic macromonomer NB-g-PDLLA$_{30}$. To the d, l-lactide monomer (100 mg, 0.690 mmol) in DCM (1 mL) was added *exo*-5-norbornene-2-methanol (0.048 mmol, 6.3 mg, 6.0 μL). The catalyst 1,3,5-triazabicyclo[4.4.0]dec-5-ene (TBD) (2 mol% to monomer, 0.014 mmol, 1.9 mg) was added with stirring at -78 °C for 10 minutes. The reaction was quenched by excess amount of acetic acid in DCM and evaporated for analysis by GPC-MALLS without purification. The polymer was then precipitated 3 times into ice cold methanol and dried under vacuum. $M_{n\ (NMR)}$ = 4 kDa, $M_{n\ (SEC)}$ = 3 kDa, $M_{w\ (SEC)}$ = 3 kDa, ^{1}H NMR (400 MHz, $CDCl_3$) δ ppm 6.01 (d, J = 2 Hz), 5.20 – 5.07 (m), 5.08 (d, J = 7 Hz), 1.50 (dd, J = 10, 6 Hz), 1.27 – 1.15 (m). ^{13}C NMR (101 MHz, $CDCl_3$) δ ppm 169.62, 169.37, 77.34, 77.03, 76.71, 69.02, 16.66.

Synthesis of macromonomer NB-PLA$_{16}$. The purchased D, L-lactide was recrystallized by dissolving in ethyl acetate and toluene mixture (yield = 50%). To the recrystallized D, L-lactide monomer (100 mg, 0.70 mmol) in DCM (1 mL) was added norbornene methanol (5.6 μL, 5.8 mg, 0.046 mmol). The catalyst 1,3,5-triazabicyclo[4.4.0]dec-5-ene (TBD) (2 mol% to monomer, 0.014 mmol, 1.94 mg) was added with stirring at -78 °C for 5 minutes. The reaction was quenched by excess amount of acetic acid in DCM. The polymer was then precipitated 3 times into ice cold diethyl ether and dried under vacuum. $M_{n\ (NMR)}$ =

2.4 kDa. ^{1}H NMR (400 MHz, $CDCl_3$) δ ppm 6.01 (t, *J* = 1.9 Hz), 5.20 – 5.03 (m), 1.56 – 1.38 (m).

General procedure for sequential ROMP of NB-NHS and NB-PGC: P(NB-NHS)$_{20}$-b-P(NB-g-PGC$_{25}$)$_{20}$. In a glove box, 200 μL of anhydrous DCM was added into vials containing NB-NHS monomer (1 mg, 4 μmol) to form a solution with a monomer concentration of 5 mg/mL. To a solution of Grubbs G3 catalyst in DCM (3.1 mg/mL, 50 μL) under argon in a glass vial capped with a septum was added the solution of NB-NHS monomer. The reaction was allowed to stir at rt for 7 min. The solution of NB-PGC$_{25}$ macromonomer (80 mg/mL) in 200 μL anhydrous DCM was then quickly added to the polymerization mixture and stirred for 45 min before by addition of an excess amount of ethyl vinyl ether. The final polymer was obtained after precipitating the reaction mixture in diethyl ether twice and dried under vacuum overnight to yield white powder (90% yield). ^{1}H NMR (500 MHz, $CDCl_3$) δ ppm 5.32 (br, $CH{=}CH$s from brush backbone), 5.02 – 4.95 (m, $CHOCH_3$ in NB-PGC units), 4.82 – 4.68 (m, $CHOCO$ in NB-PGC units), 4.34 – 4.28 (m, OCH_2CH in NB-PGC units), 4.22 – 4.15 (m, OCH_2CH_3 in NB-PGC units), 4.09 – 4.02 (m, $CHCH(CH_2)O$ in NB-PGC units), 3.46 – 3.37 (s, OCH_3 in NB-PGC units), 2.82 (br, CH_2CH_2 from NHS units), 2.25 - 2.02 (m, CH_2s from PNB backbone), 1.35 – 1.23 (m, CH_2CH_3 in NB-PGC units). ^{13}C NMR (126 MHz, $CDCl_3$) δ ppm 154.11, 154.09, 153.76, 96.36, 77.26, 77.01, 76.75, 73.69, 73.45, 72.76, 66.71, 64.76, 64.68, 64.58, 55.64, 55.43, 14.10. FT-IR (ATR, cm^{-1}) 2978, 1751, 1450, 1373, 1242, 1011, 872, 779.

General procedure for post-modification of P(NB-g-PGC)-b-P(NB-NHS) with PEG-amine: P(NB-NHS)$_{20}$-b-P(NB-g-PGC(EC)$_{25}$)$_{20}$ modified with PEG$_{45}$-amine and PEG$_{113}$-

amine. In a 20 mL flame dried vial charged with a stir bar, the polymer P(NB-NHS)$_{20}$-*b*-P(NB-*g*-PGC(EC)$_{25}$)$_{20}$ (5 mg, 0.03 µmol) and PEG$_{45}$-amine (2 mg, 1 µmol)/PEG$_{113}$-amine (5 mg, 1 µmol) was dissolved in 3 mL anhydrous DMF and *N,N*-diisopropylethylamine (DIPEA) (2 µL, 5 µmol) was added into the polymer solution. The reaction was allowed to stir under room temperature and nitrogen flow for 10 hours. The resulting solution was placed in presoaked membrane dialysis tubing (MWCO 12-14 kDa) and dialysis against nanopure water for 3 days. The grafting percentages need to be calculated by proton NMR.

PEGylation of P(NB-NHS)$_4$-b-P(NB-g-PGC$_{12}$)$_4$: In a 20 mL flame dried vial charged with a stir bar, the polymer P(NB-NHS)$_4$-*b*-P(NB-*g*-PGC$_{12}$)$_4$ (20 mg, 1.1 µmol) and mPEG$_{17}$-amine (13 mg, 17 µmol) was dissolved in 2 mL anhydrous DMF and *N,N*-diisopropylethylamine (DIPEA) (4.4 mg, 34 µmol) was added into the polymer solution. The reaction was allowed to stir under room temperature and nitrogen flow for overnight. The resulting solution was placed in presoaked membrane dialysis tubing (MWCO 12-14 kDa) and dialysis against nanopure water for 3 days. The PEGylation percentages were calculated by proton NMR as 93% for P(NB-PEG$_{17}$)$_4$-b-P(NB-g-PGC$_{12}$)$_4$. ^{1}H NMR (400 MHz, CDCl$_3$) δ ppm 5.31 (dt, *J* = 15.6, 9.5 Hz), 5.14 (t, *J* = 9.6 Hz), 4.99 (d, *J* = 15.3 Hz), 4.85 (q, *J* = 11.5, 10.9 Hz), 4.80 – 4.63 (m), 4.43 – 3.96 (m), 3.64 (s), 3.46 – 3.34 (m), 1.34 – 1.22 (m).

General Procedure for Sequential ROMP of NB-NHS ester and NB-PDLLA:

Synthesis of P(NB-NHS)$_{20}$-b-P(NB-g-PDLLA$_{30}$)$_{20}$. In the glove box, 200 µL of anhydrous DCM was added into a 4 mL shell vial containing NB-NHS monomer (1 mg, 4 µmol) to form a solution with a monomer concentration of 5 mg/mL. A green color solution of

Grubbs G3 catalyst in DCM (3.0 mg/mL, 50 μL) was added to the solution of NB-NHS monomer under argon environment, and the solution turned yellow. The reaction was allowed to stir at rt for 10 min. The solution of NB-PDLLA$_{30}$ macromonomer (100 mg/mL) in 200 μL anhydrous DCM was then quickly added to the polymerization mixture and stirred for 60 min before the addition of an excess amount of ethyl vinyl ether for quenching. The final polymer was obtained after precipitating the reaction mixture in diethyl ether twice and dried under vacuum overnight to yield white powder.

Synthesis of P(NB-NHS)$_4$-b-P(NB-g-PDLLA$_{16}$)$_4$: In a glove box, 500 μL of anhydrous DCM was added into a 4 mL shell vial containing NB-NHS monomer (2.9 mg, 13 μmol) to form a solution with a monomer concentration of 6 mg/mL. A green-color solution of Grubbs G3 catalyst (2.3 mg, 3.1 μmol) in DCM was added to the solution of NB-NHS monomer under argon environment, and the solution turned to bright yellow. The reaction was allowed to stir at rt for 6 min. The solution of NB-PLA$_{30}$ macromonomer (30 mg, 13 μmol) in 500 μL anhydrous DCM (*ca.* 60 mg/mL) was then quickly added to the polymerization mixture and stirred for 30 min before the addition of an excess amount of ethyl vinyl ether for quenching. The final polymer was obtained after precipitating the reaction mixture in diethyl ether twice and dried under vacuum overnight to yield white powder (yield = 90%). ^{1}H NMR (400 MHz, CDCl$_3$) δ ppm 5.11 (dq, *J* = 10.9, 7.0 Hz), 3.73 – 3.63 (m), 2.74 (s), 1.84 – 1.73 (m), 1.51 (t, *J* = 5.7 Hz), 1.42 (dd, *J* = 6.9, 3.4 Hz), 1.36 (s), 1.25 – 1.13 (m).

PEGylation of P(NB-NHS)$_{12}$-b-P(NB-g-PDLLA$_{30}$)$_{10}$. In a 20 mL flame dried vial charged with a stir bar, the polymer P(NB-NHS)$_{12}$-*b*-P(NB-*g*-PLA$_{30}$)$_{10}$ (3.5 mg, 0.13 μmol) and

$\mathrm{mPEG_{45}}$-amine (5.4 mg, 2.7 μmol) or $\mathrm{mPEG_{113}}$-amine (13 mg, 2.6 μmol) was dissolved in 3 mL anhydrous DMF and *N*,*N*-diisopropylethylamine (DIPEA) (0.24 mg, 2.6 μmol) was added into the polymer solution. The reaction was allowed to stir under room temperature and nitrogen flow for overnight. The resulting solution was placed in presoaked membrane dialysis tubing (MWCO 12-14 kDa) and dialysis against nanopure water for 3 days. The PEGylation percentages were calculated by proton NMR as 96% for P(NB-*g*-$\mathrm{PEG_{45}}$)$_{12}$-*b*-P(NB-*g*-$\mathrm{PLA_{30}}$)$_{10}$ and 94% for P(NB-*g*-$\mathrm{PEG_{113}}$)$_{12}$-*b*-P(NB-*g*-$\mathrm{PLA_{30}}$)$_{10}$. P(NB-*g*-$\mathrm{PEG_{45}}$)$_{12}$-*b*-P(NB-*g*-$\mathrm{PLA_{30}}$)$_{10}$: ^{1}H NMR (400 MHz, $\mathrm{CDCl_3}$) δ ppm 5.11 (dq, *J* = 11.2, 7.0 Hz), 3.58 (s), 1.51 (dd, *J* = 6.5, 1.9 Hz). P(NB-*g*-$\mathrm{PEG_{113}}$)$_{12}$-*b*-P(NB-*g*-$\mathrm{PLA_{30}}$)$_{10}$: ^{1}H NMR (400 MHz, $\mathrm{CDCl_3}$) δ ppm 5.12 (dq, *J* = 18.5, 7.1, 6.5 Hz), 3.57 (s), 1.73 – 1.31 (m).

PEGylation of P(NB-NHS)$_{12}$-b-P(NB-g-$\mathrm{PLA_{60}}$)$_{10}$. In a 20 mL flame dried vial charged with a stir bar, the polymer P(NB-NHS)$_{12}$-*b*-P(NB-*g*-$\mathrm{PLA_{30}}$)$_{10}$ (3.5 mg, 0.039 μmol) and $\mathrm{mPEG_{45}}$-amine (2.2 mg, 1.1 μmol) or $\mathrm{mPEG_{113}}$-amine (4.8 mg, 0.98 μmol) was dissolved in 3 mL anhydrous DMF and *N*,*N*-diisopropylethylamine (DIPEA) (0.10 mg, 0.78 μmol) was added into the polymer solution. The reaction was allowed to stir under room temperature and nitrogen flow for overnight. The resulting solution was placed in presoaked membrane dialysis tubing (MWCO 12-14 kDa) and dialysis against nanopure water for 3 days. The PEGylation percentages were calculated by proton NMR as 95% for P(NB-*g*-$\mathrm{PEG_{45}}$)$_{12}$-*b*-P(NB-*g*-$\mathrm{PLA_{60}}$)$_{10}$ and 95% for P(NB-*g*-$\mathrm{PEG_{113}}$)$_{12}$-*b*-P(NB-*g*-$\mathrm{PLA_{60}}$)$_{10}$. P(NB-*g*-$\mathrm{PEG_{45}}$)$_{12}$-*b*-P(NB-*g*-$\mathrm{PLA_{60}}$)$_{10}$: ^{1}H NMR (400 MHz, $\mathrm{CDCl_3}$) δ ppm 5.09

(q, J = 7.0 Hz), 3.57 (s), 1.56 – 1.45 (m). P(NB-g-PEG$_{113}$)$_{12}$-b-P(NB-g-PLA$_{60}$)$_{10}$: ^{1}H NMR (400 MHz, CDCl$_3$) δ ppm 5.17 – 5.05 (m), 3.57 (s), 1.50 (tq, J = 7.3, 4.0, 2.5 Hz).

PEGylation of P(NB-NHS)$_4$-b-P(NB-g-PLA$_{16}$)$_4$: In a 20 mL flame dried vial charged with a stir bar, the polymer P(NB-NHS)$_4$-b-P(NB-g-PLA$_{16}$)$_4$ (20 mg, 1.9 μmol) and mPEG$_{17}$-amine (23 mg, 30 μmol) was dissolved in 2 mL anhydrous DMF and N,N-diisopropylethylamine (DIPEA) (7.8 mg, 60 μmol) was added into the polymer solution. The reaction was allowed to stir under room temperature and nitrogen flow for overnight. The resulting solution was placed in presoaked membrane dialysis tubing (MWCO 12-14 kDa) and dialysis against nanopure water for 3 days. The PEGylation percentages were calculated by proton NMR as 100% for P(NB-g-PEG$_{17}$)$_4$-b-P(NB-g-PLA$_{16}$)$_4$. ^{1}H NMR (400 MHz, CDCl$_3$) δ ppm 5.09 (q, J = 7.0 Hz), 3.57 (s), 1.56 – 1.45 (m). P(NB-g-PEG$_{113}$)$_{12}$-b-P(NB-g-PLA$_{60}$)$_{10}$: ^{1}H NMR (400 MHz, CDCl$_3$) δ ppm 5.16 (q, J = 7.1 Hz), 3.65 (d, J = 5.7 Hz), 1.58 (d, J = 7.2 Hz).

Synthesis of linear diblock polymer PEG$_{113}$-b-PGC$_{50}$. To the GC(EC) monomer (55 mg, 151 μmol) in DCM (1.5 mL) was added mPEG$_{113}$-OH (3.0 μmol, 15 mg). The catalyst 1,3,5-triazabicyclo[4.4.0]dec-5-ene (TBD) (2 mol% to monomer, 3.0 μmol, 0.42 mg) was added with stirring at -78 °C for 20 minutes. The reaction was quenched by excess amount of acetic acid in DCM and evaporated for analysis by SEC without purification. The polymer was then precipitated 3 times into ice cold diethyl ether and dried under vacuum (yield = 60%). $M_{n\,(NMR)}$ = 22.8 kDa, $M_{n\,(SEC)}$ = 21.9 kDa, $M_{w\,(SEC)}$ = 23.2 kDa, ^{1}H NMR (400 MHz, CDCl$_3$) δ 5.25 (t, J = 9.7 Hz), 4.92 (d, J = 3.6 Hz), 4.74 (t, J = 9.7 Hz), 4.63

(dd, *J* = 10.3, 3.4 Hz), 4.23 (d, *J* = 11.4 Hz), 4.18 – 4.09 (m,), 4.13 – 4.03 (m), 3.56 (s), 3.33 (s), 3.38 – 3.29 (m), 3.27 (s), 1.20 (dt, *J* = 8.2, 7.1 Hz).

Synthesis of linear diblock polymer PEG_{113}-*b*-$PDLLA_{50}$. The purchased D, L-lactide was recrystallized by dissolving in ethyl acetate and toluene mixture (yield = 50%). To the recrystallized D, L-lactide monomer (35 mg, 0.24 mmol) in DCM (3 mL) was added $mPEG_{113}$-OH (5.0 μmol, 25 mg). The catalyst 1,3,5-triazabicyclo[4.4.0]dec-5-ene (TBD) (2 mol% to monomer, 5 μmol, 0.7 mg) was added with stirring at -78 °C for 4 minutes. The reaction was quenched by excess amount of acetic acid in DCM and evaporated for analysis by SEC without purification. The polymer was then precipitated 3 times into ice cold diethyl ether and dried under vacuum. $M_{n\,(NMR)}$ = 11.8 kDa, $M_{n\,(SEC)}$ = 13.2 kDa, $M_{w\,(SEC)}$ = 14.1 kDa, ^{1}H NMR (400 MHz, $CDCl_3$) δ ppm 5.27 – 5.13 (m), 3.66 (s), 3.50 (q, *J* = 7.0 Hz, 1H), 1.65 – 1.53 (m), 1.23 (t, *J* = 7.0 Hz).

Synthesis of linear diblock polymer PEG_{113}-*b*-$PDLLA_{25}$. To the recrystallized D, L-lactide monomer (18 mg, 120 μmol) in DCM (3 mL) was added $mPEG_{113}$-OH (5.0 μmol, 25 mg). The catalyst 1,3,5-triazabicyclo[4.4.0]dec-5-ene (TBD) (2 mol% to monomer, 5 μmol, 0.7 mg) was added with stirring at -78 °C for 4 minutes. The reaction was quenched by excess amount of acetic acid in DCM and evaporated for analysis by SEC without purification. The polymer was then precipitated 3 times into ice cold diethyl ether and dried under vacuum. $M_{n\,(NMR)}$ = 8.7 kDa, $M_{n\,(SEC)}$ = 9.7 kDa, $M_{w\,(SEC)}$ = 10.0 kDa, ^{1}H NMR (400 MHz, $CDCl_3$) δ ppm 5.11 (dq, *J* = 14.3, 7.1 Hz), 3.57 (s), 3.41 (q, *J* = 7.0 Hz), 1.50 (dd, *J* = 10.6, 6.1 Hz), 1.14 (t, *J* = 7.0 Hz).

Self-assembly and morphological study. Series of diblock amphiphilic polymers were dissolved in 1 mL DMF to form 1 mg/mL solutions, weighed by microbalance. Syringe pump was used to slowly add 2 mL nanopure water into the polymer-DMF solution at the rate of 2 mL/h, stir at 200 rpm, followed by dialysis against nanopure water for three days before characterization by DLS and TEM.

Results and Discussions

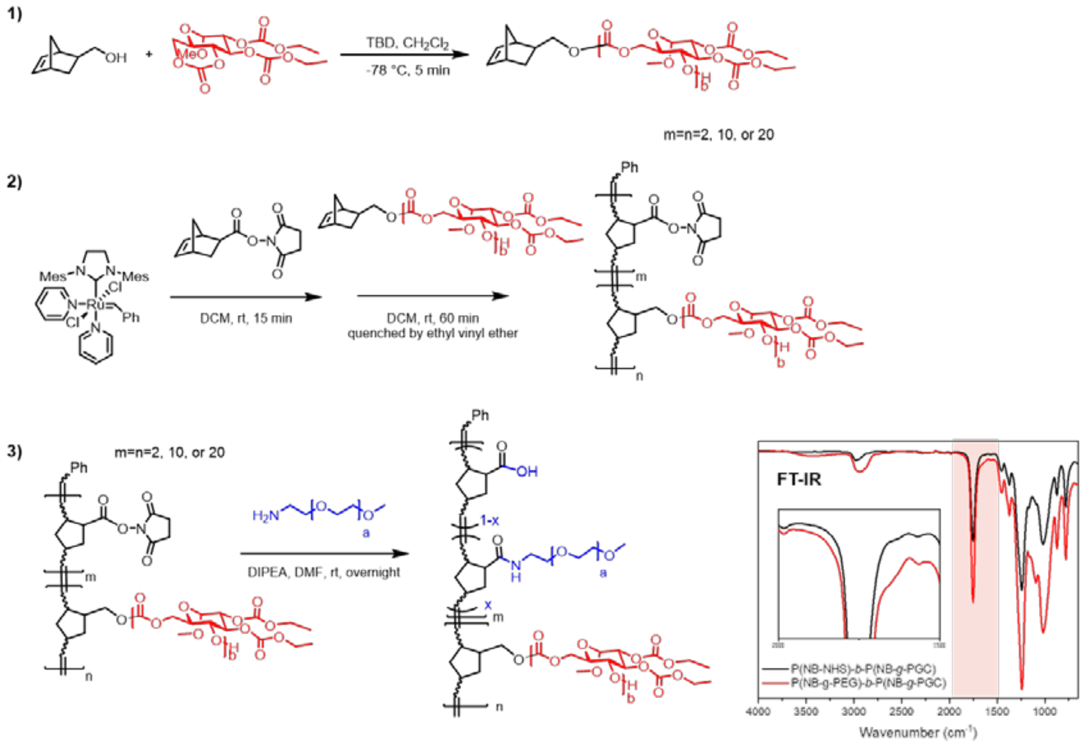

Scheme II-1 Synthesis of diblock bottlebrush copolymer $P(NB\text{-}g\text{-}PEG_a)_m\text{-}b\text{-}P(NB\text{-}g\text{-}PGC_b)_n$

In order to systematically investigate the effects of backbone length, side chain length, side chain chemistry, and architecture on morphology of nanostructures resulting from solution assembly of diblock bottlebrush copolymers, a series of bottlebrush copolymers were synthesized and assembled into nanoscopic structures. The bottlebrush copolymers contain either PGC or PDLLA as their hydrophobic segment and PEG as their hydrophilic segments. Ring-opening polymerizations (ROP) of glucose carbonate monomers or D,L-lactide monomers targeting different molar masses (*i.e.*,4 kDa and 9 kDa) were initiated by a norbornene-functionalized alcohol to a afford a series of PGC or PDLLA-based macromonomers, respectively. The following synthesis of diblock bottlebrush

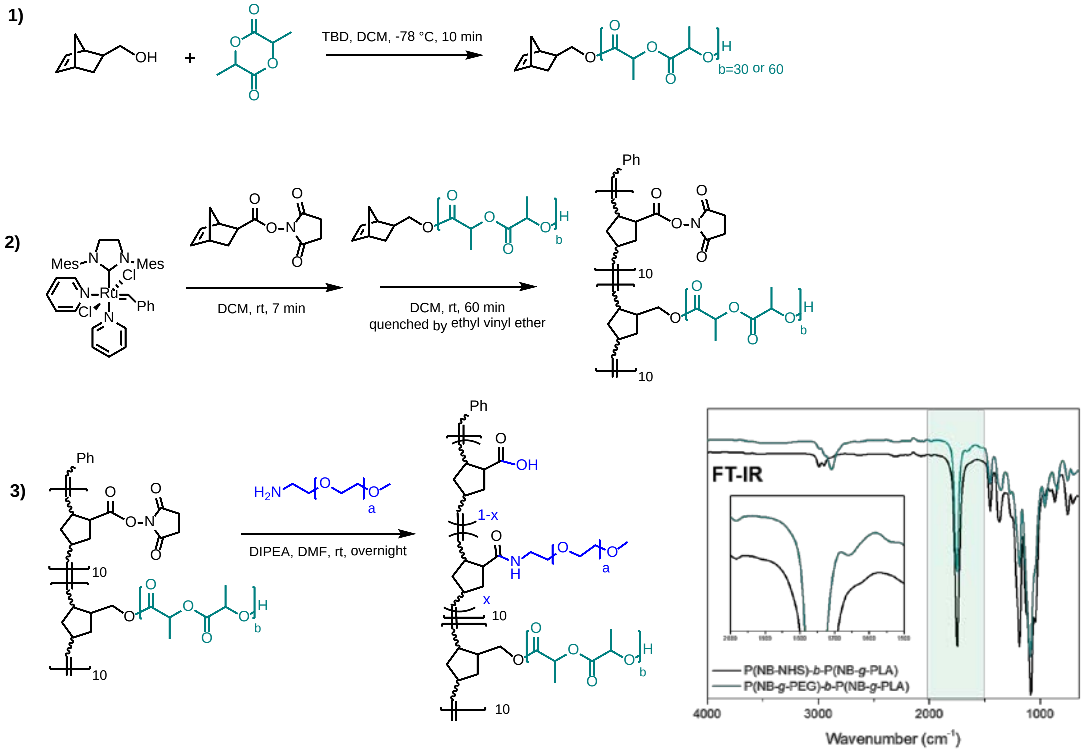

Scheme II-2 Synthesis of diblock bottlebrush copolymer *P(NB-g-PEG$_a$)$_m$-b-P(NB-g-PDLLA$_b$)$_n$*

Table II-1 Design of PGC-based diblock bottlebrush copolymers with varied PEG side chain lengths and backbone lengths

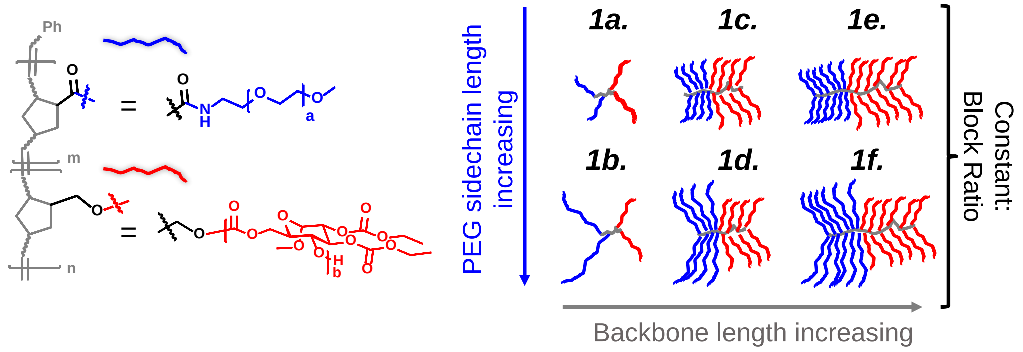

	Backbone Length (m)	(n)	DP_{PEG} (a)	DP_{PGC} (b)	PEGylation Percentage (x)	PEG Weight Percentage	PGC Weight percentage	$M_{n\ NMR}$
1a.	2	2	45	25	82%	15%	85%	21.6 kDa
1b.	2	2	113	25	94%	34%	66%	27.7 kDa
1c.	9	10	45	25	72%	12%	88%	104 kDa
1d.	9	10	113	25	90%	31%	69%	132 kDa
1e.	24	20	45	25	70%	16%	84%	217 kDa
1f.	24	20	113	25	75%	33%	67%	274 kDa

copolymers involves two steps: the first step is by "grafting-through" - a sequential ring-opening metathesis polymerization (ROMP) of a norbornenyl-functionalized *N*-hydroxysuccinimidyl (NHS) ester monomer and the norbornene-terminated PGC or PDLLA; the second step is by "grafting-to" – a post-polymerization modification by methoxy PEG amine with different molar masses (*i.e.*, 2 kDa and 5 kDa). Thus, diblock bottlebrush polymers with well-defined and comparable backbone lengths are synthesized for further self-assembly studies (**Scheme II-1** and **Scheme II-2**). It is noted that the PEGylation percentage (x) for all bottlebrush copolymers are higher than 70%, and mostly

Table II-2 Design of PGC and PDLLA-based diblock bottlebrush copolymers with varied PEG side chain lengths, hydrophobic side chain chemistry, and PDLLA side chain lengths

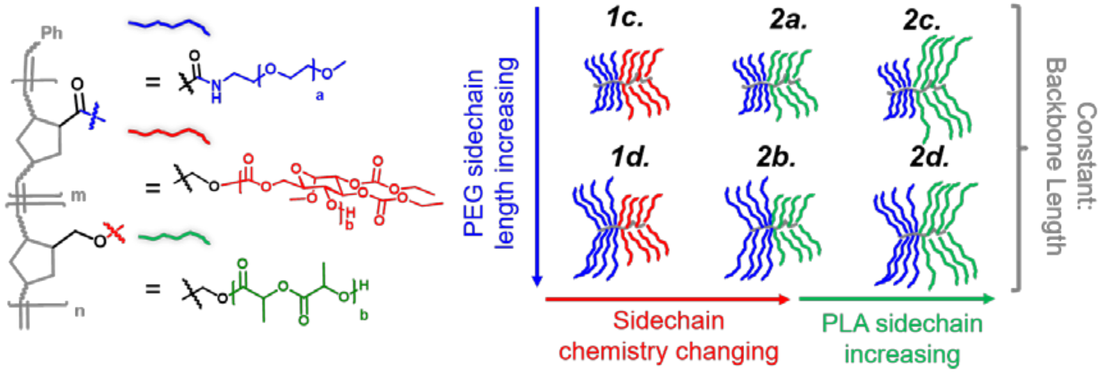

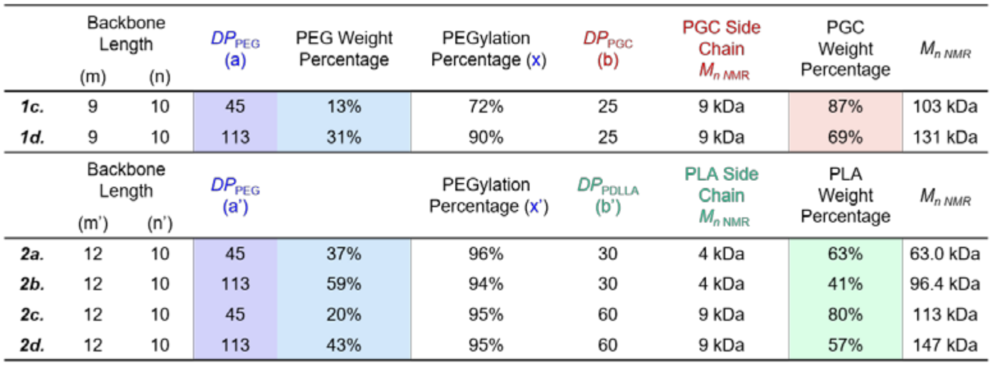

	Backbone Length (m)	(n)	DP_{PEG} (a)	PEG Weight Percentage	PEGylation Percentage (x)	DP_{PGC} (b)	PGC Side Chain $M_{n\ NMR}$	PGC Weight Percentage	$M_{n\ NMR}$
1c.	9	10	45	13%	72%	25	9 kDa	87%	103 kDa
1d.	9	10	113	31%	90%	25	9 kDa	69%	131 kDa
	Backbone Length (m')	(n')	DP_{PEG} (a')		PEGylation Percentage (x')	DP_{PDLLA} (b')	PLA Side Chain $M_{n\ NMR}$	PLA Weight Percentage	$M_{n\ NMR}$
2a.	12	10	45	37%	96%	30	4 kDa	63%	63.0 kDa
2b.	12	10	113	59%	94%	30	4 kDa	41%	96.4 kDa
2c.	12	10	45	20%	95%	60	9 kDa	80%	113 kDa
2d.	12	10	113	43%	95%	60	9 kDa	57%	147 kDa

80 - 100%, thus the non-PEGylated carboxylic acid moiety is neglected in following schematic illustrations.

In order to investigate the correlation between resulting morphologies and chemical structures of diblock bottlebrush copolymers, by varying each molecular parameter *(i.e.*, backbone length, side chain length, side chain chemistry, and architecture), two groups of bottlebrushes were designed with corresponding diblock bottlebrush structures for comparison, as shown in **Table II-1** and **Table II-2**. In **Table II-1**, bottlebrushes **1a-f** were designed with three different backbone lengths (*i.e.*, DP=2, 10, 20) with constant block ration 1:1. Besides, for each backbone length, the hydrophilic PEG side chain is tuned between 2 kDa and 5 kDa to investigate the effect of hydrophilic side chain length on assembly morphology. In **Table II-2**, bottlebrushes **1c-d** and **2a-d** are designed with constant backbone length. In addition to varying hydrophilic PEG side chain length, the chemistry and chain length of hydrophobic chain are altered as well. Therefore, bottlebrushes with varied hydrophilic side chain lengths, hydrophobic side chain lengths and hydrophobic side chain chemistry are compared.

The as-synthesized bottlebrushes **1a-f** and **2a-d** were assembled in solution followed by a dialysis-based solvent exchange process. Diblock bottlebrush copolymers were firstly dissolved in DMF to afford 1 mg/mL solutions at room temperature, then 2× volume of nanopure water was slowly added into the polymer-DMF solution by a syringe pump at the rate of 2 mL/h, stir at 200 rpm, followed by dialysis against nanopure water for three days before characterization by DLS and TEM. The morphology of the resulting nanostructures was characterized by TEM, and the size was quantitatively measured by DLS.

Effect of backbone length and relative weight percentage. In **Figure II-1** and **Figure II-2**, following the order of **1a - 1c - 1e** or **1b – 1d – 1f**, the backbone lengths increase from DP for each block = 2 to 10 to 20. It is found that for bottlebrushes with short backbone (DP for each block = 2), **1a** and **1b**, interconnected spherical micelles and short worm-like assemblies were formed with an average diameter of 15 ± 2 nm and an average width of 17 ± 6 nm, respectively. For bottlebrushes with medium backbone (DP for each block = 10), **1c** and **1d**, double-layer vesicles with a relatively large diameter (210 ± 70

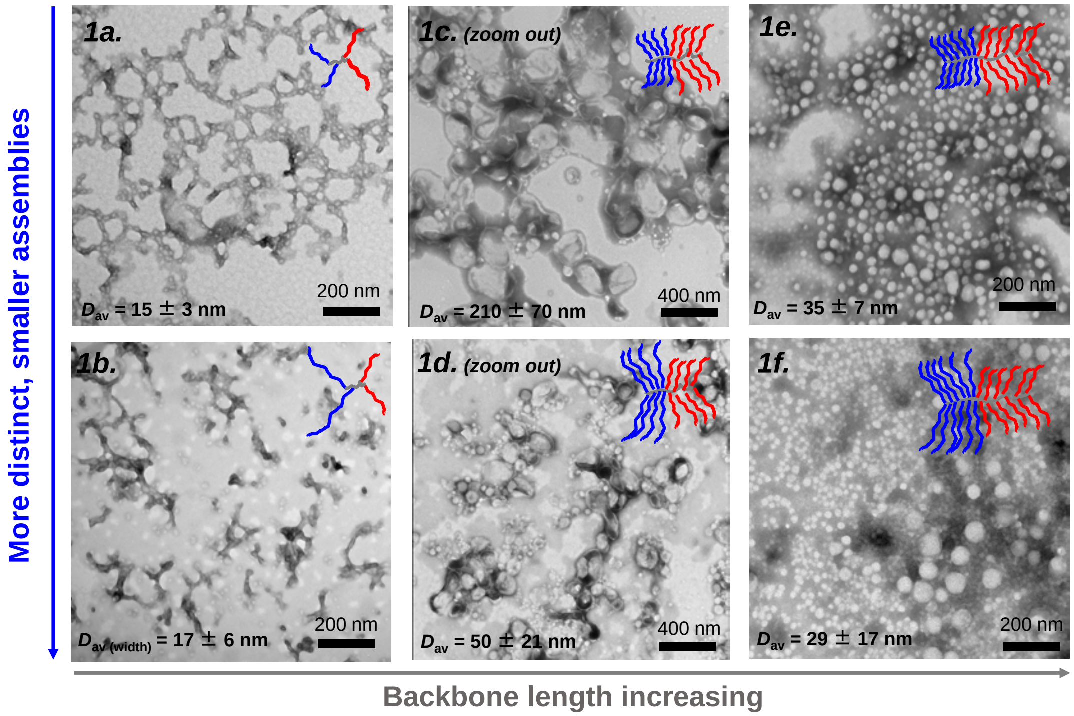

Figure II-1 TEM analysis of assemblies obtained from bottlebrush copolymers 1a - f. TEM samples were negatively stained with 1 wt% phosphotungstic acid aqueous solution (20 uL), and the diameters were measured by counting >50 nanoparticles.

nm) and a relatively small diameter (50 ± 24 nm) were observed, respectively. For bottlebrushes with long backbone (DP for each block = 20), uniform spherical micelles with an average diameter of 35 ± 7 nm were observed for bottlebrush **1e**, and a mixture of relatively small and large spherical micelles with an average diameter of 29 ± 17 nm was observed for bottlebrush **1f**. Therefore, it is found that the morphology for the bottlebrushes with same backbone length is consistent to some extent. However, the transition of morphology and size between bottlebrushes with different backbone lengths is not that clear and conclusive. Then, by revisiting the synthetic details of these bottlebrushes in **Table II-1**, it is found that although the block ratio was controlled as 1:1

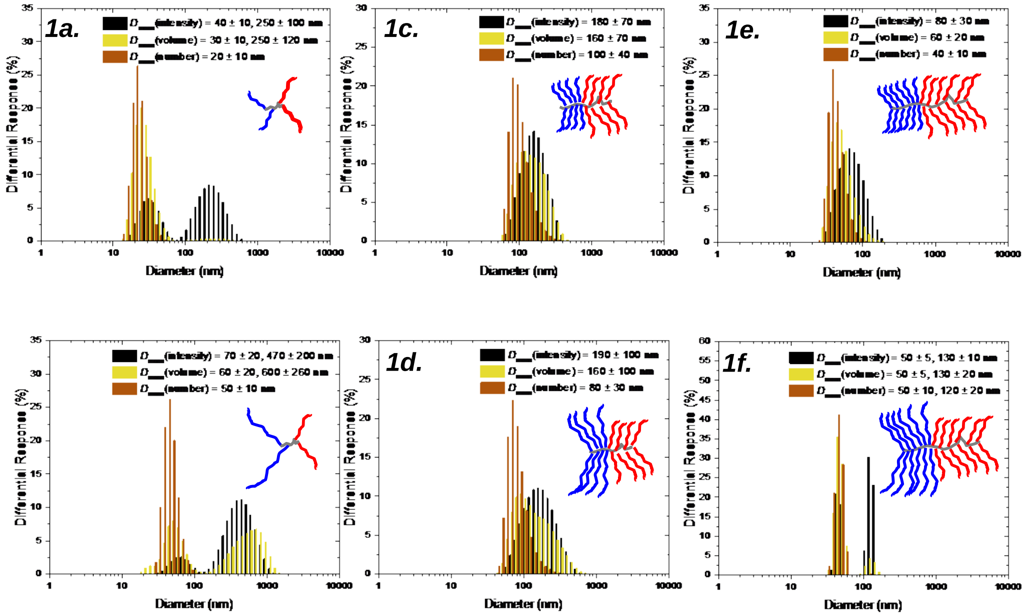

Figure II-2 DLS characterization of diblock bottlebrush copolymers **1a - f.**

with minimum deviation, the weight percentages of hydrophobic (hydrophilic) block of **1a**, **1c**, and **1e** as well as **1b**, **1d**, and **1f** still have less than 3% difference. Consequently, the slight difference in weight percentage may be the cause of the inconclusive morphology trend. For example, **1c** and **1d** have a larger volume fraction of hydrophobic PGC block compared with **1a** and **1b**, leading to a flatter interface and thereby affording double-layer vesicle morphology. Likewise, **1e** and **1f** have a larger volume fraction of hydrophilic PEG block compared with **1a** and **1b**, resulting in a smaller interface curvature and thereby affording spherical micelle morphology.

Effect of hydrophilic side chain length. As shown in **Figure II-1** and **Figure II-3**, as the hydrophilic PEG chain length increases, the morphology remains similar while more distinct and smaller size assemblies were observed. This size change can be explained by

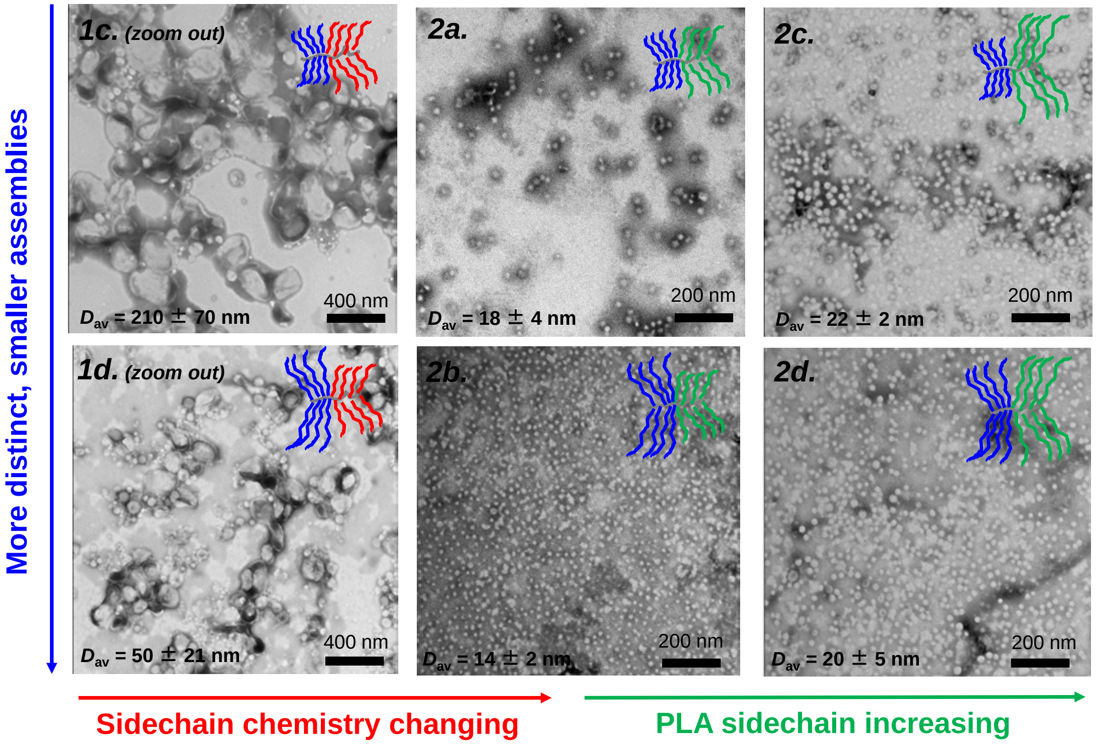

Figure II-3 TEM analysis of assemblies obtained from bottlebrush copolymers **1a – b**, **2a - d**. TEM samples were negatively stained with 1 wt% phosphotungstic acid aqueous solution (20 uL), and the diameters were measured by counting >50 nanoparticles.

the increase in hydrophilic volume fraction, which causes a more curved interface between the hydrophilic and hydrophobic interface.

Effect of hydrophobic side chain chemistry and length. In order to investigate the effect of side chain chemistry on morphology of solution assemblies, bulky PGC and linear PDLLA were synthesized as hydrophobic side chains of diblock bottlebrushes, of which degree of polymerization and molar mass are set as constant and variable alternatively, as shown in **Figure II-3.** It is found that either with same hydrophobic and hydrophilic side chain length (degree of polymerization) or malar mass, the diblock

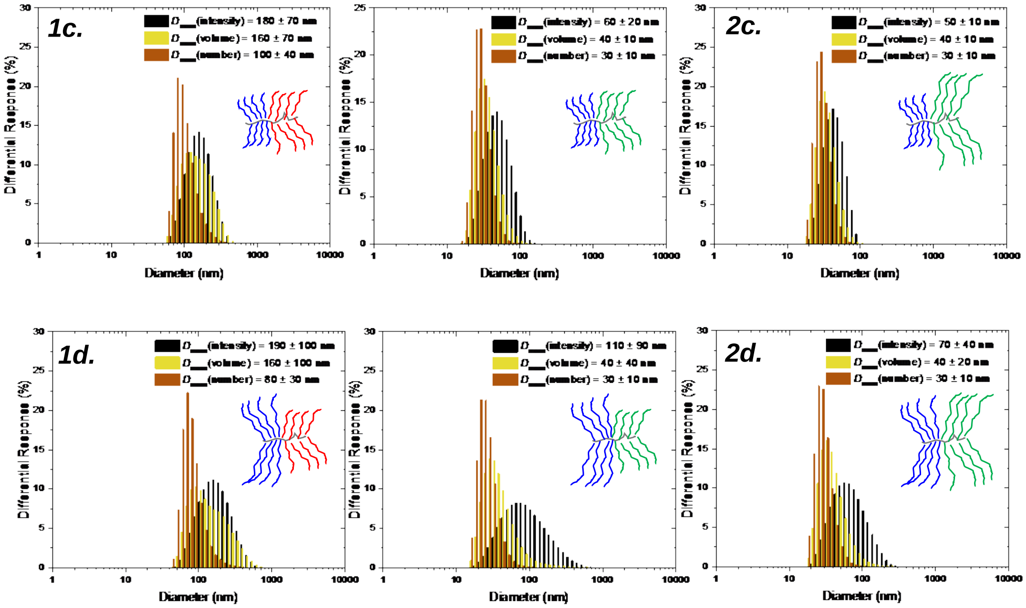

Figure II-4 DLS characterization of diblock bottlebrush copolymers **1a - f**.

bottlebrushes with PDLLA side chains are likely to form spherical micelles, which is speculated to result from the lower volume fraction of PDLLA compared with PGC. Therefore, the molecular structure of side chain building blocks also plays an important role in solution assembly of diblock bottlebrushes. Moreover, according to the diameter measurements by TEM in **Figure II-3** and DLS in **Figure II-4**, the assemblies obtained from bottlebrushes with longer hydrophobic side chains (**2c -d**) have larger sizes than the ones with shorter hydrophobic side chains (**2a – b**), which is attributed to corresponding hydrophobic volume fractions, following the same rule as hydrophilic side chains.

Effect of architecture and relative weight percentage. In addition to bottlebrushes, a series of diblock copolymers with linear, star-shaped, and short brush architectures were synthesized with similar block ratio (*ca.* 1:1) and molar masses (**Scheme II-3**). Thus, the

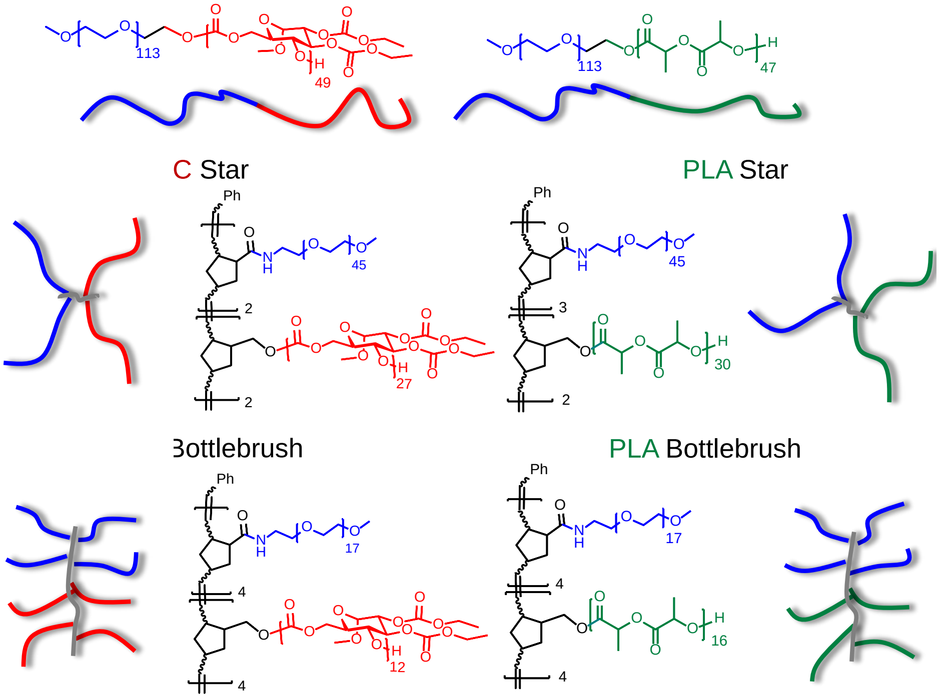

Scheme II-3 Chemical structures and schematic illustrations of diblock linear, star-shaped, and short brush copolymers.

effect of architectures on assembly morphology can be designed and studied. The synthesis of star-shaped and short brush copolymers followed the same strategy as mentioned above, while the linear diblock copolymers were synthesized *via* ROP initiated by methoxy PEG alcohol as a macroinitiator, as shown in **Scheme II-4**. The synthetic details are listed in **Table II-3**, indicating for each group of diblock copolymers based on same chemistry, their molar masses remain in a narrow range of 21 – 23 kDa (PGC) and 12 – 15 kDa (PDLLA). Also, diblock copolymers based on PGC generally have higher molar masses compared with corresponding copolymers based on PDLLA. The resulting

Table II-3 Synthetic details and SEC traces of diblock linear, star-shaped, and short brush copolymers based on PGC and PDLLA.

	$\frac{49}{113}$	$\frac{49\times364}{113\times44}$
	$\frac{27\times2}{45\times2}$	$\frac{27\times2\times364}{45\times2\times44}$
	$\frac{12\times4}{17\times4}$	$\frac{12\times4\times364}{17\times4\times44}$

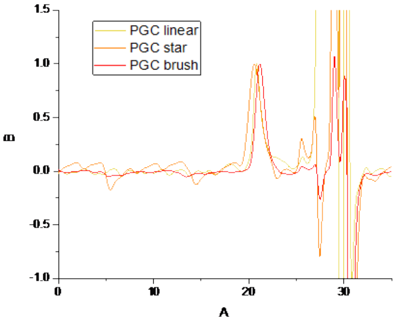

	$\frac{47}{113}$	$\frac{47\times144}{113\times44}$
	$\frac{30\times2}{45\times3}$	$\frac{30\times2\times144}{45\times3\times44}$
	$\frac{16\times4}{17\times4}$	$\frac{16\times4\times144}{17\times4\times44}$

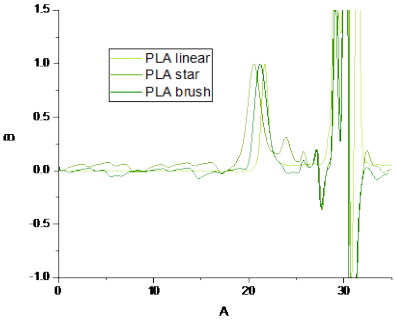

assemblies of these diblock copolymers shown in **Figure II-5** and **Figure II-6** reveal that for same architecture, the diblock copolymers are likely to adopt similar nanoscopic morphologies. For example, the linear copolymers formed distinct assemblies, and the

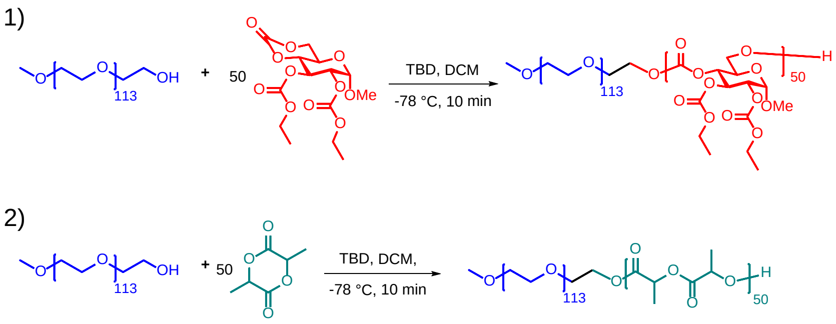

Scheme II-4 Synthetic routes of diblock linear copolymers PEG$_{113}$-*b*-PGC$_{50}$ and PEG$_{113}$-*b*-PDLLA$_{50}$.

star-shaped copolymers afforded an interconnected network, or pearl necklace-like structure. The short PGC brushes and PDLLA brushes yielded different assemblies: the PGC brushes tend to yield worm-like structures while PDLLA-based brushes tend to aggregate together to form a closely packed cluster. However, the reason behind the morphology preference of those diblock copolymers is still under investigation. There is one factor that is supposed to affect the morphological transition – hydrophilic and hydrophobic relative weight percentage. Like the study of backbone length effect, although the block ratio between hydrophilic and hydrophobic segments has been

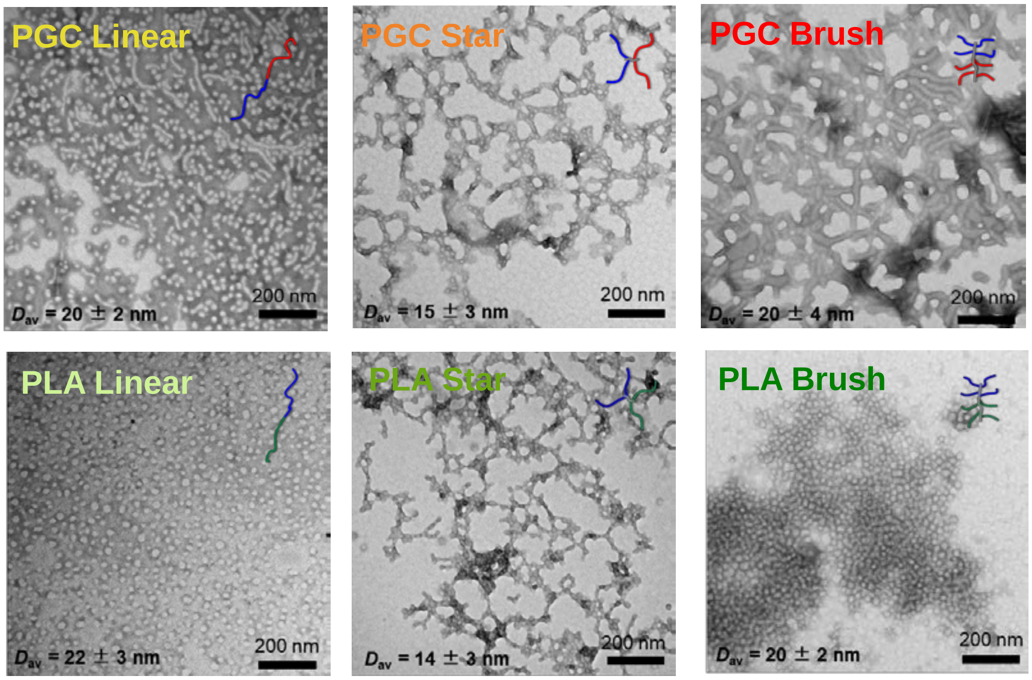

Figure II-5 TEM analyis of nanoscopic assemblies obtained from diblock linear, star-shaped, and short brush copolymers based on PGC and PDLLA.

controlled as close to 1:1 as possible, the relative weight percentages among three architectures are not exactly same, which may impact their morphological transition.

Conclusions

In this work, a series of comparison between diblock copolymer with varied backbone length, hydrophilic and hydrophobic side chain length, hydrophobic side chain chemistry as well as polymer architectures have been designed and investigated. It is found that the relative weight percentages of hydrophilic and hydrophobic blocks of the diblock bottlebrushes greatly affect the volume fractions of resulting assemblies. Therefore, a precise control over relative weight percentage is highly required for investigation of assembly morphology. In general, the assemblies obtained from diblock bottlebrushes with larger hydrophilic (PEG) volume fraction are likely to adopt more distinct shapes

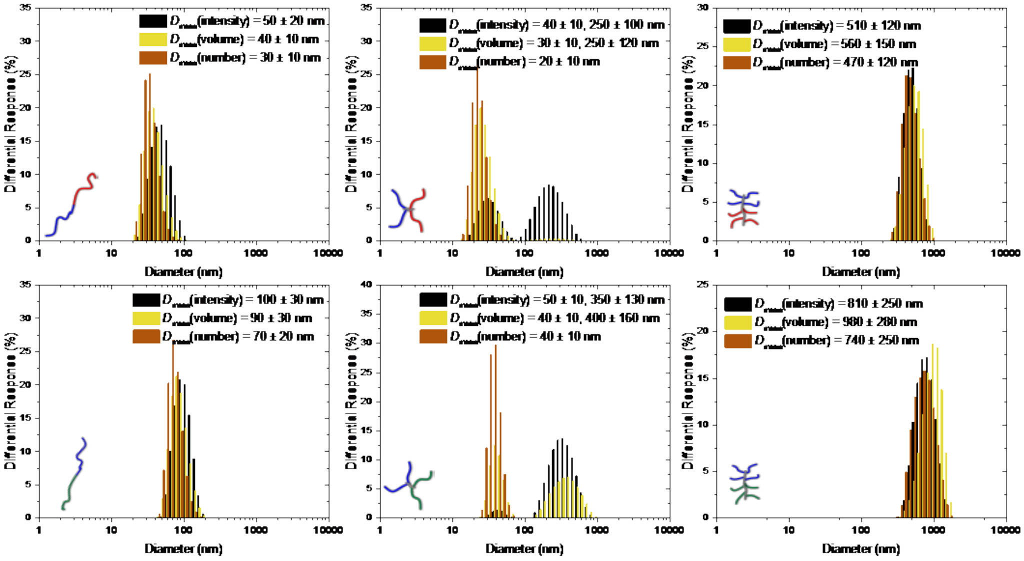

Figure II-6 DLS analysis of nanoscopic assemblies obtained from diblock linear, star-shaped, and short brush copolymers based on PGC and PDLLA.

with smaller size, such as spherical micelles; while the assemblies obtained from diblock bottlebrushes with larger hydrophobic (PGC or PDLLA) volume fraction are likely to adopt more complex (*e.g.*, double layer, clustered) shapes with larger size. In addition, the molecular structure of building blocks also affects the side chain conformation, which further leads to variation in overall assembly structures. In a word, the highly tunable structure of bottlebrush copolymers allows the fundamental study of the structure-property relationship stemming from each component in various dimensions, therefore expanding their potential applications and advancing their underlying functionality as a promising degradable and functional material in biomedical, environmental field, *etc.*

CHAPTER III

COMPLEX SUGAR-BASED COIL-BRUSH BLOCK POLYMER NANOASSEMBLIES IN AQUEOUS SOLUTION[*]

Introduction

Self-assembly of degradable synthetic polymers, especially those with increasing topological complexity, has been studied for several decades as a powerful way to create nanostructures and the vast amount of experimental work is now experiencing iterative interplay with guidance by theoretical and computational advances. Obtaining more complex nanostructures has long fascinated researchers at the interface of biology, chemistry, materials science, and medicine,[77-80] and motivated the design of amphiphilic macromolecules with degradability, *e.g.* polyesters, polypeptides, and polycarbonates,[75, 81-88] as well as sophisticated architectures, *e.g.* cyclic, bottlebrush, and branched structures.[89-91] Precisely-constructed brush polymers are of increasing interest, especially multifunctional bottlebrushes that are capable of supramolecular assembly into biologically-active nanomaterials, due to their physicochemical properties, such as their extended backbone conformation, hindered entanglement, and feasibility as nanoscopic molecular building blocks with tunable relative concentric and lengthwise dimensions.[34, 92-94] Coil-brush block polymers, also known as linear-*block*-brush polymers, contain both

---

[*] Reprinted (adapted) with permission from “Experiments and Simulations of Complex Sugar-Based Coil-Brush Block Polymer Nanoassemblies in Aqueous Solution” by Dong, M.; Wessels, M. G.; Lee, J. Y.; Su, L.; Wang, H.; Letteri, R. A.; Song, Y.; Chen, Y.; Li, R.; Lin, Y.; Pochan, D. J.; Jayaraman, A.; Wooley, K. L., *ACS Nano* **2019**, *13*, 5147-5162. https://pubs.acs.org/doi/abs/10.1021/acsnano.8b08811. Copyright 2019 American Chemical Society.

a flexible linear structure as well as a bulky bottlebrush structure, resulting in a wide range of compositional variables over both blocks, individually, as well as their combined two-dimensional architectures. The assembly behavior of coil-brush polymers is expected to be fundamentally different from either linear or brush block polymers; the molecular parameters within their unconventional asymmetric architecture are associated with an interesting set of tradeoffs between various polymer-polymer/surface/solvent interactions in the system, caused by their intrinsic imbalances. Owing to their molecular geometry, they exhibit distinct microphase separation patterns in the bulk and at interfaces, and assemble into defined aggregates in solution.[95-106] Among all the characteristics, the ability of amphiphilic coil-brush polymers to self-assemble into numerous nanoscopic objects, including spherical,[96, 103, 107-109] hexagonal,[110] cylindrical,[111-112] vesicle,[113] lamellar morphologies,[110] *etc.* offers significant diversity in the construction of well-defined nanoscopic materials. Schmidt and coworkers have reported the synthesis and self-assembly of poly(styrene-*block*-((2-isobutyryloxy) ethyl methacrylate)-*graft*-(acrylic acid)) (PS-*b*-(P^{i}BEMA-*g*-PAA)) coil-brush block polymers that were observed to form star-like micelles in aqueous solution by scanning force microscopy.[114] Hadjichristidis and coworkers have studied the micellization behavior of complex comb-like block polymers containing polystyrene, polyisoprene, or polybutadiene components with various architectures.[115] Xi, Chen, and coworkers synthesized amphiphilic comb-dendronized diblock polymers composed of a hydrophobic Percec-type dendronized polystyrene block and a hydrophilic comb-like poly(ethylene oxide) grafted polymethacrylate block, and obtained diverse morphologies, such as twisted string, vesicle, and large compound micelles in a mixture of methanol and tetrahydrofuran.[116] Lin and coworkers reported the synthesis and self-assembly behavior of an amphiphilic coil-brush block polymer bearing hydrophilic poly(ethylene glycol) and hydrophobic polypeptide brush segments in aqueous solution, and investigated the morphology as a function of brush length.[117]

The breadth of the types of polymers that can be designed, synthesized and assembled experimentally has been growing, inspiring the use of theoretical and computational tools to investigate increasingly complex polymers and predict molecular features of the polymers needed to achieve nanostructures that meet the design criteria for specific applications. Theory and molecular simulations allow for systematic variation of parameters in polymer design and explanation of the molecular packing within the assembled states as a function of the polymer design; this motivates the synergistic use of theory and simulations with experiments.[118-130] Simulation and theory have been used to study coil-branched architectures such as coil-dendrimer, coil-star, and coil-brush block polymer assembly in melt-like conditions[131-138] and in solution.[139-142] Solution assembly of linear-branched architectures, namely single examples of each of the following architectures: linear-linear, linear-comb, linear-star, and linear-dendritic copolymers, have been studied by Cheng and coworkers, who used Brownian dynamics simulations to find that the critical micelle concentration increases with increased branching, while the micelle size and aggregation number decrease with increased branching.[140] Self-consistent field theory (SCFT) calculations have been used to investigate coil-brush block polymer micelles with a solvophobic backbone and solvophilic side chains, showing a bimodal distribution of micelles where the backbone section with grafted side chains either separates to the core-corona interface or forms part of the corona.[139] These studies indicate the ability of computational tools to systematically vary the coil-brush design parameters and study their effect on the resulting molecular packing and micellization behavior.

Herein, we report the synthesis, molecular modeling, and assembly of a series of asymmetric coil-brush block polymers containing a flexible, hydrophilic carboxylic acid coil block and a rigid, hydrophobic bottlebrush block comprised of hydrolytically-degradable glucose carbonate-based oligo/polymeric side chain grafts. We developed an intermediate resolution coarse-grained model to mimic the synthesized coil-brush block polymers in molecular dynamics (MD) simulations. The design of the coil-brush block polymers was followed by their assembly through a dialysis-based solvent exchange process in experiments and by directly changing the solvent quality to mimic dialysis in simulations. As a result, phase diagrams using both experiment and simulation were constructed, showing that the morphology depends on both the length of hydrophobic side chains and the overall hydrophilic/hydrophobic ratio, described in terms of the molar ratio of carboxylic acid units to glucose carbonate units (A/G).[143-144] The morphologies of the assembled structures as a function of coil-brush design parameters matched well between the experiments and MD simulations. We also quantified the chain packing parameters[145] within the assembled structures in the simulations and found how the packing parameter changes with the coil-brush polymer design. This experiment-simulation work validates the coarse-grained model and provides a platform for further investigation using both simulation and experiment to explore wider design parameter space and establish design rules for assembly towards desired nanostructures.[88, 146-147]

Materials and Methods

Materials

The bicyclic glucose-based carbonate monomer, methyl-2,3-*O*-ethyloxycarbonyl-4,6-*O*-carbonyl-α-d-glucopyranoside (GC)[75] and the Grubbs' G3 catalyst[76], were synthesized according to previously-published procedures. 3-(3-Dimethylaminopropyl)-1-ethyl-carbodiimide hydrochloride (EDC hydrochloride) was purchased from Chem-Impex International, Inc. 1,5,7-Triazabicyclo[4.4.0]dec-5-ene (TBD) was received from TCI America (Portland, OR), degassed, and stored in a glovebox under Ar atmosphere. Other chemicals and reagents were purchased from Sigma-Aldrich, Co. (St. Louis, MO) and were used as received, unless otherwise noted. Dichloromethane (DCM) and *N*,*N*-dimethyl formamide (DMF) were dried using a solvent purification system (J. C. Meyer Solvent Systems, Inc., Laguna Beach, CA). Nanopure water (18 MΩ·cm) was obtained from a Milli-Q water filtration system (Millipore Corp, USA). Dialysis membrane tubing with a molar mass cut off (MWCO) of 6-8 kDa was purchased from Spectrum Laboratories, Inc. (Rancho Dominguez, CA) and soaked for 5 min in nanopure water at room temperature (rt) before use. Column chromatography was performed on a CombiFlash Rf4x (Teledyne ISCO) with RediSep Rf columns (Teledyne ISCO).

Instrumentation

^{1}H NMR and ^{13}C NMR spectra were recorded on Varian Inova 500 spectrometer (Varian, Inc., Palo Alto, CA) interfaced to a UNIX computer using the VnmrJ software. Chemical shifts for ^{1}H NMR and ^{13}C NMR signals were referenced to the solvent resonance frequencies. Fourier transform infrared (FT-IR) spectra were recorded on an IR Prestige 21 system, equipped with a diamond attenuated total reflection (ATR) lens (Shimadzu Corp., Japan), and analyzed using IRsolution v. 1.40 software.

Size exclusion chromatography (SEC) was used to determine polymer molar mass and molar mass distribution (or dispersity, *Đ*). Polymer solutions were prepared at a known concentration (3-5 mg/mL) and 200 µL of an injection volume was used. After filtration through a 0.45 µm PTFE filter, the polymer samples were passed through the SEC system equilibrated at 40°C in tetrahydrofuran (THF) as the mobile phase with the flow rate of 1 mL/min. SEC was conducted on a Waters 1515HPLC (Waters Chromatography, Inc.) equipped with a differential refractive index (RI) detector (Wyatt Technology, Optilab T-rEX), a multi-angle laser light scattering (MALLS) detector (Wyatt Technology, DAWN HELEOS II, 658 nm) using ASTRA software (Wyatt Technology; the dn/dc values of the analyzed polymers were determined from the differential refractometer response based on sample concentration, assuming 100% mass recovery), and three-column series (Phenogel 5 µm; 100 Angstroms (Å), 104 Å, and Linear (2); 300×4.6 millimeters (mm) columns; Phenomenex, Inc.).

Glass transition temperatures (T_g) were measured by differential scanning calorimetry (DSC) on a Mettler-Toledo DSC3/700/1190 (Mettler-Toledo, Inc., Columbus, OH) under a nitrogen gas atmosphere. Measurements were performed with a heating and cooling rate of 10 °C/min, and three heating and cooling cycles were conducted. Measurements were analyzed using Mettler-Toledo STAR^e v. 15.00a software. The T_g was taken as the midpoint of the inflection tangent of the third heating scan.

Thermogravimetric analysis (TGA) was performed under Ar atmosphere using a Mettler-Toledo TGA2/1100/464, with a heating rate of 10 °C/min. Data were analyzed using Mettler-Toledo STAR^e v. 15.00a software.

Electrospray ionization mass spectrometry (ESI-MS) was performed using an Applied Biosystems PE SCIEX QSTAR instrument. Matrix-assisted laser desorption ionization-time of flight mass spectrometry (MALDI-Tof MS) was performed on a microflex™ LRF mass spectrometer (Bruker Corporation, Billerica, MA) in positive linear mode. Ions were generated by a pulsed nitrogen laser (337 nm, 25 kV), and 100 laser pulses were used per spectrum. Trans-2-[3-(4-*tert*-butylphenyl)-2-methyl-2-propylidene]malonitrile (DCTB) and potassium trifluoroacetate (KTFA) were used as a matrix and cationization reagent, respectively. The sample and matrix were prepared at 1 and 26 mg/mL, respectively, in chloroform, and KTFA was prepared at 1 mg/mL in acetone. The sample solution was mixed with the matrix and KTFA at a volumetric ratio of 2:5:1, and 1 μL of the mixture was deposited onto a stainless-steel sample holder and dried in air prior to the measurement.

Transmission electron microscopy (TEM) images were collected on a JEOL 1200EX operated at 100 kV, and micrographs were recorded using an SIA-15C CCD camera. Samples for TEM were prepared as follows: 20 μL of polymer solution in nanopure water (1 mg/mL) was deposited onto a carbon-coated copper grid, and after 1 min, excess solution was quickly wicked away by a piece of filter paper. The samples were then negatively stained with a 1 wt% phosphotungstic acid (PTA) aqueous solution (20 µL). After 30 s, excess staining solution was quickly wicked away by a piece of filter paper and the samples were left to dry under ambient conditions prior to imaging.

Atomic force microscopy (AFM) was performed using a Multimode 8 system (Bruker) using a ScanAsyst-Air Silicon Nitride probe (k = 0.4 N/m, f_0 = 70 kHz, Bruker). AFM images were assessed with Nanoscope Analysis (Bruker). For AFM sample preparation, the solution of nanoparticles in nanopure water (20 µL) at 0.3 mg/mL was deposited on the mica surface, followed by spin coating. The mica surface was allowed to dry *in vacuo*.

Cryogenic-TEM (CryoTEM) images were performed on FEI Talos operated at an accelerating voltage of 200 keV. For vitrified grid preparation, the FEI Vitrobot system, an automated plunge freezing device was used. First, a droplet (3 µL) of polymer solution was deposited onto a plasma-treated lacey carbon grid, and then blotted 2-3 times with each blot lasting around 1 s. After blotting, the sample was allowed to relax for 2 s to achieve uniform liquid thickness and then quickly plunged into a liquid ethane reservoir. The grids were then transferred to liquid nitrogen until further imaging. The temperature during imaging was maintained at -178 °C to avoid any liquid crystallization. All images were taken with FEI Falcon II camera with 1 s exposure time.

Dynamic light scattering (DLS) measurements were conducted using a Zetasizer Nano ZS instrument (Malvern Panalytical Ltd., Malvern, United Kingdom) equipped with a laser diode operating at 633 nm. Scattered light was detected at 175° and analyzed using a log correlator for a 0.5 mL of sample in a disposable cell (capacity = 0.9 mL). The photomultiplier aperture and attenuator were adjusted automatically. The particle size distribution and distribution averages were calculated using particle size distribution analysis routines in Zetasizer 7.13 software. Number of accumulations and measurement duration were adjusted automatically. All measurements were repeated 3 times. The average diameter of the particles is reported as the intensity-, volume- and number-average particle diameter from three measurements.

Experimental Procedures

Synthesis of the Hydrophilic Precursor Monomer, Bicyclo[2.2.1]hept-5-ene-exo-2-carboxylic acid N-hydroxysuccinimide Ester (NB-NHS Ester). In a 25 mL Schlenk flask charged with a stir bar, the *exo*-5-norbornenecarboxylic acid (283 mg, 2.05 mmol, 1.0 eq.), *N*-hydroxysuccinimide (320 mg, 2.78 mmol, 1.4 eq.), and *N*-(3-dimethylaminopropyl)-*N*'-ethylcarbodiimide hydrochloride (EDCI·HCl) (470 mg, 3.03 mmol, 1.5 eq.) were allowed to stir in 10 mL anhydrous DCM for 20 h under nitrogen flow at room temperature. The reaction mixture was concentrated under reduced pressure, and *N*-hydroxysuccinimidyl (NHS) ester was purified by flash chromatography (100% DCM as eluent) to afford **1** as a white powder (482 mg, 1.70 mmol, 83% yield). ^{1}H NMR (500 MHz, $CDCl_3$) δ ppm 6.19 (dd, *J* = 6, 3 Hz, 1H), 6.13 (dd, *J* = 6, 3 Hz, 1H), 3.25 (s, 1H), 2.99 (s, 1H), 2.81 (d, *J* = 4 Hz, 5H), 2.49 (dd, *J* = 9, 4 Hz, 1H), 2.03 (dt, *J* = 12, 4 Hz, 1H), 1.59 – 1.47 (m, 2H), 1.43 (d, *J* = 9 Hz, 1H). ^{13}C NMR (126 MHz, $CDCl_3$) δ ppm 171.63, 169.37, 138.62, 138.53, 135.26, 47.10, 46.39, 41.76, 40.29, 30.95, 25.61. FT-IR (ATR, cm^{-1}) 3071-2876, 1806, 1779, 1736, 1331, 1200, 1060, 947, 841, 710, 644. HRMS: calculated $[M+H]^+$ for $C_{12}H_{13}NO_4H^+$: 236.0923, found: 236.0896.

General Procedure for Synthesis of Hydrophobic Macromonomers, exo-Norbornene-terminated Poly(glucose carbonate)s (NB-PGCs). To a solution of the monomer GC (100 mg, 0.275 mmol) in anhydrous DCM (500 µL) was added *exo*-5-norbornene-2-methanol (1.11 µL, 0.00960 mmol). The catalyst 1,3,5-triazabicyclo[4.4.0]dec-5-ene (TBD) (2 mol% with respect to monomer, 0.766 mg, 0.00550 mmol) was added with stirring at -78 °C for 5 min. The reaction was removed from the acetone-dry ice bath, quenched with excess addition of acetic acid, and evaporated for analysis by GPC-MALLS without purification. The polymers were precipitated three times into ice-cold methanol and dried under vacuum.

NB-PGC$_8$: ^{1}H NMR (500 MHz, CDCl$_3$) δ ppm 6.09 (t, J = 5 Hz), 5.41 – 5.25 (m), 5.06 – 4.97 (m), 4.95 – 4.87 (m), 4.84 (dd, J = 11, 9 Hz), 4.79 – 4.70 (m), 4.38 – 4.21 (m), 3.39 (s), 1.40 – 1.24 (m), 1.21 – 1.13 (m). ^{13}C NMR (126 MHz, CDCl$_3$) δ ppm 206.92, 154.20, 154.07, 153.76, 96.33, 77.27, 73.69, 73.45, 72.75, 66.71, 66.01, 64.70, 64.66, 64.54, 55.62, 55.43, 30.91, 14.09. FT-IR (ATR, cm^{-1}) 3080 – 2793, 1750, 1458, 1371, 1234, 1011, 872, 779. 90% yield. DSC: T_g = 62 °C. TGA in Ar: 272 - 384 °C, 89% mass loss.

NB-PGC$_{17}$: ^{1}H NMR (500 MHz, CDCl$_3$) δ ppm 6.09 (t, J = 4 Hz), 5.42 – 5.24 (m), 5.07 – 4.95 (m), 4.94 – 4.86 (m), 4.85 – 4.78 (m), 4.71 (dt, J = 11, 3 Hz), 4.36 – 4.26 (m), 4.26 – 4.12 (m), 4.04 (qd, J = 9, 7, 4 Hz), 3.41 (s, J = 1 Hz), 1.34 – 1.23 (m). ^{13}C NMR (126 MHz, CDCl$_3$) δ ppm 206.90, 154.10, 154.06, 153.75, 96.33, 73.70, 73.43, 72.75, 66.01, 64.69, 64.66, 64.54, 55.62, 14.10. FT-IR (ATR, cm^{-1}) 3078 – 2785, 1751, 1458, 1373, 1234, 1011, 872, 779. 93% yield. DSC: T_g = 85 °C. TGA in Ar: 245 - 401 °C, 93% mass loss.

NB-PGC$_{18}$: ^{1}H NMR (500 MHz, CDCl$_3$) δ ppm 6.09 (t, J = 4 Hz), 5.39 – 5.25 (m), 5.08 – 4.95 (m), 4.95 – 4.85 (m), 4.83 (dd, J = 11, 9 Hz, 7H), 4.38 – 3.96 (m), 3.41 (s), 1.38 – 1.18 (m). ^{13}C NMR (126 MHz, CDCl$_3$) δ ppm 154.10, 154.07, 153.75, 96.33, 73.69, 73.43, 72.75, 66.71, 66.01, 64.69, 64.66, 64.58, 55.62, 14.09. FT-IR (ATR, cm^{-1}) 3078 – 2800, 1751, 1458, 1371, 1234, 1011, 872, 779. 95% yield. DSC: T_g = 89 °C. TGA in Ar: 240 - 387 °C, 88% mass loss.

NB-PGC$_{20}$: ^{1}H NMR (500 MHz, CDCl$_3$) δ ppm 6.09 (m), 5.40 – 5.30 (m), 4.88 – 4.79 (m), 4.79 – 4.69 (m), 4.37 – 3.68 (m), 3.45 – 3.39 (m), 1.92 – 1.29 (m). ^{13}C NMR (126 MHz, CDCl$_3$) δ ppm 206.92, 154.10, 154.07, 153.75, 153.76, 96.32, 73.68, 73.42, 72.74, 72.41, 66.71, 66.01, 64.70, 64.67, 64.58, 64.54, 55.62, 14.10. FT-IR (ATR, cm^{-1}) 3078 – 2800, 1751, 1458, 1371, 1234, 1011, 872, 779. 95% yield. DSC: T_g = 93 °C. TGA in Ar: 264 - 393 °C, 93% mass loss.

NB-PGC$_{25}$: ^{1}H NMR (500 MHz, CDCl$_3$) δ ppm 6.11 (t, J = 4 Hz), 5.40 – 5.30 (m), 5.03 (t, J = 4 Hz), 4.84 (t, J = 10 Hz), 4.75 (ddt, J = 14, 10, 4 Hz), 4.34 (d, J = 13 Hz), 4.25 (s), 4.29 – 4.13 (m), 4.10 – 4.02 (m), 3.49 – 3.37 (m), 3.43 (s), 1.39 – 1.25 (m). ^{13}C NMR (126 MHz, CDCl$_3$) δ ppm 206.92, 154.24, 154.10, 154.07, 153.80, 153.76, 96.32, 77.27, 77.01, 76.76, 73.68, 73.42, 72.74, 72.41, 66.71, 66.00, 64.70, 64.67, 64.58, 64.54, 55.60, 55.43, 30.91, 14.10. FT-IR (ATR, cm^{-1}) 3063 – 2801, 1751, 1458, 1373, 1234, 1018, 872, 779. 90% yield. DSC: T_g = 106 °C. TGA in Ar: 195 - 390 °C, 91% mass loss.

NB-PGC$_{33}$: ^{1}H NMR (500 MHz, CDCl$_3$) δ ppm 6.09 (m), 5.34 (dq, *J* = 11, 7, 6 Hz), 5.01 (dt, *J* = 8, 4 Hz), 4.83 (td, *J* = 10, 5 Hz), 4.75 – 4.65 (m), 4.32 (d, *J* = 13 Hz), 4.27 – 4.12 (m), 4.07 – 4.02 (m), 3.42 (d, *J* = 6 Hz), 1.29 (m). ^{13}C NMR (126 MHz, CDCl$_3$) δ ppm 206.90, 154.20, 154.07, 153.76, 96.33, 73.69, 73.43, 72.74, 66.01, 64.70, 64.66, 64.58, 55.62, 14.09. FT-IR (ATR, cm^{-1}) 3071 – 2762, 1751, 1458, 1373, 1234, 1173, 1018, 872, 779. 90% yield. DSC: T_g = 110 °C. TGA in Ar: 261 - 380 °C, 81% mass loss.

General Procedure for Sequential ROMP of NB-NHS Ester and NB-PGC. In a glove box, 250 μL of anhydrous DCM was added into vials containing NB-NHS monomer (5.0 mg, 21 μmol) to form a solution with a monomer concentration of 0.02 g/mL. To a solution of Grubbs' G3 catalyst in DCM (3.14 mg/mL, 100 μL) under argon in a glass vial capped with a septum was added the solution of NB-NHS monomer. The reaction was allowed to stir at rt for 15 min, and an aliquot of the reaction mixture (100 μL) was withdrawn for the analysis of the first block. The solution of NB-PGC macromonomer (50.0 mg/mL) in 300 μL anhydrous DCM was then quickly added to the polymerization mixture and stirred for 30 min before by addition of an excess amount of ethyl vinyl ether. The final coil-brush block polymers were obtained after precipitating the reaction mixture in diethyl ether twice and dried under vacuum overnight to yield white powders.

P(NB-NHS)$_{54}$-*b*-P(NB-*g*-PGC$_{33}$)$_{5}$: ^{1}H NMR (500 MHz, CDCl$_3$) δ ppm 5.34 (t, *J* = 9 Hz, C*H*=C*H*s from brush backbone), 5.01 (d, *J* = 4 Hz, C*H*OCH$_3$ in NB-PGC units), 4.84 (t, *J* = 9 Hz, C*H*OCO in NB-PGC units), 4.72 (m, OC*H*$_2$CH$_3$ in NB-PGC units), 4.19 (m, OC*H*$_2$CH$_3$ in NB-PGC units), 3.42 (s, OC*H*$_3$ in NB-PGC units), 2.83 (m, C*H*$_2$C*H*$_2$ from

NHS units), 2.19 (d, *J* = 1.0 Hz, C*H*$_2$s from PNB backbone), 1.29 (m, CH$_2$C*H*$_3$ in NB-PGC units). ^{13}C NMR (126 MHz, CDCl$_3$) δ ppm 154.11, 153.76, 96.36, 77.26, 77.03, 76.72, 73.70, 73.45, 72.76, 66.71, 64.76, 64.58, 55.64, 14.10. FT-IR (ATR, cm^{-1}) 3078-2762, 1751, 1458, 1373, 1234, 1010, 872, 779. 90% yield.

P(NB-NHS)$_{89}$-*b*-P(NB-*g*-PGC$_{33}$)$_{5:}$ ^{1}H NMR (500 MHz, CDCl$_3$) δ ppm 5.34 (t, *J* = 10 Hz, C*H*=C*H*s from brush backbone), 5.01 (d, *J* = 4 Hz, C*H*OCH$_3$ in NB-PGC units), 4.83 (t, *J* = 10 Hz, C*H*OCO in NB-PGC units), 4.72 (m, OC*H*$_2$CH$_3$ in NB-PGC units), 4.27 – 4.11 (m, OC*H*$_2$CH$_3$ in NB-PGC units), 3.45 – 3.39 (s, OC*H*$_3$ in NB-PGC units), 2.82 (m, C*H*$_2$C*H*$_2$ from NHS units), 1.35 – 1.25 (m, CH$_2$C*H*$_3$ in NB-PGC units). ^{13}C NMR (126 MHz, CDCl$_3$) δ ppm 154.11, 154.09, 153.75, 96.35, 77.35, 77.01, 76.75, 73.70, 73.45, 72.76, 66.71, 64.80, 64.68, 64.58, 55.64, 55.43, 14.12. FT-IR (ATR, cm^{-1}) 2970, 1751, 1466, 1373, 1242, 1011, 872, 779. 87% yield.

P(NB-NHS)$_{26}$-*b*-P(NB-*g*-PGC$_{25}$)$_{5:}$ ^{1}H NMR (500 MHz, CDCl$_3$) δ ppm 5.35 (q, *J* = 9 Hz, C*H*=C*H*s from brush backbone), 5.03 (d, *J* = 4 Hz, C*H*OCH$_3$ in NB-PGC units), 4.85 (t, *J* = 10 Hz, C*H*OCO in NB-PGC units), 4.74 (d, *J* = 10 Hz, C*H*OCH$_3$ in NB-PGC units), 4.41 – 4.31 (m, OC*H*$_2$CH$_3$ in NB-PGC units), 4.29 – 4.21 (m, OC*H*$_2$CH$_3$ in NB-PGC units), 3.47 – 3.41 (s, OC*H*$_3$ in NB-PGC units), 2.82 (m, C*H*$_2$C*H*$_2$ from NHS units), 1.40 – 1.22 (m, CH$_2$C*H*$_3$ in NB-PGC units). ^{13}C NMR (126 MHz, CDCl$_3$) δ ppm 154.12, 153.78, 96.34, 77.35, 77.03, 76.71, 73.70, 73.43, 72.75, 66.72, 64.69, 64.60, 55.64, 30.94, 14.12. FT-IR (ATR, cm^{-1}) 2978, 1750, 1452, 1374, 1242, 1011, 872, 778. 85% yield.

P(NB-NHS)$_{59}$-*b*-P(NB-*g*-PGC$_{25}$)$_{5:}$ ^{1}H NMR (500 MHz, CDCl$_3$) δ ppm 5.03 (d, *J* = 4 Hz, C*H*OCH$_3$ in NB-PGC units), 4.88 – 4.81 (m, C*H*OCO in NB-PGC units), 4.74 (d, *J* = 10

Hz, CHOCH$_3$ in NB-PGC units), 4.34 (m, OCH_2CH$_3$ in NB-PGC units), 4.26 – 4.13 (m, OCH_2CH$_3$ in NB-PGC units), 3.44 (s, OCH_3 in NB-PGC units), 2.82 (m, CH_2CH_2 from NHS units), 1.40 – 1.23 (m, CH$_2$CH_3 in NB-PGC units). ^{13}C NMR (126 MHz, CDCl$_3$) δ ppm 154.10, 154.09, 153.76, 96.36, 77.26, 77.04, 76.75, 73.69, 73.45, 72.76, 66.70, 64.76, 64.68, 64.58, 55.64, 55.43, 14.11. FT-IR (ATR, cm^{-1}) 2980, 1751, 1450, 1373, 1234, 1011, 872, 780. 90% yield.

P(NB-NHS)$_{29}$-*b*-P(NB-*g*-PGC$_{17}$)$_3$: ^{1}H NMR (500 MHz, CDCl$_3$) δ ppm 5.36 (m, CH=CHs from brush backbone), 5.03 (m, CHOCH$_3$ in NB-PGC units), 4.85 (m, CHOCO in NB-PGC units), 4.74 (d, *J* = 10 Hz, CHOCH$_3$ in NB-PGC units), 4.33 (m, OCH_2CH$_3$ in NB-PGC units), 4.25 – 4.18 (m, OCH_2CH$_3$ in NB-PGC units), 3.50 (s, OCH_3 in NB-PGC units), 2.82 (m, CH_2CH_2 from NHS units), 1.36 – 1.26 (m, CH$_2$CH_3 in NB-PGC units). ^{13}C NMR (126 MHz, CDCl$_3$) δ ppm 154.11, 154.10, 153.76, 96.35, 77.26, 77.00, 76.75, 73.69, 72.76, 66.70, 64.76, 64.69, 64.58, 55.64, 14.11. FT-IR (ATR, cm^{-1}) 2980, 1750, 1451, 1373, 1242, 1010, 872, 779. 92% yield.

P(NB-NHS)$_{114}$-*b*-P(NB-*g*-PGC$_{17}$)$_7$: ^{1}H NMR (500 MHz, CDCl$_3$) δ ppm 5.32 (br, CH=CHs from brush backbone), 5.02 – 4.95 (m, CHOCH$_3$ in NB-PGC units), 4.82 – 4.68 (m, CHOCO in NB-PGC units), 4.34 – 4.28 (m, OCH_2CH in NB-PGC units), 4.22 – 4.15 (m, OCH_2CH$_3$ in NB-PGC units), 4.09 – 4.02 (m, CHCH(CH$_2$)O in NB-PGC units), 3.46 – 3.37 (s, OCH_3 in NB-PGC units), 2.82 (br, CH_2CH_2 from NHS units), 2.25 - 2.02 (m, CH_2s from PNB backbone), 1.35 – 1.23 (m, CH$_2$CH_3 in NB-PGC units). ^{13}C NMR (126 MHz, CDCl$_3$) δ ppm 154.11, 154.09, 153.76, 96.36, 77.26, 77.01, 76.75, 73.69, 73.45, 72.76, 66.71, 64.76, 64.68, 64.58, 55.64, 55.43, 14.10. FT-IR (ATR, cm^{-1}) 2978, 1751, 1450, 1380, 1242, 1011, 872, 779. 90% yield.

P(NB-NHS)$_{322}$-*b*-P(NB-*g*-PGC$_{20}$)$_{12}$: ^{1}H NMR (500 MHz, CDCl$_3$) δ ppm 5.35 – 5.27 (m, C*H*=C*H*s from brush backbone), 5.00 (d, *J* = 4 Hz, C*H*OCH$_3$ in NB-PGC units), 4.81 (t, *J* = 10 Hz, C*H*OCO in NB-PGC units), 4.30 (d, *J* = 12 Hz, OC*H*$_2$CH in NB-PGC units), 4.24 – 4.12 (m, OC*H*$_2$CH$_3$ in NB-PGC units), 4.04 (m, CHC*H*(CH$_2$)O in NB-PGC units), 3.43 – 3.38 (s, OC*H*$_3$ in NB-PGC units), 2.83 – 2.77 (m, C*H*$_2$C*H*$_2$ from NHS units), 2.19 – 2.09 (m, C*H*$_2$s from PNB backbone), 1.33 – 1.23 (m, CH$_2$C*H*$_3$ in NB-PGC units). ^{13}C NMR (126 MHz, CDCl$_3$) δ ppm 154.10, 154.10, 153.76, 96.40, 77.26, 77.01, 76.75, 73.69, 73.45, 72.76, 66.70, 64.76, 64.68, 64.58, 55.64, 14.10. FT-IR (ATR, cm^{-1}) 2982, 1751, 1450, 1373, 1234, 1011, 872, 780. 93% yield.

P(NB-NHS)$_{173}$-*b*-P(NB-*g*-PGC$_{25}$)$_5$: ^{1}H NMR (500 MHz, CDCl$_3$) δ ppm 5.35 (t, *J* = 10 Hz, C*H*=C*H*s from brush backbone), 5.03 (m, C*H*OCH$_3$ in NB-PGC units), 4.84 (t, *J* = 10 Hz, C*H*OCO in NB-PGC units), 4.33 (d, *J* = 12 Hz, OC*H*$_2$CH in NB-PGC units), 4.26 – 4.16 (m, OC*H*$_2$CH$_3$ in NB-PGC units), 4.06 (m, CHC*H*(CH$_2$)O in NB-PGC units), 3.43 (q, *J* = 2 Hz, OC*H*$_3$ in NB-PGC units), 2.82 (m, C*H*$_2$C*H*$_2$ from NHS units), 2.27 (m, C*H*$_2$s from PNB backbone), 1.34 – 1.18 (m, CH$_2$C*H*$_3$ in NB-PGC units). ^{13}C NMR (126 MHz, CDCl$_3$) δ ppm 154.11, 154.09, 153.76, 96.36, 77.26, 77.03, 76.75, 73.69, 73.43, 72.76, 64.76, 64.68, 64.60, 55.64, 55.43, 14.10. FT-IR (ATR, cm^{-1}) 2950, 1750, 1450, 1373, 1234, 1011, 872, 779. 90% yield.

P(NB-NHS)$_{143}$-*b*-P(NB-*g*-PGC$_{33}$)$_2$: ^{1}H NMR (500 MHz, CDCl$_3$) δ ppm 5.33 (d, *J* = 10 Hz, C*H*=C*H*s from brush backbone), 5.01 (d, *J* = 4 Hz, C*H*OCH$_3$ in NB-PGC units), 4.83 (dd, *J* = 12 Hz, C*H*OCO in NB-PGC units), 4.32 (d, *J* = 12 Hz, OCH_2CH in NB-PGC units), 4.27 – 4.12 (m, OCH_2CH_3 in NB-PGC units), 4.06 (dd, *J* = 11 Hz, m, CHC*H*(CH_2)O in NB-PGC units), 3.49 (s, OCH_3 in NB-PGC units), 2.82 (s, CH_2CH_2 from NHS units), 2.26 (m, CH_2s from PNB backbone), 1.29 - 1.17 (m, CH_2CH_3 in NB-PGC units). ^{13}C NMR (126 MHz, CDCl$_3$) δ ppm 154.10, 154.09, 153.76, 96.40, 77.26, 77.01, 76.75, 73.70, 73.45, 72.78, 66.71, 64.76, 64.68, 64.58, 55.65, 55.43, 14.11. FT-IR (ATR, cm^{-1}) 2981, 1751, 1450, 1372, 1242, 1008, 872, 779. 91% yield.

P(NB-NHS)$_{159}$-*b*-P(NB-*g*-PGC$_{18}$)$_7$: ^{1}H NMR (500 MHz, CDCl$_3$) δ ppm 5.33 (d, *J* = 10 Hz, C*H*=C*H*s from brush backbone), 5.04 – 4.96 (m, C*H*OCH_3 in NB-PGC units), 4.84 (q, *J* = 11 Hz, C*H*OCO in NB-PGC units), 4.31 (m, OCH_2CH in NB-PGC units), 4.27 – 4.12 (m, OCH_2CH_3 in NB-PGC units), 4.08 – 4.02 (m, CHC*H*(CH_2)O in NB-PGC units), 3.42 (s, OCH_3 in NB-PGC units), 2.82 (s, CH_2CH_2 from NHS units), 2.26 (s, CH_2s from PNB backbone), 1.29 (m, CH_2CH_3 in NB-PGC units). ^{13}C NMR (126 MHz, CDCl$_3$) δ ppm 154.10, 154.10, 153.76, 96.36, 77.30, 77.01, 76.76, 73.69, 73.45, 72.76, 66.72, 64.76, 64.68, 64.58, 55.65, 55.43, 14.11. FT-IR (ATR, cm^{-1}) 2980, 1751, 1451, 1373, 1237, 1010, 872, 780. 90% yield.

P(NB-NHS)$_{139}$-*b*-P(NB-*g*-PGC$_{17}$)$_4$: ^{1}H NMR (500 MHz, CDCl$_3$) δ ppm 5.57 (m, C*H*=C*H*s from brush backbone), 5.03 (d, *J* = 4 Hz, C*H*OCH_3 in NB-PGC units), 4.84 (t, *J* = 10 Hz, C*H*OCO in NB-PGC units), 4.27 – 4.13 (m, OCH_2CH_3 in NB-PGC units), 3.43 (s, OCH_3 in NB-PGC units), 2.82 (br, CH_2CH_2 from NHS units), 2.27 (m, CH_2s from PNB backbone), 1.36 – 1.27 (m, CH_2CH_3 in NB-PGC units). ^{13}C NMR (126 MHz, CDCl$_3$) δ ppm 154.12, 153.78, 96.34, 77.35, 77.01, 76.71, 73.70, 73.43, 72.75, 66.72, 64.69, 64.60, 55.64, 30.94, 14.12. FT-IR (ATR, cm^{-1}) 2982, 1751, 1448, 1373, 1234, 1011, 872, 779. 90% yield.

$P(NB-NHS)_{157}$-*b*-P(NB-*g*-$PGC_8)_{12}$: ^1H NMR (500 MHz, $CDCl_3$) δ ppm 5.56 (m, C*H*=C*H*s from brush backbone), 5.02 (d, *J* = 4 Hz, C*H*OCH_3 in NB-PGC units), 4.26 – 4.17 (m, OC$H_2$$CH_3$ in NB-PGC units), 3.42 (s, OCH_3 in NB-PGC units), 2.81 (m, CH_2CH_2 from NHS units), 1.34 – 1.18 (m, CH_2CH_3 in NB-PGC units). ^{13}C NMR (126 MHz, $CDCl_3$) δ ppm 154.11, 154.10, 153.76, 96.36, 77.30, 77.01, 76.75, 73.69, 73.45, 72.77, 66.71, 64.76, 64.70, 64.58, 55.64, 55.45, 14.10. FT-IR (ATR, cm^{-1}) 2981, 1750, 1450, 1373, 1242, 1010, 872, 779. 91% yield.

General Procedure for Hydrolysis of Coil-brush Block Polymers, P(NB-NHS)-b-P(NB-g-PGC(EC)), detailed for P(NB-NHS_{29})-*b*-P(NB-*g*-$PGC_{17})_3$. In a 10 mL Schlenk flask charged with a stir bar, P(NB-*g*-PGC(EC))-*b*-P(NB-NHS) (14 mg, 0.80 μmol) was dissolved in 5 mL DMF and *N,N*-diisopropylethylamine (DIPEA) (0.010 mL, 7.4 mg, 57 μmol) was added into the polymer solution. The reaction was allowed to stir overnight at rt and under nitrogen. After dialysis against nanopure water for three days, the product was isolated by lyophilization overnight to give a fluffy white solid (*ca.* 98% yield).

$P(NB-COOH)_{54}$-*b*-P(NB-*g*-$PGC_{33})_{5:}$: ^1H NMR (500 MHz, $CDCl_3$) δ ppm 5.34 (t, *J* = 9 Hz, C*H*=C*H*s from brush backbone), 5.01 (d, *J* = 4 Hz, C*H*OCH_3 in NB-PGC units), 4.84 (t, *J* = 9 Hz, C*H*OCO in NB-PGC units), 4.72 (m, OC$H_2$$CH_3$ in NB-PGC units), 4.19 (m, OC$H_2$$CH_3$ in NB-PGC units), 3.42 (s, OCH_3 in NB-PGC units), 2.19 (d, *J* = 1.0 Hz, CH_2s from PNB backbone), 1.29 (m, CH_2CH_3 in NB-PGC units). FT-IR (ATR, cm^{-1}) 3696 -

3071, 3071 - 2808, 1759, 1373, 1250, 1018, 872, 779. DSC: T_g = 93 °C, 116 °C. TGA in Ar: 225 - 322 °C, 58 % mass loss.

P(NB-COOH)$_{89}$-*b*-P(NB-*g*-PGC$_{33}$)$_5$: ^{1}H NMR (500 MHz, CDCl$_3$) δ ppm 5.33 (br, C*H*=C*H*s from brush backbone), 5.23 – 5.01 (m, C*H*OCH$_3$ in NB-PGC units), 4.82 – 4.72 ((m, C*H*OCO in NB-PGC units), 4.32 – 4.28 (m, OC*H*$_2$CH in NB-PGC units), 4.20 – 4.19 (m, OC*H*$_2$CH$_3$ in NB-PGC units), 4.05 – 4.02 (m, CHC*H*(CH$_2$)O in NB-PGC units), 3.66 – 3.41 (s, OC*H*$_3$ in NB-PGC units), 2.99 - 2.82 (m, C*H*$_2$s from PNB backbone), 1.29 – 1.23 (m, CH$_2$C*H*$_3$ in NB-PGC units). FT-IR (ATR, cm^{-1}) 3719 – 3101, 2970, 1751, 1458, 1366, 1234, 1026, 872, 779. DSC: T_g = 95 °C, 152 °C. TGA in Ar: 313 - 360 °C, 60% mass loss.

P(NB-COOH)$_{26}$-*b*-P(NB-*g*-PGC$_{25}$)$_{5:}$: ^{1}H NMR (500 MHz, CDCl$_3$) δ ppm 5.35 (q, *J* = 9 Hz, C*H*=C*H*s from brush backbone), 5.03 (d, *J* = 4 Hz, C*H*OCH$_3$ in NB-PGC units), 4.85 (t, *J* = 10 Hz, C*H*OCO in NB-PGC units), 4.74 (d, *J* = 10 Hz, C*H*OCH$_3$ in NB-PGC units), 4.41 – 4.31 (m, OC*H*$_2$CH$_3$ in NB-PGC units), 4.29 – 4.21 (m, OC*H*$_2$CH$_3$ in NB-PGC units), 3.47 – 3.41 (s, OC*H*$_3$ in NB-PGC units), 1.40 – 1.22 (m, CH$_2$C*H*$_3$ in NB-PGC units). FT-IR (ATR, cm^{-1}) 3711 – 2716, 2970, 1751, 1453, 1373, 1250, 1018, 880, 779. DSC: T_g = 93 °C, 125 °C. TGA in Ar: 230 - 350 °C, 55% mass loss.

P(NB-COOH)$_{59}$-*b*-P(NB-*g*-PGC$_{25}$)$_{5:}$ ^{1}H NMR (500 MHz, CDCl$_3$) δ ppm 5.03 (d, *J* = 4 Hz, C*H*OCH$_3$ in NB-PGC units), 4.88 – 4.81 (m, C*H*OCO in NB-PGC units), 4.74 (d, *J* = 10 Hz, C*H*OCH$_3$ in NB-PGC units), 4.34 (m, OC*H*$_2$CH$_3$ in NB-PGC units), 4.26 – 4.13 (m, OC*H*$_2$CH$_3$ in NB-PGC units), 3.44 (s, OC*H*$_3$ in NB-PGC units), 1.40 – 1.23 (m, CH$_2$C*H*$_3$

in NB-PGC units). FT-IR (ATR, cm^{-1}) 3742 – 2731, 2970, 1751, 1628, 1443, 1373, 1242, 1018, 872, 779. DSC: T_g = 94 °C, 126 °C. TGA in Ar: 250 - 355 °C, 53% mass loss.

P(NB-COOH)$_{29}$-*b*-P(NB-*g*-PGC$_{17}$)$_{3}$: ^{1}H NMR (500 MHz, CDCl$_3$) δ ppm 5.36 (m, C*H*=C*H*s from brush backbone), 5.03 (m, C*H*OCH$_3$ in NB-PGC units), 4.85 (m, C*H*OCO in NB-PGC units), 4.74 (d, *J* = 10 Hz, C*H*OCH$_3$ in NB-PGC units), 4.33 (m, OC*H*$_2$CH$_3$ in NB-PGC units), 4.25 – 4.18 (m, OC*H*$_2$CH$_3$ in NB-PGC units), 3.50 (s, OC*H*$_3$ in NB-PGC units), 1.36 – 1.26 (m, CH$_2$C*H*$_3$ in NB-PGC units). FT-IR (ATR, cm^{-1}) 3726 – 3074, 3074 – 2762, 2970, 1752, 1628, 1250, 1018, 872, 779, 656. DSC: T_g = 90 °C, 150 °C. TGA in Ar: 300 - 360 °C, 58% mass loss.

P(NB-COOH)$_{114}$-*b*-P(NB-*g*-PGC$_{17}$)$_7$: ^{1}H NMR (500 MHz, CDCl$_3$) δ ppm 5.32 (br, C*H*=C*H*s from brush backbone), 5.02 – 4.95 (m, C*H*OCH$_3$ in NB-PGC units), 4.82 – 4.68 (m, C*H*OCO in NB-PGC units), 4.34 – 4.28 (m, OC*H*$_2$CH in NB-PGC units), 4.22 – 4.15 (m, OC*H*$_2$CH$_3$ in NB-PGC units), 4.09 – 4.02 (m, CHC*H*(CH$_2$)O in NB-PGC units), 3.46 – 3.37 (s, OC*H*$_3$ in NB-PGC units), 2.25 - 2.02 (m, C*H*$_2$s from PNB backbone), 1.35 – 1.23 (m, CH$_2$C*H*$_3$ in NB-PGC units). FT-IR (ATR, cm^{-1}) 3711 – 2710, 1751, 1373, 1250, 1018, 871, 779, 640. DSC: T_g = 93 °C, 148 °C. TGA in Ar: 267 - 372 °C, 63% mass loss.

P(NB-COOH)$_{322}$-*b*-P(NB-*g*-PGC$_{20}$)$_{12}$: ^{1}H NMR (500 MHz, CDCl$_3$) δ ppm 5.35 – 5.27 (m, C*H*=C*H*s from brush backbone), 5.00 (d, *J* = 4 Hz, C*H*OCH$_3$ in NB-PGC units), 4.81 (t, *J* = 10 Hz, C*H*OCO in NB-PGC units), 4.30 (d, *J* = 12 Hz, OC*H*$_2$CH in NB-PGC units), 4.24 – 4.12 (m, OC*H*$_2$CH$_3$ in NB-PGC units), 4.04 (m, CHC*H*(CH$_2$)O in NB-PGC units), 3.43 – 3.38 (s, OC*H*$_3$ in NB-PGC units), 2.19 – 2.09 (m, C*H*$_2$s from PNB backbone), 1.33

– 1.23 (m, $\mathrm{CH_2C}\mathit{H}_3$ in NB-PGC units). FT-IR (ATR, cm^{-1}) 3703 - 3078, 3078 - 2777, 1743, 1458, 1373, 1242, 1018, 872, 779, 640. DSC: T_g = 93 °C, 115 °C. TGA in Ar: 234 - 363 °C, 76% mass loss.

P(NB-COOH)$_{173}$-*b*-P(NB-*g*-PGC$_{25}$)$_5$: ^{1}H NMR (500 MHz, $\mathrm{CDCl_3}$) δ ppm 5.35 (t, J = 10 Hz, $\mathrm{C}\mathit{H}\mathrm{=C}\mathit{H}$s from brush backbone), 5.03 (m, $\mathrm{C}\mathit{H}\mathrm{OCH_3}$ in NB-PGC units), 4.84 (t, J = 10 Hz, $\mathrm{C}\mathit{H}\mathrm{OCO}$ in NB-PGC units), 4.33 (d, J = 12 Hz, $\mathrm{OC}\mathit{H}_2\mathrm{CH}$ in NB-PGC units), 4.26 – 4.16 (m, $\mathrm{OC}\mathit{H}_2\mathrm{CH_3}$ in NB-PGC units), 4.06 (m, $\mathrm{CHC}\mathit{H}\mathrm{(CH_2)O}$ in NB-PGC units), 3.43 (q, J = 2 Hz, $\mathrm{OC}\mathit{H}_3$ in NB-PGC units), 2.27 (m, $\mathrm{C}\mathit{H}_2$s from PNB backbone), 1.34 – 1.18 (m, $\mathrm{CH_2C}\mathit{H}_3$ in NB-PGC units). ^{13}C NMR (126 MHz, $\mathrm{CDCl_3}$) δ ppm 154.11, 154.09, 153.76, 96.36, 77.26, 77.03, 76.75, 73.69, 73.43, 72.76, 64.76, 64.68. FT-IR (ATR, cm^{-1}) 3742 - 2731, 1744, 1458, 1380, 1250, 1018, 872, 779. DSC: T_g = 95 °C, 126 °C. TGA in Ar: 242 - 360 °C, 51% mass loss.

P(NB-COOH)$_{143}$-*b*-P(NB-*g*-PGC$_{33}$)$_2$: ^{1}H NMR (500 MHz, $\mathrm{CDCl_3}$) δ ppm 5.33 (d, J = 10 Hz, $\mathrm{C}\mathit{H}\mathrm{=C}\mathit{H}$s from brush backbone), 5.01 (d, J = 4 Hz, $\mathrm{C}\mathit{H}\mathrm{OCH_3}$ in NB-PGC units), 4.83 (dd, J = 12 Hz, $\mathrm{C}\mathit{H}\mathrm{OCO}$ in NB-PGC units), 4.32 (d, J = 12 Hz, $\mathrm{OC}\mathit{H}_2\mathrm{CH}$ in NB-PGC units), 4.27 – 4.12 (m, $\mathrm{OC}\mathit{H}_2\mathrm{CH_3}$ in NB-PGC units), 4.06 (dd, J = 11 Hz, m, $\mathrm{CHC}\mathit{H}\mathrm{(CH_2)O}$ in NB-PGC units), 3.49 (s, $\mathrm{OC}\mathit{H}_3$ in NB-PGC units), 2.26 (m, $\mathrm{C}\mathit{H}_2$s from PNB backbone), 1.29 - 1.17 (m, $\mathrm{CH_2C}\mathit{H}_3$ in NB-PGC units). FT-IR (ATR, cm^{-1}) 3734 - 2462, 1744, 1450, 1373, 1242, 1011, 872, 779, 640. DSC: T_g = 101 °C, 141 °C. TGA in Ar: 251 - 344 °C, 61% mass loss.

P(NB-COOH)$_{159}$-*b*-P(NB-*g*-PGC$_{18}$)$_7$: ^{1}H NMR (500 MHz, $\mathrm{CDCl_3}$) δ ppm 5.33 (d, J = 10 Hz, $\mathrm{C}\mathit{H}\mathrm{=C}\mathit{H}$s from brush backbone), 5.04 – 4.96 (m, $\mathrm{C}\mathit{H}\mathrm{OCH_3}$ in NB-PGC units), 4.84 (q,

J = 11 Hz, CHOCO in NB-PGC units), 4.31 (m, OCH_2CH in NB-PGC units), 4.27 – 4.12 (m, OCH_2CH$_3$ in NB-PGC units), 4.08 – 4.02 (m, CHCH(CH$_2$)O in NB-PGC units), 3.42 (s, OCH_3 in NB-PGC units), 2.26 (s, CH_2s from PNB backbone), 1.29 (m, CH$_2$CH_3 in NB-PGC units). FT-IR (ATR, cm^{-1}) 3726 - 3078, 2974, 1751, 1250, 1018, 779. DSC: T_g = 97 °C, 153 °C. TGA in Ar: 260 - 373 °C, 64% mass loss.

P(NB-COOH)$_{139}$-*b*-P(NB-*g*-PGC$_{17}$)$_4$: ^{1}H NMR (500 MHz, CDCl$_3$) δ ppm 5.57 (m, CH=CHs from brush backbone), 5.03 (d, J = 4 Hz, CHOCH$_3$ in NB-PGC units), 4.84 (t, J = 10 Hz, CHOCO in NB-PGC units), 4.27 – 4.13 (m, OCH_2CH$_3$ in NB-PGC units), 3.43 (s, OCH_3 in NB-PGC units), 2.27 (m, CH_2s from PNB backbone), 1.36 – 1.27 (m, CH$_2$CH_3 in NB-PGC units). FT-IR (ATR, cm^{-1}) 3749 – 3093, 2940, 1744, 1234, 1018, 872, 779. DSC: T_g = 95 °C, 144 °C. TGA in Ar: 242 - 352 °C, 64% mass loss.

P(NB-COOH)$_{157}$-*b*-P(NB-*g*-PGC$_8$)$_{12}$: : ^{1}H NMR (500 MHz, CDCl$_3$) δ ppm 5.56 (m, CH=CHs from brush backbone), 5.02 (d, J = 4 Hz, CHOCH$_3$ in NB-PGC units), 4.26 – 4.17 (m, OCH_2CH$_3$ in NB-PGC units), 3.42 (s, OCH_3 in NB-PGC units), 2.81 (m, CH_2CH_2 from NHS units), 1.34 – 1.18 (m, CH$_2$CH_3 in NB-PGC units). FT-IR (ATR, cm^{-1}) FT-IR (ATR, cm^{-1}) 3750 – 3078, 2986, 1751, 1373, 1234, 1018, 871, 779. DSC: T_g = 97 °C, 126 °C. TGA in Ar: 225 - 441 °C, 73% mass loss.

Nanostructure Formation by Supramolecular Assembly in Solution. Each polymer sample was dissolved into DMF to give a 1 mg/mL solution, which was then transferred into presoaked dialysis membrane tubing (MWCO *ca.* 6-8 kDa) and dialyzed against nanopure water for three days at rt. The addition of water induced the assembly and stabilized the formed nanostructures.

Results and Discussions

Coil-brush block polymers were synthesized and assembled to yield core-degradable nano-objects in aqueous media with functionalizable coronas. ROP of cyclic glucose carbonates was initiated by a norbornene-functionalized alcohol to afford a series of norbornene-terminated PGC macromonomers, followed by sequential ROMP of a norbornenyl-functionalized NHS ester monomer and the norbornene-terminated PGC macromonomers to achieve the well-defined coil-brush architecture with high grafting efficiency and tunable chemical compositions. Hydrolysis of the NHS groups generated amphiphilic coil-brush block polymers that assembled in aqueous solutions into various nanoscopic morphologies. Several compositional parameters, such as hydrophilic(phobic) weight percentage, block ratio, and side chain length were investigated to study their

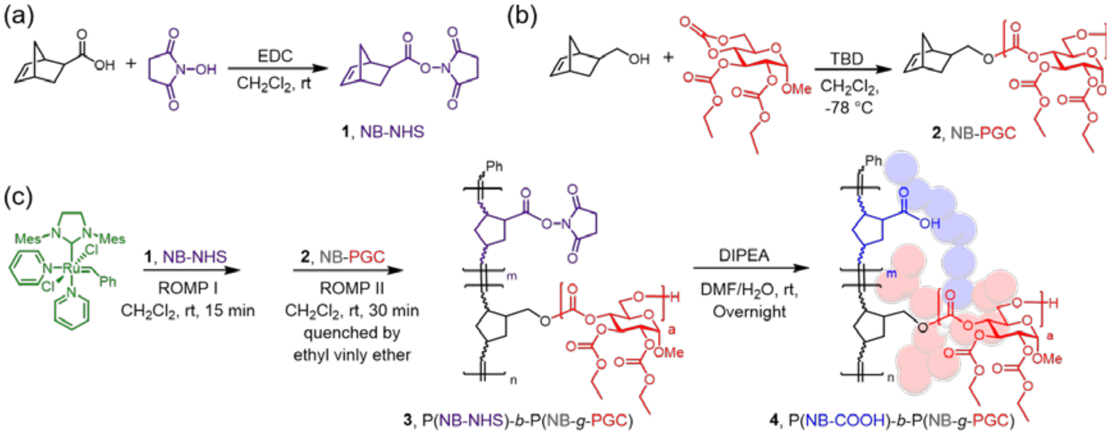

Scheme III-1 (a) Synthesis of norbornenyl-functionalized NHS ester **1**, NB-NHS, (b) polymerization of glucose carbonates to afford NB-PGC$_a$, **2**, and (c) one-pot sequential ROMP of **1** and **2**, followed by hydrolysis, to afford amphiphilic coil-brush block polymers **4**, P(NB-COOH)$_m$-*b*-P(NB-*g*-PGC$_a$)$_n$.

individual and combined effects on the self-assembly behavior of coil-brush block polymers in aqueous media.

Synthesis of P(NB-COOH)-b-P(NB-g-PGC) Coil-brush Block Polymers. As shown in **Scheme III-1**, the synthesis of amphiphilic PGC-based coil-brush block polymers were achieved in four consecutive steps. Firstly, norbornenyl-functionalized NHS ester **1** (NB-NHS) was synthesized in 83% yield by carbodiimide-mediated coupling of *exo*-norbornene carboxylic acid and NHS in dichloromethane at room temperature followed by purification by flash chromatography. The structure was confirmed by electrospray ionization mass spectrometry (ESI-MS), and Fourier-transform infrared, ^{1}H and ^{13}C NMR spectroscopies (**Figure III-1**). Secondly, a series of hydrophobic norbornene-terminated macromonomers **2** (**Table III-1**) with different chain lengths was synthesized by

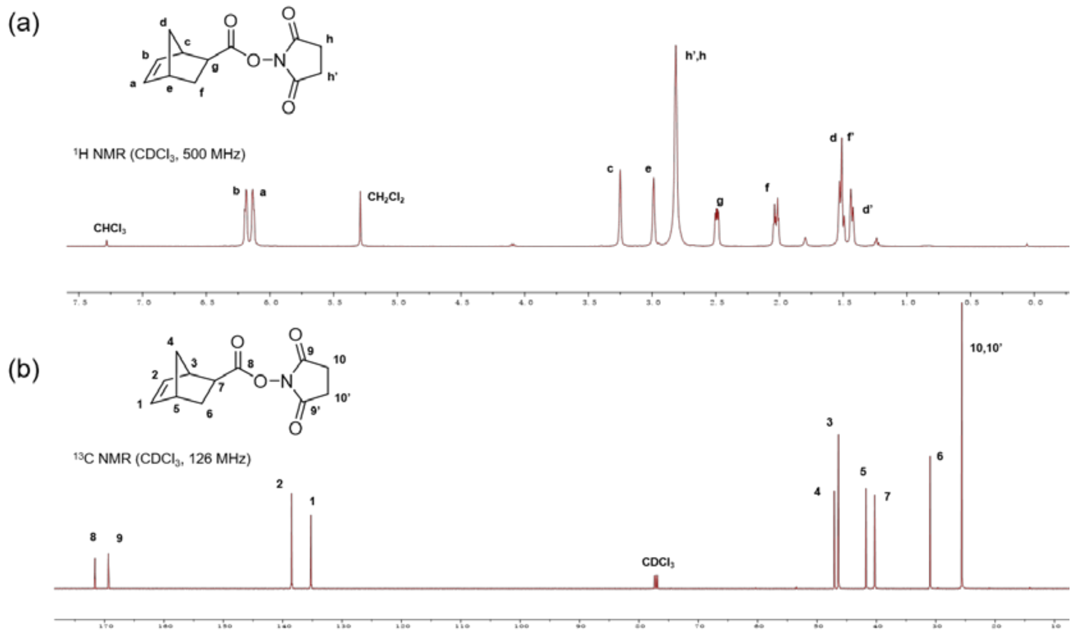

Figure III-1 ^{1}H NMR (500 MHz) and ^{13}C NMR (126 MHz) spectra of NB-NHS, **1**, in $CDCl_3$.

organocatalyzed ROP of the bicyclic D-glucose-based carbonate monomer, methyl-2,3-*O*-ethyloxycarbonyl-4,6-*O*-carbonyl-α-D-glucopyranoside, at -78 °C using *exo*-5-norbornene-2-methanol as the initiator, according to a previously established procedure.[75] The resulting macromonomers were shown to have monomodal molar mass dispersities ($Đ < 1.1$) according to size exclusion chromatography (SEC) (**Figure III-2**). The molar masses were additionally determined by end group analysis from ^{1}H NMR spectroscopy (**Figure III-3**) and by matrix-assisted laser desorption/ionization-time of flight (MALDI-TOF) mass spectrometry (**Figure III-4**). MALDI-TOF further confirmed the fidelity of the ROP and the presence of the norbornenyl-containing α-chain end. Thermal properties were evaluated by thermogravimetric analysis (TGA) and differential

Table III-1 Characterization data of NB-PGC$_a$ macromonomers **2**

Entry	DP_n[a]	$M_{n\ NMR}$[a] (kDa)	$M_{n\ SEC}$[b] (kDa)	$Đ$[b]
a	8	3.0	3.3	1.02
b	17	6.3	4.9	1.04
c	18	6.7	6.3	1.01
d	20	7.4	8.2	1.05
e	25	9.2	10.1	1.01
f	33	12.1	11.8	1.02

[a] Calculated from the monomer to initiator ratio based on ^{1}H NMR spectroscopy

[b] Measured by THF SEC calibrated using polystyrene standards

scanning calorimetry (DSC) (**Figure III-5**, **III-6**). Thirdly, sequential one-pot ROMP was performed at room temperature *via* the rapid addition of Grubbs' Generation 3 (G3) catalyst as a solution in dichloromethane into a stock solution of coil-block precursor **1**, followed *ca*. 15 min later by the quick addition of a relatively more concentrated solution of brush-block precursor macromonomer **2**. The polymerizations were quenched by addition of ethyl vinyl ether 30 min after the macromonomer addition had occurred. These

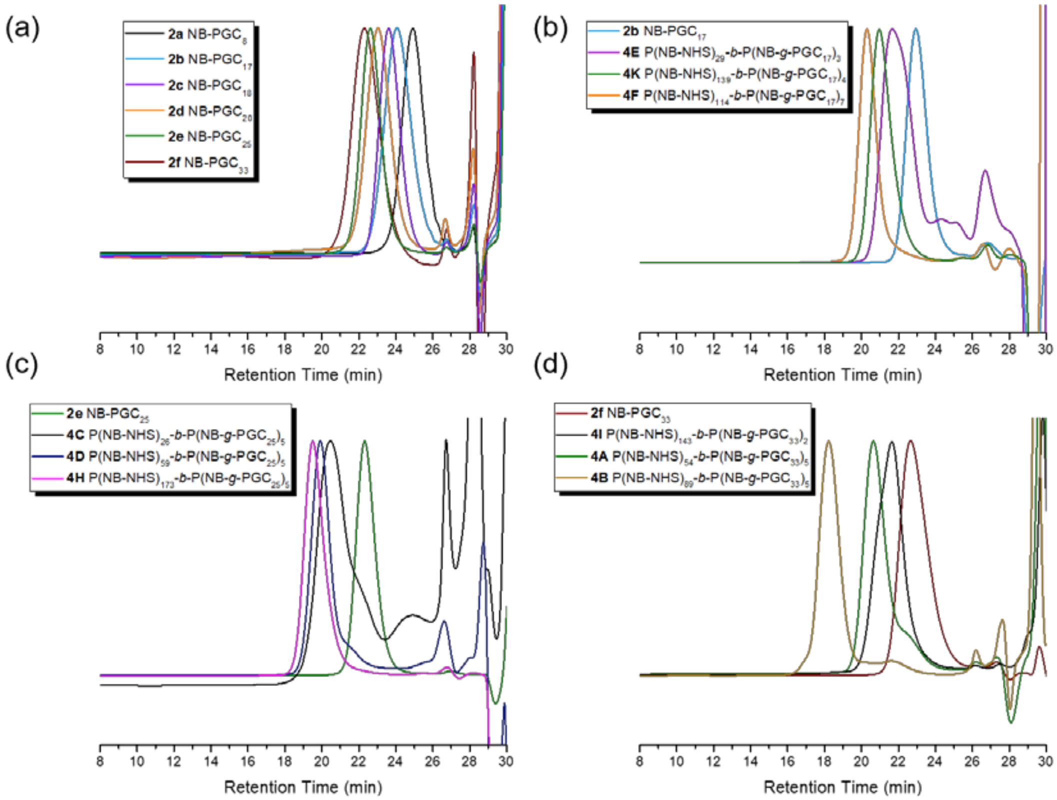

Figure III-2 Normalized SEC (THF eluent) traces of the (a) macromonomers NB-PGC$_a$, **2**, and (b, c, d) coil-brush block polymers P(NB-NHS)$_m$-*b*-P(NB-*g*-PGC$_a$)$_n$, **3**, compared to the corresponding macromonomers with different degrees of polymerization (DP_a).

efficient polymerizations provided facile access to various coil-brush block polymers with low dispersities (*Đ* < 1.2) (**Figure III-2b - d**), containing a linear NHS ester-functionalized block connected to a hydrophobic bottlebrush. The lengths of the two blocks were controlled by adjusting the feed ratio between the (macro)monomers and Grubbs' G3 catalyst. Finally, to produce hydrophilic coil segments and enable supramolecular assembly in water, the NHS groups were cleaved by hydrolysis in a mixture of water and DMF containing *N*,*N*-diisopropylethylamine (DIPEA), allowed to stir overnight at room temperature. The reaction mixtures were then transferred to dialysis tubings and dialyzed against nanopure water for at least three days, followed by being lyophilized to afford the final amphiphilic coil-brush polymers **A-L**. ^{1}H NMR and FT-IR spectroscopies

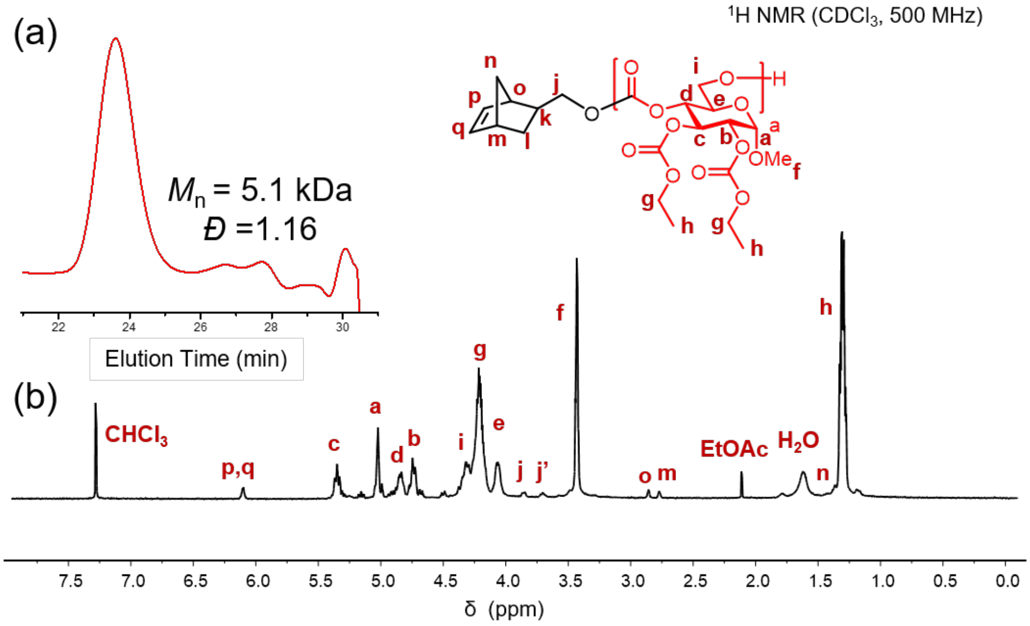

Figure III-3 (a) SEC trace (THF as eluent, 1 mL/min) and (b) ^{1}H NMR (500 MHz, CDCl$_3$) spectrum of norbornene-terminated macromonomer 2b, NB-PGC$_{17}$.

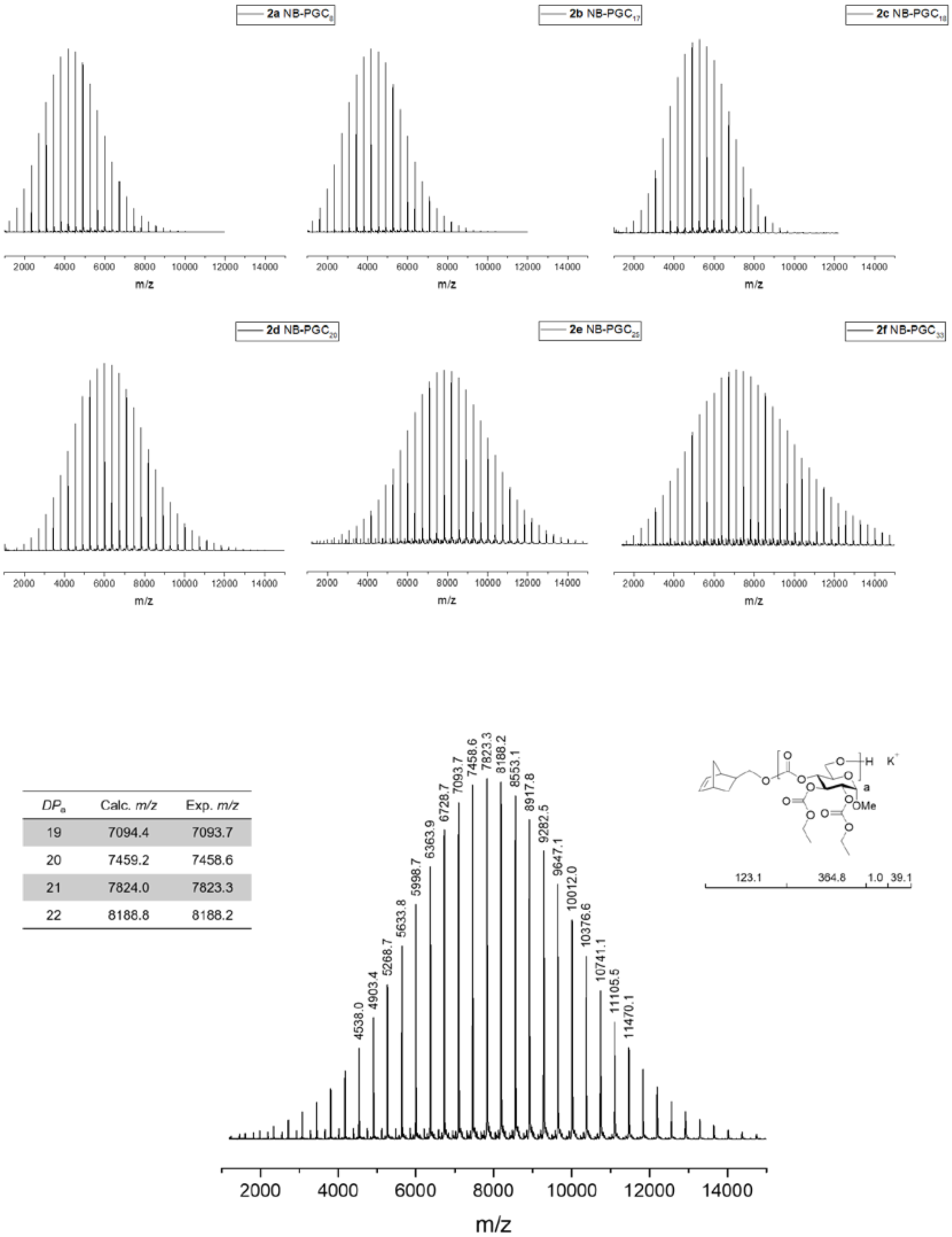

DP_a	Calc. *m/z*	Exp. *m/z*
19	7094.4	7093.7
20	7459.2	7458.6
21	7824.0	7823.3
22	8188.8	8188.2

Figure III-4 MALDI-TOF MS spectra of macromonomer NB-PGC$_a$, **2**. DCTB and KTFA were used as a matrix and cationization reagent, respectively.

confirmed the complete consumption of the NHS esters by showing that the proton NMR resonance at 2.82 ppm disappeared and a broad O-H stretch appeared from 3745 to 2756 cm^{-1} (**Figure III-7**). Taken together, these results demonstrate the successful synthesis of coil-brush block polymers composed of a coil block of hydrophilic norbornene carboxylic acid units and a bottlebrush block of hydrophobic poly(glucose carbonate)-grafted polynorbornene (**Table III-2**). Notably, the NHS-functionalized precursor is anticipated to enable diversification of these coil-brush block polymers with a variety of amine-terminated moieties. The combination of ROP, "grafting-through" ROMP, and post-polymerization modification strategies for the hydrophobic and hydrophilic segments provided significant structural control and simultaneous incorporation of multiple functional moieties.

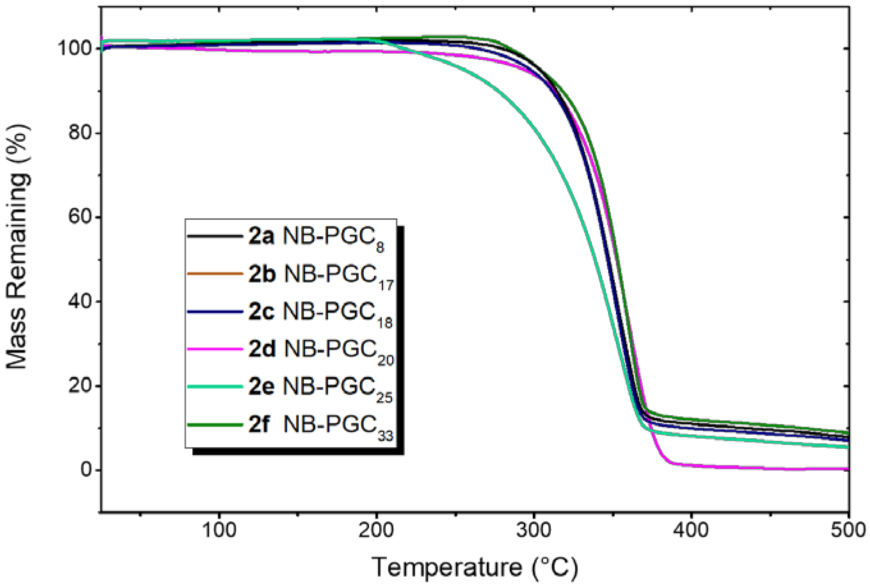

Figure III-5 TGA traces obtained under Ar atmosphere with a heating rate of 10 °C/min for macromonomers NB-PGC$_a$, **2**.

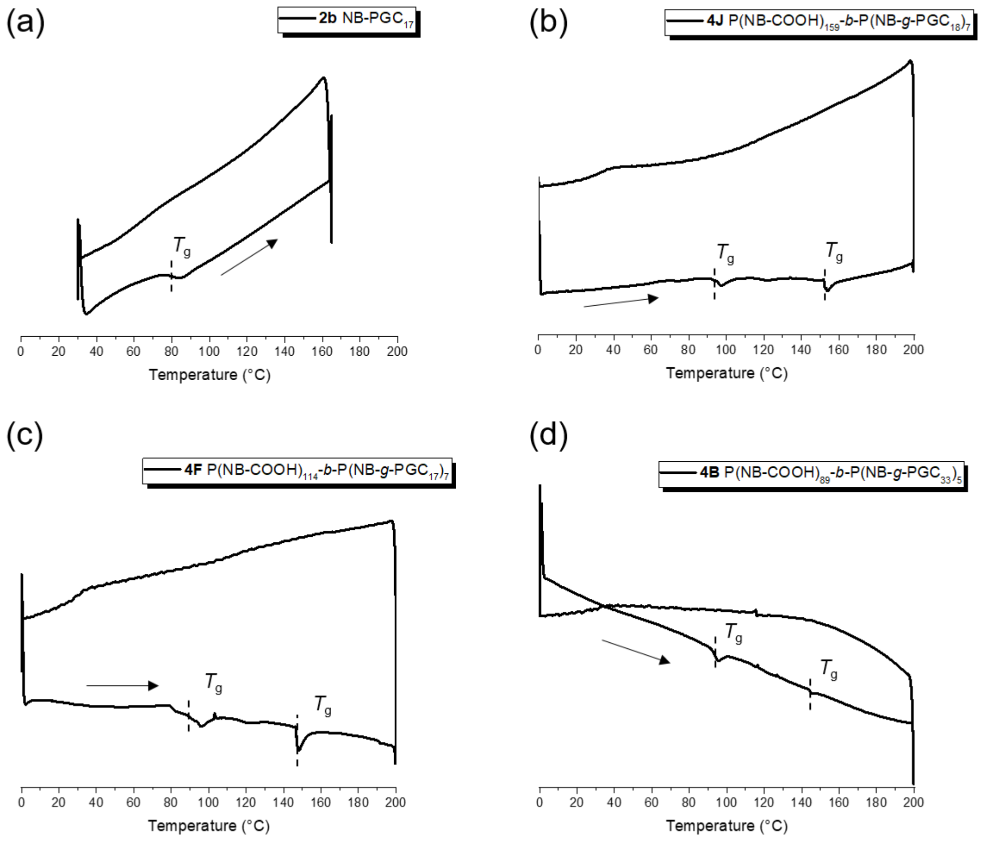

Figure III-6 DSC traces obtained under N_2 atmosphere with a heating and cooling rate of 10 °C/min of selected macromonomer NB-PGC_{17}, and coil-brush block polymers, **J** P(NB-COOH)$_{159}$-*b*-P(NB-PGC_{18})$_7$, **F** P(NB-COOH)$_{114}$-*b*-P(NB-PGC_{17})$_7$, and **B** P(NB-COOH)$_{89}$-*b*-P(NB-PGC_{33})$_5$. Glass transition temperatures (T_g) are labeled on the thermograms. Arrows indicate the direction of temperature ramping.

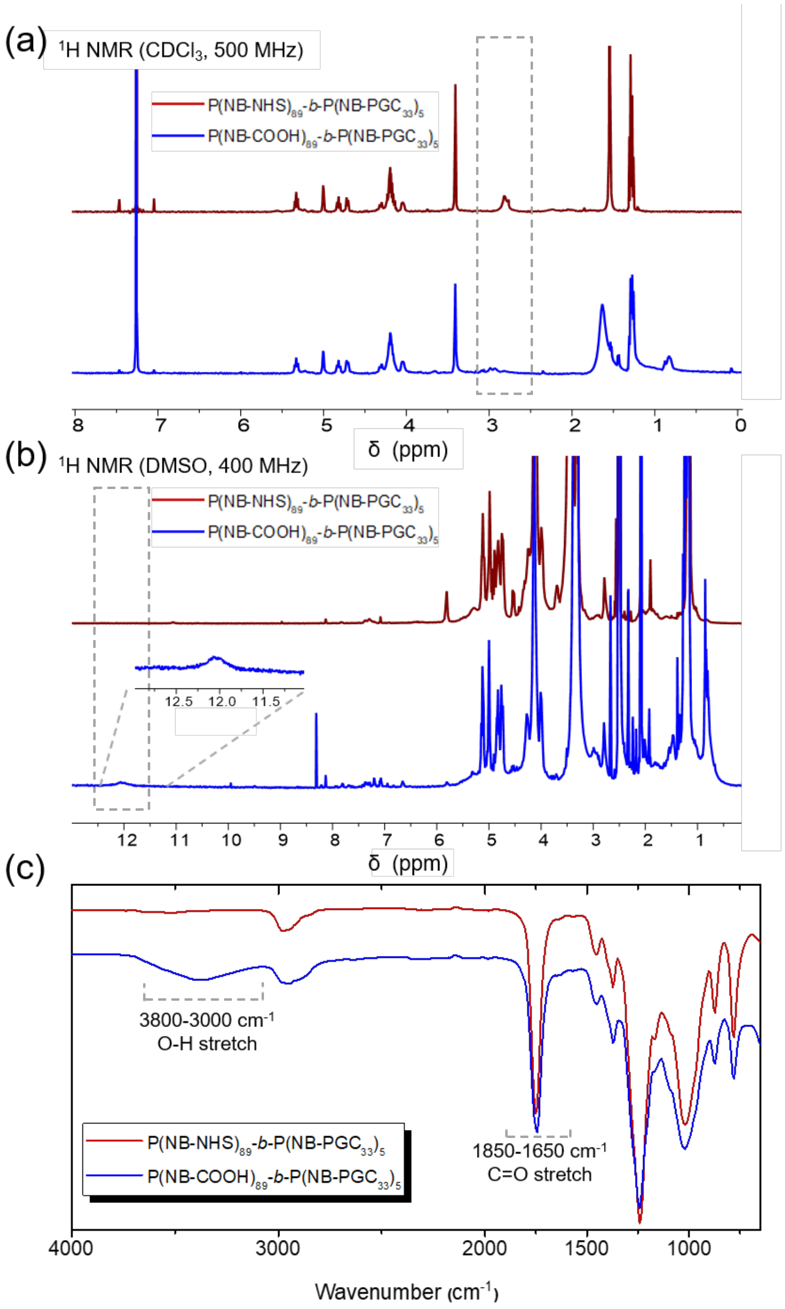

Figure III-7 (a) ^{1}H NMR (CDCl$_3$, 500 MHz) and (b) ^{1}H NMR (DMSO-d$_6$, 400 MHz) spectra, as well as (c) FT-IR spectra of coil-brush block polymers before (red line) and after hydrolysis (blue line), showing the proton NMR resonance at 2.82 ppm in CDCl$_3$ and at 12.04 ppm in DMSO-d$_6$ disappeared and appeared, respectively, as well as the appearance of a broad O-H stretch from 3745 to 2756 cm^{-1}.

Table III-2 Characterization data of P(NB-COOH)$_m$-*b*-P(NB-*g*-PGC$_a$)$_n$ coil-brush polymers **4**

	Coil-brush Block Polymers	A/G[a]	$M_{n\,\mathrm{NMR}}$[b] (kDa)	$M_{n\,\mathrm{SEC}}$[b,c] (kDa)	Đ[c]	Hydrophilic weight percentage (%)
A	P(NB-COOH)$_{54}$-*b*-P(NB-*g*-PGC$_{33}$)$_5$[d]	0.33	73.4	69.4	1.06	11
B	P(NB-COOH)$_{89}$-*b*-P(NB-*g*-PGC$_{33}$)$_5$	0.54	81.6	106	1.02	17
C	P(NB-COOH)$_{26}$-*b*-P(NB-*g*-PGC$_{25}$)$_5$	0.21	52.2	38.9	1.06	7
D	P(NB-COOH)$_{59}$-*b*-P(NB-*g*-PGC$_{25}$)$_5$	0.47	60.0	58.9	1.05	15
E	P(NB-COOH)$_{29}$-*b*-P(NB-*g*-PGC$_{17}$)$_3$	0.56	25.8	15.8	1.06	17
F	P(NB-COOH)$_{114}$-*b*-P(NB-*g*-PGC$_{17}$)$_7$	0.96	71.0	52.6	1.02	26
G	P(NB-COOH)$_{322}$-*b*-P(NB-*g*-PGC$_{20}$)$_{12}$	1.34	165.0	139	1.09	33
H	P(NB-COOH)$_{173}$-*b*-P(NB-*g*-PGC$_{25}$)$_5$	1.38	86.8	107	1.02	34
I	P(NB-COOH)$_{143}$-*b*-P(NB-*g*-PGC$_{33}$)$_2$	2.16	57.9	55.1	1.09	45
J	P(NB-COOH)$_{159}$-*b*-P(NB-*g*-PGC$_{18}$)$_7$	1.26	84.1	98.0	1.07	32
K	P(NB-COOH)$_{139}$-*b*-P(NB-*g*-PGC$_{17}$)$_4$	2.04	57.9	37.8	1.03	43
L	P(NB-COOH)$_{157}$-*b*-P(NB-*g*-PGC$_8$)$_{12}$	1.64	73.3	103	1.04	37

[a] Molar ratio of carboxylic acid units to glucose carbonates units, calculated by comparing the peak integrals of NHS proton resonances with methyl group proton resonances from glucose carbonate repeating units, based on ^{1}H NMR spectra.

[b] Molar masses here refer to the molar masses of the coil-brush block polymers having NHS groups.

[c] Measured by THF SEC equipped with a multi-angle laser light scattering (MALLS) detector.

[d] DP_ns were calculated by comparing the peak integrals from the corresponding characteristic proton resonances from each block.

Although the architecture of the coil-brush block polymer is complex, the hydrophilic-hydrophobic balance was hypothesized to be the main factor governing the assembly behavior. We introduced the parameter A/G, *i.e.*, molar ratio of carboxylic acid units to glucose carbonate units, $\frac{m}{a\times n}$, to express the hydrophilic/hydrophobic content of the coil-brush block polymers, for evaluation of the self-assembly. The A/G ratio is calculated by comparing the integrals of the proton resonances of the methylene groups of the NHS esters (δ = 2.82 ppm) with those of the methyl groups of the glucose carbonates (δ = 1.29 ppm) (**Figure III-8**).

Aqueous Solution Assembly of P(NB-COOH)-b-P(NB-g-PGC) Asymmetric Amphiphilic Coil-brush Block Polymers. Aqueous assembly of the well-defined coil-brush block polymers at various A/G ratios and PGC side chain lengths was investigated using a dialysis-based solvent exchange process. In a typical experiment, coil-brush block polymers were dissolved in DMF at 1 mg/mL at room temperature, followed by extensive dialysis against nanopure water for three days. A strong Tyndall light scattering path was observed, suggesting the existence of assemblies. The size and morphology of the resulting nanostructures were characterized quantitatively by dynamic light scattering (DLS) and transmission electron microscopy (TEM). Assembly results were observed for all coil-brush block polymers, where a clear morphological transition between spherical micelles, long cylindrical nanostructures, and bilayer vesicles can be visualized by changing block polymer composition, *i.e.,* polymeric side chain lengths and overall hydrophilic/hydrophobic ratio.

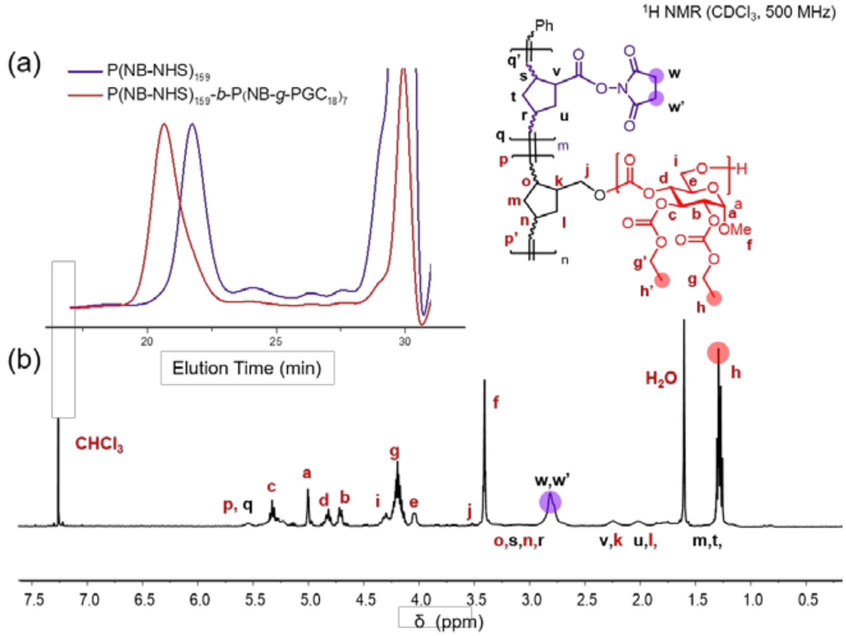

Figure III-8 (a) Normalized SEC traces (THF as eluent, 1 mL/min) and (b) ^{1}H NMR (500 MHz, $CDCl_3$) spectrum of the sequential ROMP for preparation of coil-brush block polymer P(NB-NHS)$_{159}$-*b*-P(NB-*g*-PGC$_{18}$)$_7$.

Adjusting the Morphology by Changing the A/G Ratio and Brush Side Chain Length. As shown in the TEM images, vesicular structures with an average diameter of 125 ± 14 nm and membrane thickness of 15 ± 5 nm (**Figure III-9b** and **III-9c**) were observed from coil-brush block polymer **A**, P(NB-COOH)$_{54}$-*b*-P(NB-*g*-PGC$_{33}$)$_5$, with a relatively low A/G ratio, 0.33, and long PGC side chains with a degree of polymerization (DP_n) of 33. The vesicular morphology was further supported by AFM illustrating apparent collapse on the substrate and cryo-TEM imaging with observation of a double-layered structure (**Figure III-10**). Maintaining the same side chain length, spherical micelles with an average diameter of 28 ± 5 nm as measured by TEM (**Figure III-9e**, **III-9f**) and height of *ca*. 3.5 ± 1.0 nm as measured by AFM (**Figure III-11**) were obtained from coil-brush block polymer **I**, $P(NB\text{-}COOH)_{143}\text{-}b\text{-}P(NB\text{-}g\text{-}PGC_{33})_2$, upon increasing the hydrophilic weight percentage to A/G = 2.16. The larger diameter relative to the height is expected to result from deformation of the particles upon adsorption onto the solid substrates for analyses. DLS showed unimodal size distributions of the vesicles and spheres, with number-average hydrodynamic diameters ($D_{h(number)}$) of 150 ± 50 nm and 60 ± 20 nm, respectively (**Figure III-12**). The difference between absolute particle diameter values between DLS and TEM data could be attributed to the differences between their hydrated

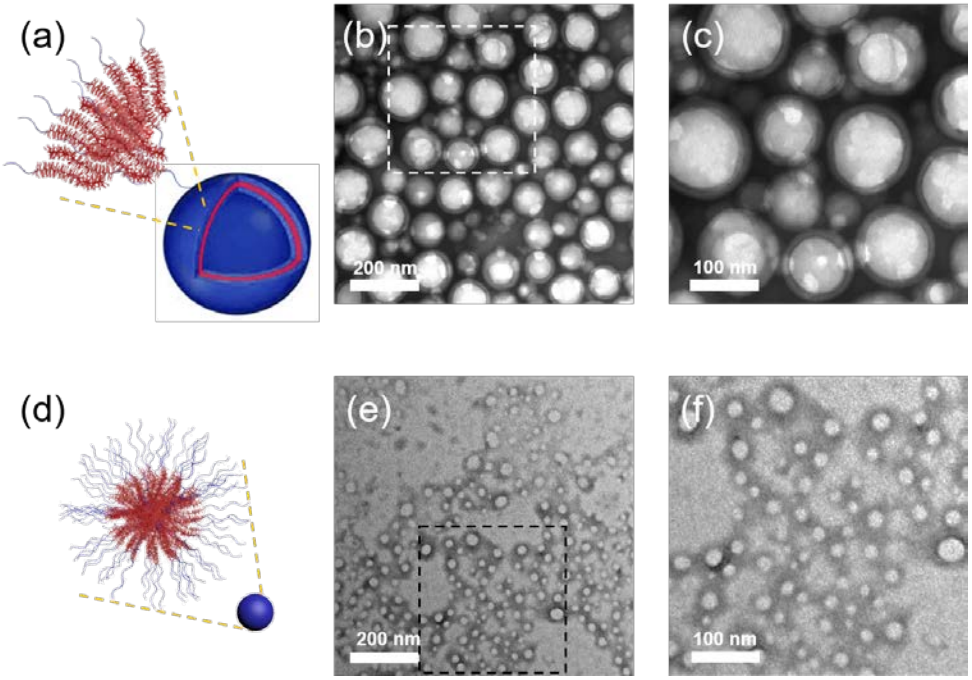

Figure III-9 TEM analysis of assemblies obtained from coil-brush block polymers **A** (b), (c) and **I** (e), (f). TEM samples were negatively stained with 1 wt% phosphotungstic acid aqueous solution (20 µL), and diameters were measured by counting > 50 nanoparticles. Schematic illustrations of vesicles (a) and spherical micelles (d) composed of coil-brushes.

structure in the solvated state as measured by DLS and their structure in the dry state upon deposition onto a solid carbon-coated copper grid substrate as measured by TEM, especially when these nanoassemblies are formed by coil-brush block polymers with flexible hydrophilic segments and stiff hydrophobic segments. The morphological

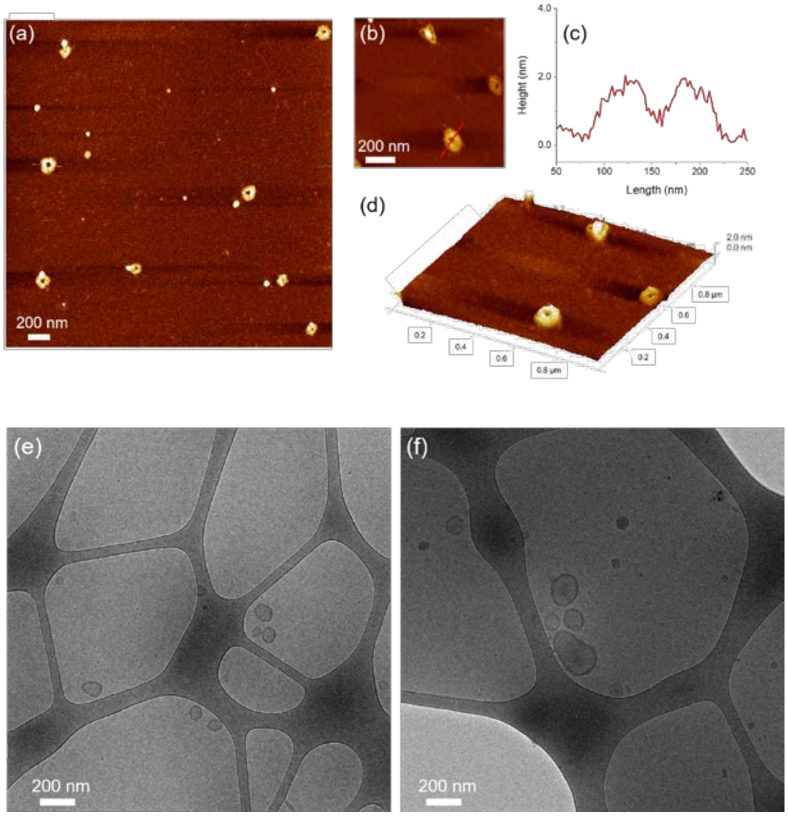

Figure III-10 AFM micrographs (a), (b), height profile (c), 3D image (d) of collapsed vesicles in dry state, and CryoTEM images (e), (f) of vesicles in a frozen-hydrated state obtained from an aqueous solution of coil-brush block polymer **B**, P(NB-COOH)$_{89}$-*b*-P(NB-*g*-PGC$_{33}$)$_5$. For AFM characterization, the sample solution was deposited on to freshly cleaved mica, spin coated, and then dried *in vacuo*. The height profiles were measured along the red line shown on the micrographs. For CryoTEM characterization, a droplet of polymer solution was deposited onto a plasma-treated lacey carbon grid, and then quickly plunged into a liquid ethane reservoir. The grids were then transferred to liquid nitrogen until the imaging. The temperature was maintained at -176 °C during the imaging to prevent ice crystallization. Scale bars = 200 nm.

variation between vesicular assemblies and spherical micelles may be due to a larger volume fraction of hydrophilic coil blocks, or coronal chains, of coil-brush **I** in aqueous solution, relative to **A**.

Vesicular structures were also dominant in coil-brush **B**, P(NB-COOH)$_{89}$-*b*-P(NB-*g*-PGC$_{33}$)$_{5}$, mainly due to the relatively long brush side chains and a similar A/G ratio compared to **A**. With similar A/G ratios of coil-brush block polymers **B** and **E**, P(NB-COOH)$_{29}$-*b*-P(NB-*g*-PGC$_{17}$)$_{3}$, *i.e.*, A/G ratios = 0.54 and 0.56,

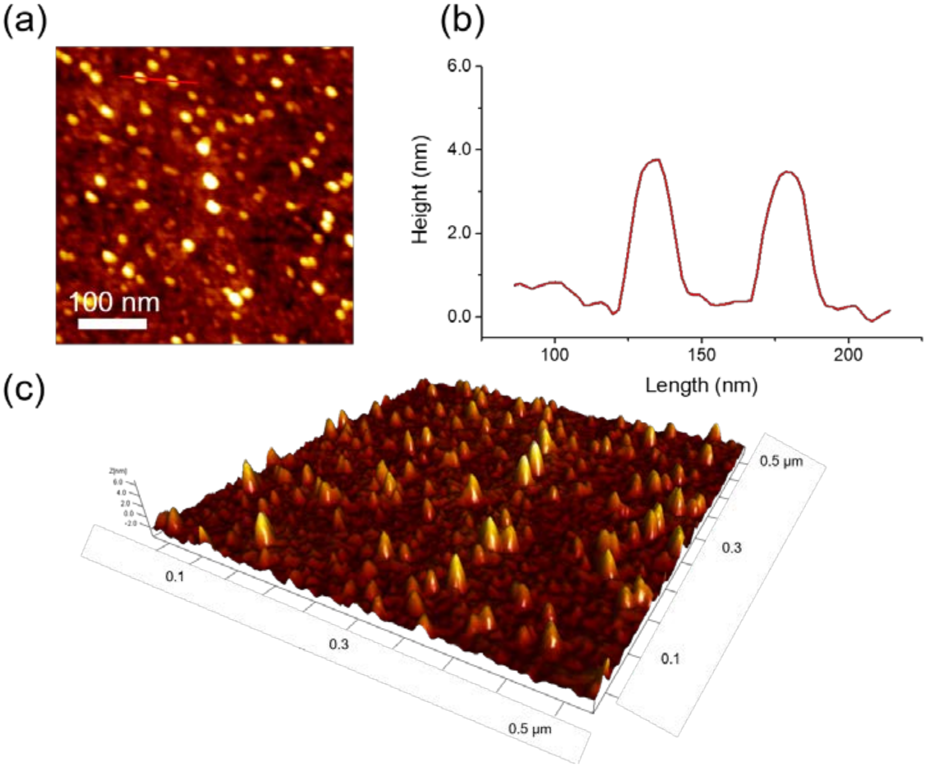

Figure III-11 AFM micrographs (a), height profile (b), 3D image (c) of nanoassemblies obtained from coil-brush block polymers **I**, P(NB-COOH)$_{143}$-*b*-P(NB-*g*-PGC$_{33}$)$_{2}$. For AFM characterization, the sample solution was drop cast onto the freshly cleaved mica and then dried in air. The height profiles were measured along the red line shown on the micrographs.

respectively, the lengths of their hydrophobic brush side chains varied markedly. As the DP_n of the grafted hydrophobic side chains decreased from 33 (**B**) to 17 (**E**), long cylindrical nanostructures with a width of 8 ± 1 nm were observed by TEM (**Figure III-13b**, **III-13c**, **Figure III-14**) and AFM (**Figure III-15**). It is inferred that these long cylindrical micelles result from an arrangement where polymer chains adopted more curved interfaces between coil segments and brush segments than vesicular structures, which would be caused by shorter hydrophobic brush side chains, or a smaller core volume fraction in aqueous solution. Additionally, pearl necklace-like nanostructures were found

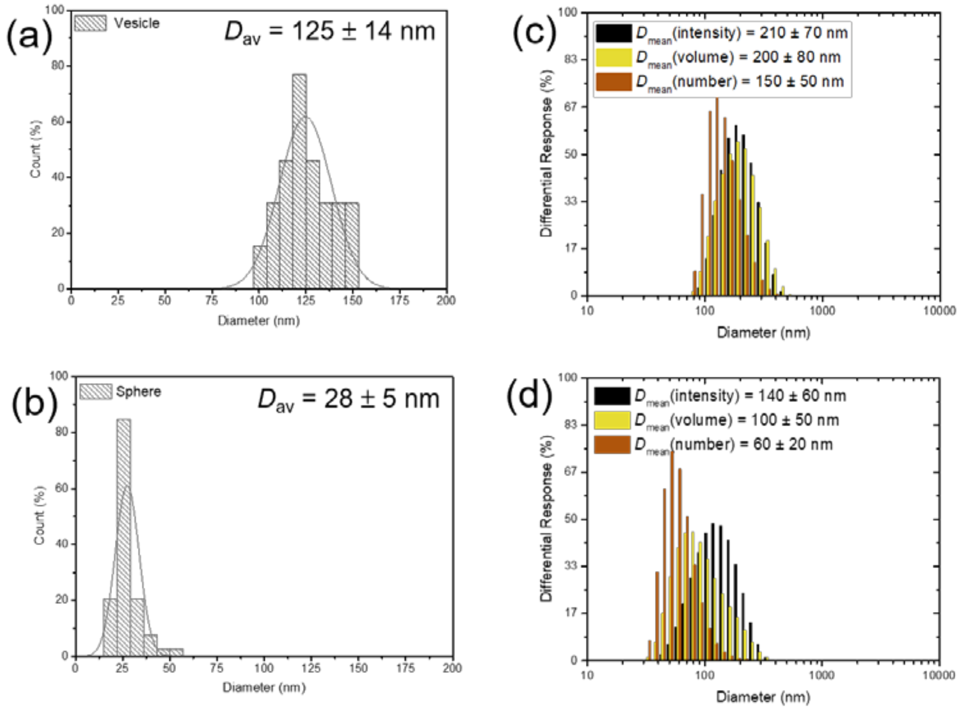

Figure III-12 Histograms of the diameters of nanoassemblies obtained from coil-brush block polymers **A**, P(NB-COOH)$_{54}$-*b*-P(NB-*g*-PGC$_{33}$)$_5$, and **I,** P(NB-COOH)$_{143}$-*b*-P(NB-*g*-PGC$_{33}$)$_2$, as determined by TEM analysis (a, b) and DLS characterization (c, d) respectively.

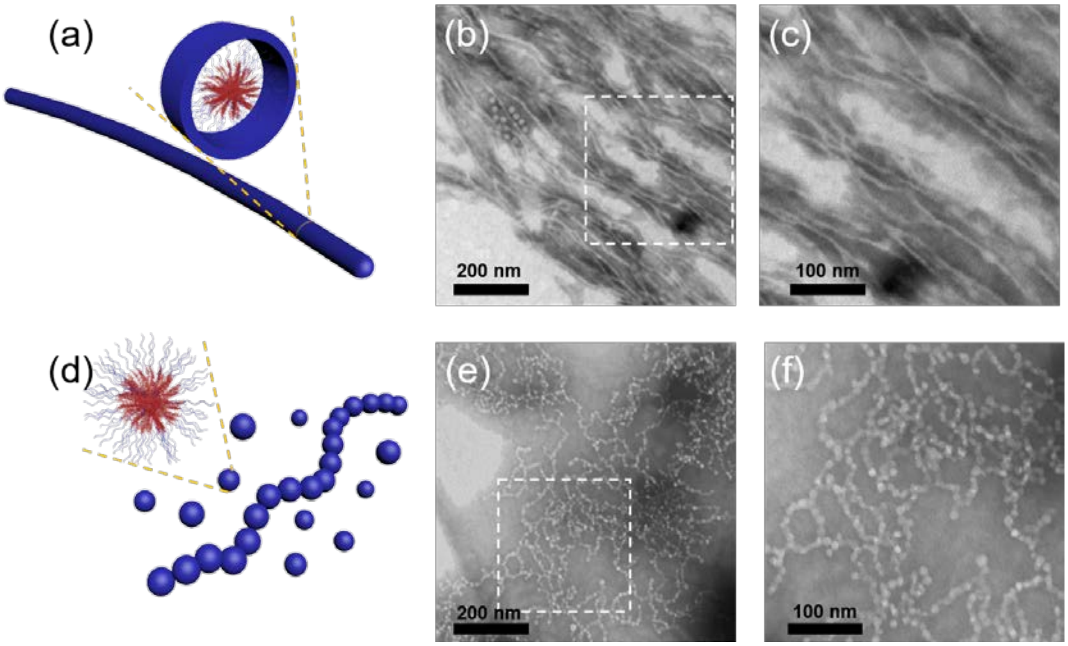

Figure III-13 TEM analysis of assemblies obtained from coil-brush block polymers **E** (b), (c), and **F** (e), (f). TEM samples were negatively stained by 1 wt% phosphotungstic acid aqueous solution (20 μL). Schematic illustrations of elongated cylindrical nanostructures (a) and pearl necklace-like nanostructures (d) composed of coil-brushes.

by TEM (**Figure IIII-13e**, **IIII-13f**) and AFM (**Figure III-16**) for coil-brush **F**, P(NB-COOH)$_{114}$-*b*-P(NB-*g*-PGC$_{17}$)$_7$, having the same polymeric side chain length and slightly higher A/G ratio than coil-brush **E**; thus, the pearl necklace-like nanostructures can be considered as an intermediate between spherical and long cylindrical micelles, which warrants further investigation on the self-assembly mechanisms. For instance, TEM imaging of **F** after three days showed both pearl necklace and cylindrical nanoassemblies and, qualitatively, the pearl necklace-like nanostructures were observed to evolve to cylindrical morphology over longer time periods (**Figure III-17**). The three-dimensional structural information for their higher-order supramolecular assembly was confirmed by tomographic TEM studies, as illustrated in a series of still and video images (**Figure III-18**). When the coil segment was extended further, for example, A/G ratio increasing to 2.04 for coil-brush **K**, P(NB-COOH)$_{139}$-*b*-P(NB-*g*-PGC$_{17}$)$_4$, TEM revealed spherical nanostructures.

Based on the above assembly of a library of coil-brush polymers with a range of side chain polymer lengths and A/G ratios, we proposed a roughly sectionalized phase diagram

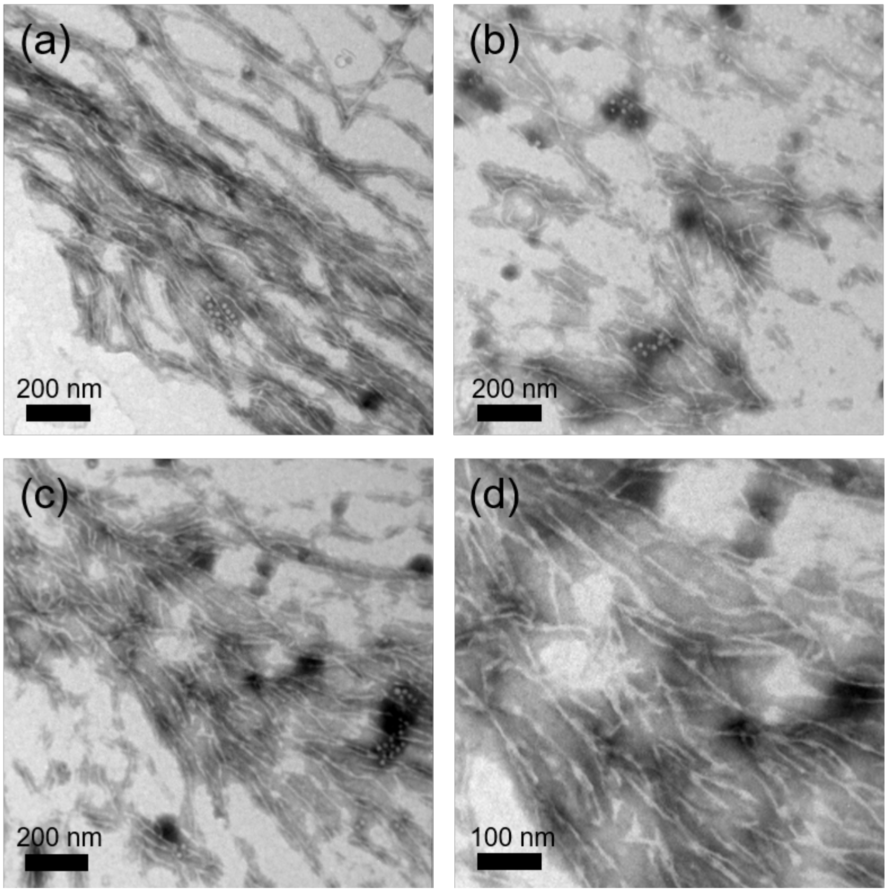

Figure III-14 Additional TEM analysis of assemblies obtained from coil-brush block polymer **E**, P(NB-COOH$_{29}$)-*b*-P(NB-*g*-PGC$_{17}$)$_3$. TEM samples were negatively stained by 1 wt% phosphotungstic acid aqueous solution (20 µL).

(**Figure III-19**). Variation of the side chain length and hydrophilic-hydrophobic ratio dictated the morphology of the nano-objects formed by asymmetric coil-brushes upon aqueous assembly.

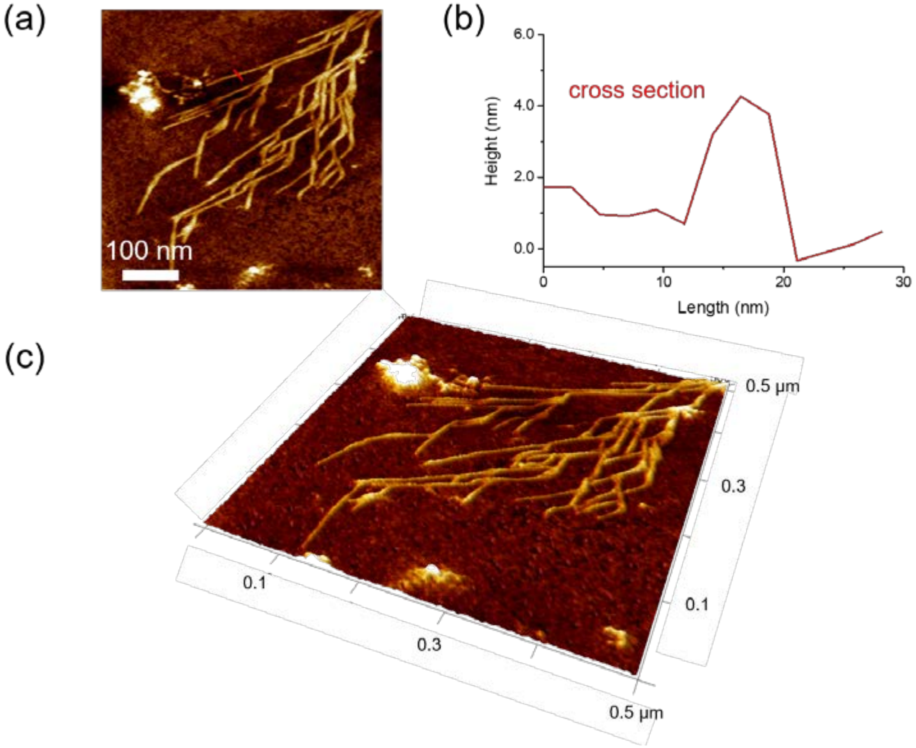

Figure III-15 AFM micrographs (a), height profile (b), 3D image (c) of nanoassemblies obtained from coil-brush block polymers **E**, P(NB-COOH$_{29}$)-*b*-P(NB-*g*-PGC$_{17}$)$_3$. For AFM characterization, the sample solution was drop cast onto the freshly cleaved mica and then dried in air. The height profiles were measured along the red line shown on the micrographs.

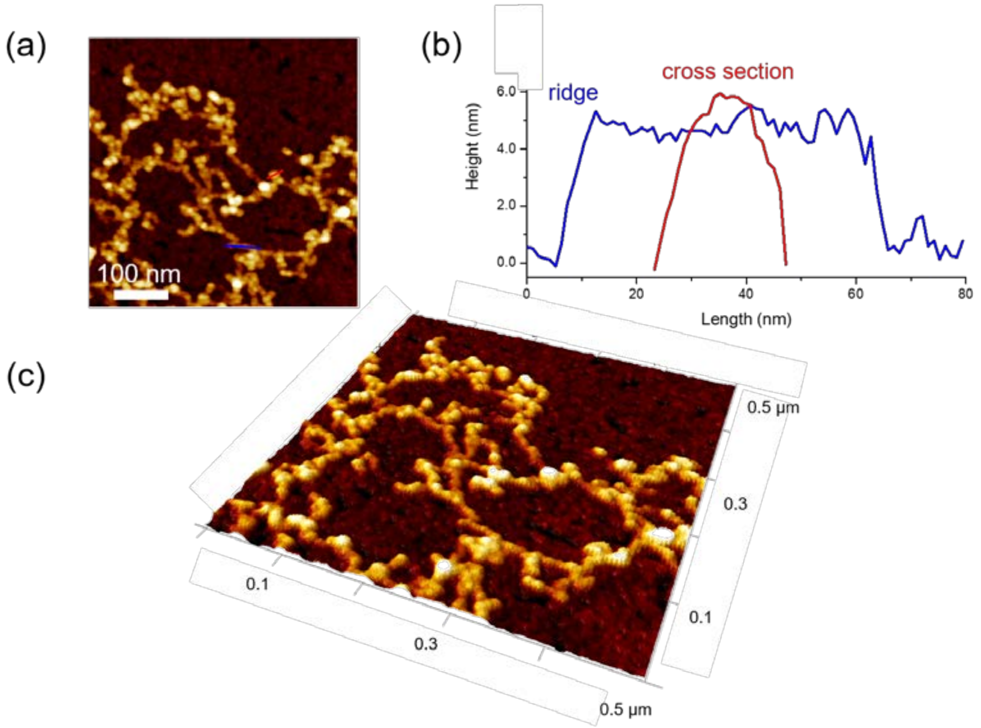

Figure III-16 AFM micrographs (a), height profile (b), 3D image (c) of nanoassemblies obtained from coil-brush block polymers **F**, P(NB-COOH)$_{114}$-*b*-P(NB-*g*-PGC$_{17}$)$_{7}$, analyzed after 3 days. For AFM characterization, the sample solution was drop cast onto the freshly cleaved mica and then dried in air. The height profiles were measured along the colored lines shown on the micrographs.

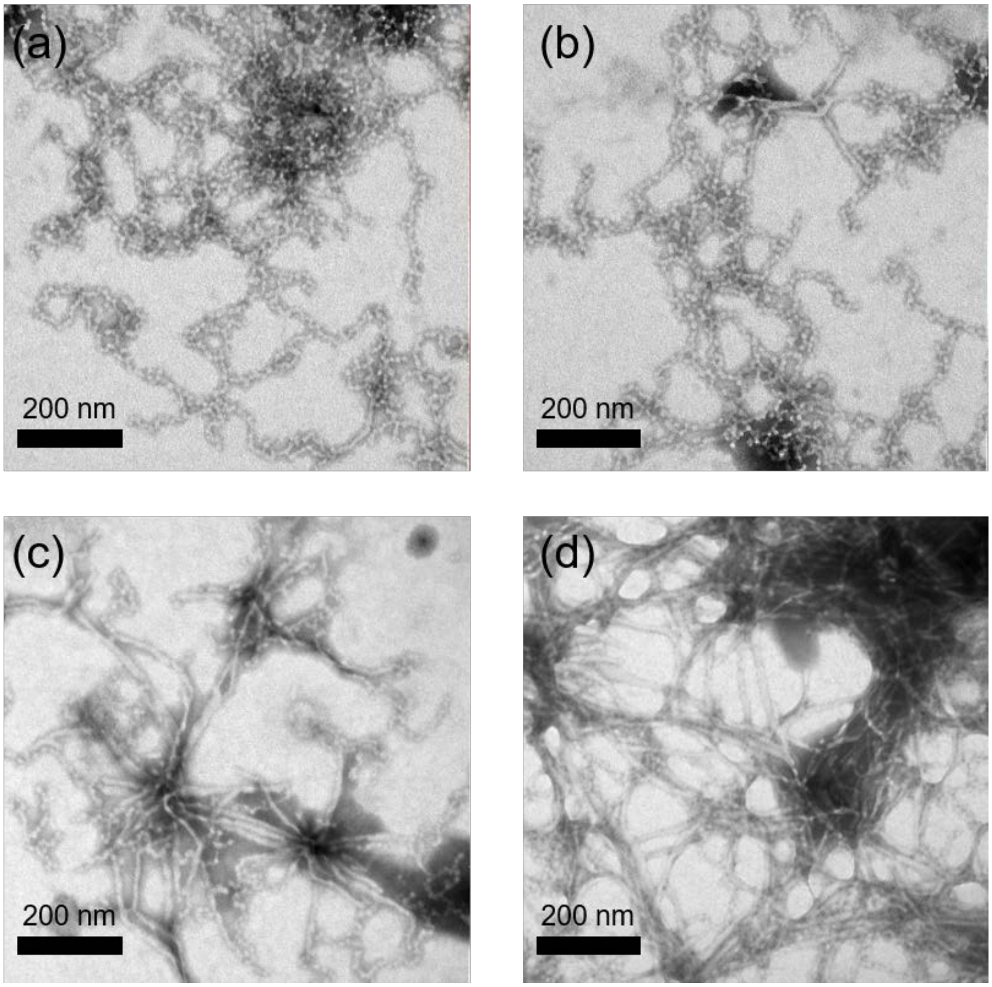

Figure III-17 Additional TEM analysis of assemblies obtained from coil-brush block polymers **F**, P(NB-COOH)$_{114}$-*b*-P(NB-*g*-PGC$_{17}$)$_7$: (a-c) different regions of a TEM grid for a sample analyzed after 3 days; (d) a TEM image collected for the same sample allowed to incubate for 5 days. TEM samples were negatively stained by 1 wt% phosphotungstic acid aqueous solution (20 µL).

(a)

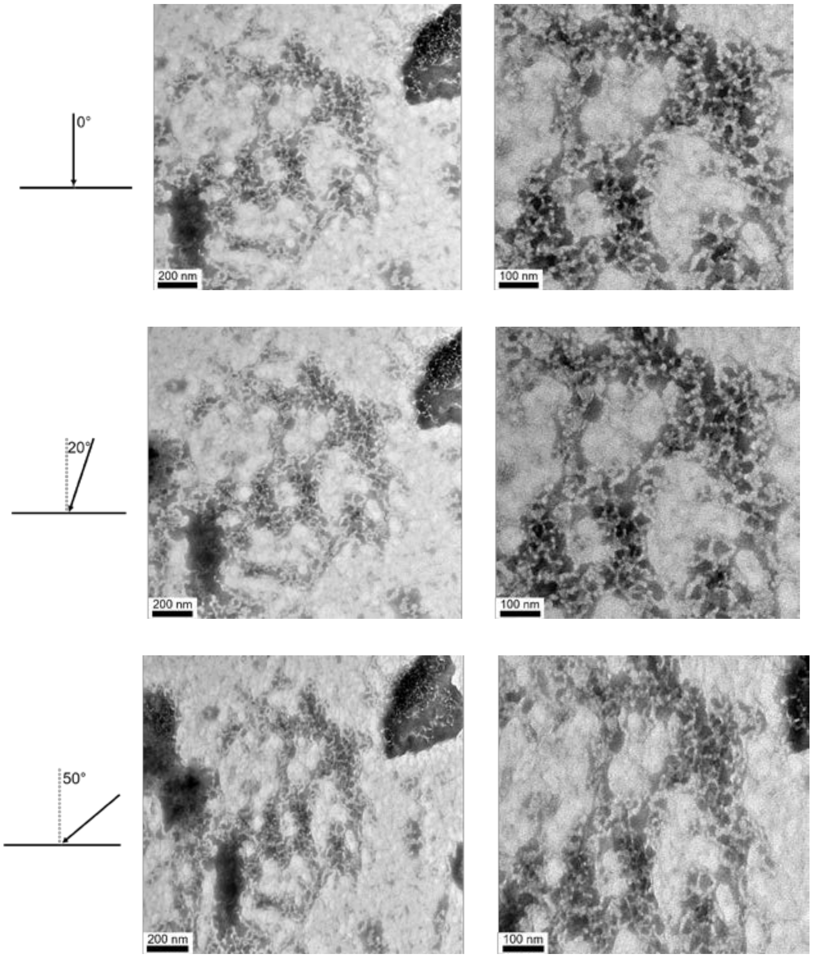

(b)

Pearl Necklace-like Nanostructure-Tomographic Video.avi

Figure III-18 Characterization of nanoassemblies obtained from coil-brush block polymers **F**, P(NB-COOH)$_{114}$-*b*-P(NB-*g*-PGC$_{17}$)$_7$ by tomographic TEM (a) still images taken at 0°, 20°, and 50°; (b) x-y tilt series of images consolidated as a quicktime video. TEM samples were negatively stained by 1 wt% phosphotungstic acid aqueous solution (20 µL).

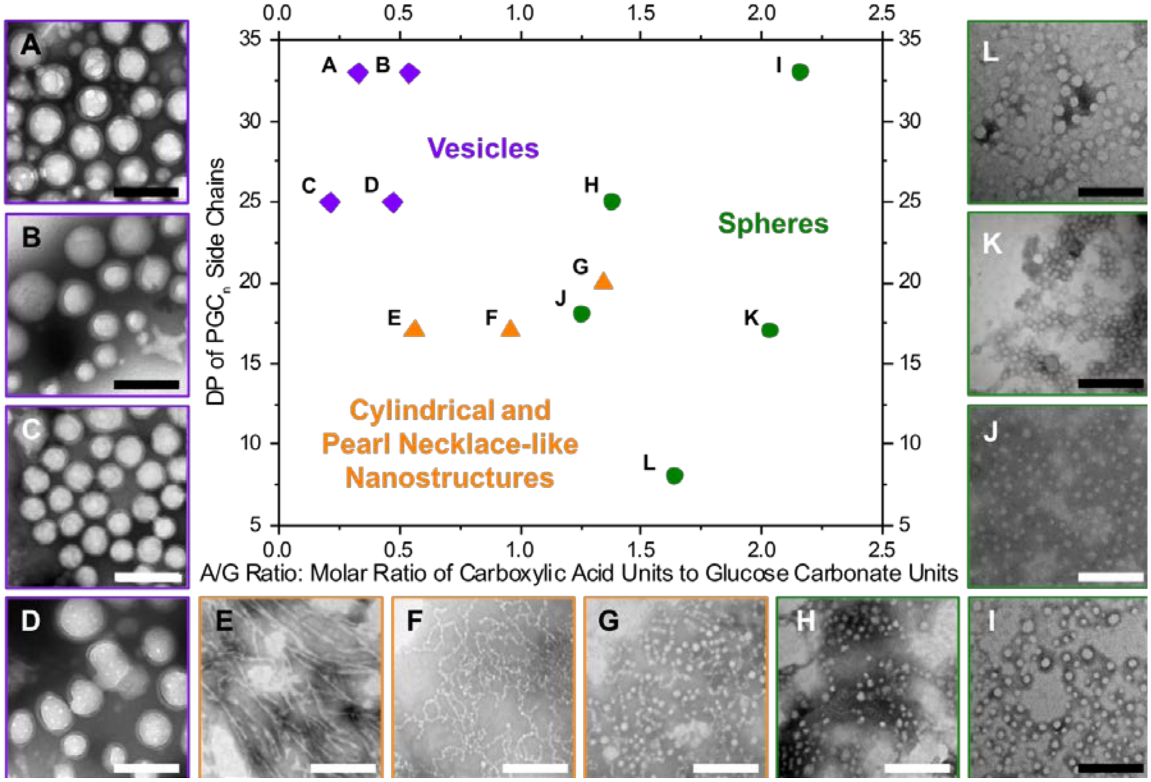

Figure III-19 Phase diagram constructed for coil-brush block polymers **A**-**L**. As the side chain length and hydrophobic-hydrophilic ratio were systematically varied, the resulting morphologies included long cylinders (orange), vesicles (purple), and spheres (green). TEM samples were negatively stained by 1 wt% phosphotungstic acid aqueous solution (20 μL). Scale bars represent 200 nm.

Simulations Using a Coarse-grained Model of the Coil-brush Block Polymers. To complement the experiments and provide understanding of the molecular packing within the assemblies, we conducted simulations using an intermediate resolution coarse-grained (CG) model of the coil-brush block polymers; the details of this CG model are described in the methods section. In **Figure III-20**, we present the phase diagram and representative snapshots of the assembled states seen in simulations as the side chain length and the A/G ratio (ratio of solvophilic/solvophobic degree of polymerization) were varied.

There is qualitative agreement between experiments (**Figure III-19**) and simulations (**Figure III-20**) in how the assembled state and the core-corona interfacial curvature changed with side chain length and A/G ratio. The spherical micelles, which have the highest curvature of all the morphologies, were observed in both simulations and experiments for the assembled states of coil-brush block polymers **H**, **I**, **J**, **K** and **L** with high A/G ratios. At fixed side chain length, decreasing the A/G ratio (*e.g.*, 1.26 **J** to 0.56

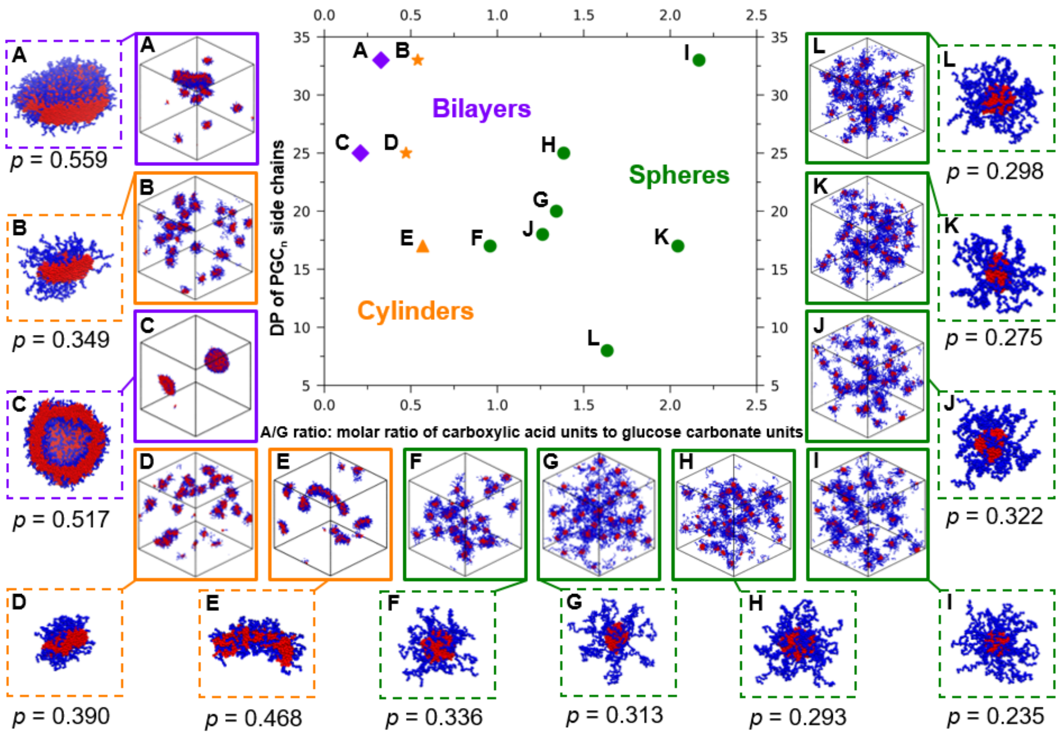

Figure III-20 Phase diagram of assembled states from CG simulations of coil-brush polymers (**A**-**L**) conducted at 1 mg/mL polymer concentration. The assembled states including cylinders (orange triangles), disc-like structures (orange stars), bilayers (purple diamonds), and spheres (green spheres) are shown as a function of the side chain length and hydrophobic-hydrophilic ratio. In addition to representative assembled states (boxes with solid borders) one representative assembled micelle for each state is also shown (boxes with dashed borders) at different scales for visual clarity. The calculated packing parameter (p) for each assembled micelle is also indicated below the relevant micelle shape.

E) decreased the interfacial curvature and the morphologies transition from spherical shapes (in both experiments and simulations) to cylindrical shapes. At approximately the same A/G ratio, increasing the side chain length (*e.g.*, DP_n = 17 in **E** to 33 in **A**) decreased the interfacial curvature, as the morphology transitioned from cylindrical nanostructures to vesicles (in experiments)/bilayers (in simulation). The bilayers and cylinders in the simulations are analogous to the larger scale vesicles and longer cylindrical micelles in experiments, respectively. The chains in the vesicles are expected to arrange in a bilayer manner, and similarly elongated cylindrical nanostructures are the larger scale version of cylinders (See **Figure III-27**).

To connect the changing interfacial curvature with known trends for polymer chain packing parameter, *p*, we calculated *p* of the chains in the assembled state (as described in Simulation Analyses). The *p* obtained for each of the assembly structures is shown in **Figure III-20** and agrees well with known trends of *p* and the observed micelle shapes[145] (See **Figure III-27**). For example, in simulations at a fixed A/G ratio of ~0.3, we see that by decreasing the side chain length, the morphology transitioned from bilayers (see micelle snapshot in **A** with DP_n = 33) to vesicles (see micelle snapshot in **C** with DP_n = 25) in **Figure III-19** The corresponding change in *p* follows the expected trend of Israelachvili and coworkers.[145]

There are some *quantitative* differences between the experimental and computational phase diagrams (**Figures III-19** and **III-20**). In experiments, at an A/G ratio of ~0.5 with increasing side chain length, the morphology changed from cylindrical micelles to vesicles (DP_n = 17 **E** to 33 **B** in **Figure III-19**). In simulations, for the same variation, the morphology changed from cylindrical micelles to disc-like micelles (*DP*$_n$ = 17 **E** to 33 **B** in **Figure III-20**). Thus, the qualitative trend of changing interfacial curvature with the A/G ratio and side chain length is the same in both simulation and experiments, however, the phase boundaries in the phase diagrams do not match quantitatively between simulations and experiments. These phase boundaries can be adjusted through the CG model definition, and we have selected the model that gives the best qualitative match in phase diagram with experiments, while maintaining reasonable computational speed, to further elucidate the chain packing and the conformations that the chains adopt within these micellar structures.

The Effect of Assembly on the Simulated Chain Conformations. In **Figure III-21a**, the conformational changes in the side chains of the coil-brush block polymers **J**, **E**, **C** and **A** upon micellization are shown through shifts in the distribution of the side chain squared end-to-end distances, R_{EE}^2. The emergence of bimodal features in the distribution of R_{EE}^2 upon assembly (at poorer solvent conditions / higher solvophobicity, ε_{BB}, indicated in **Figure III-26**) suggests a population of conformations with $R_{EE}^2 < 2\sigma^2$ and another population at the higher R_{EE}^2. Side chains with $R_{EE}^2 < 2\sigma^2$ loop back to the backbone in a collapsed conformation, visualized in black in **Figure III-21b**. These collapsed chains were well dispersed throughout the system, occurring in most of the micelles (**Figure III-21c**), regardless of the morphology. We conjecture that, in general, the coil-brush block polymers with brush hydrophobic cores yielded frustrated packing in the micelle cores, and this led to some of the side chains sacrificing their conformational entropy to reduce the packing frustration, leading to an increased volume (*i.e.*, possibility to explore conformations, and thus higher conformational entropy) for the remaining side chains within the micelle cores.

The discussion accompanying supplementary **Figure III-26** provides additional details of chain conformation calculations/visualization.

Comparison Between Experimental and Simulation Spherical Micelle Sizes. The core radius of the spherical micelles shows quantitative agreement between experiments (measured from TEM images) and simulation (measured using two different metrics: the radius of gyration and the concentration profile) in **Figure III-28**. Although, we see that

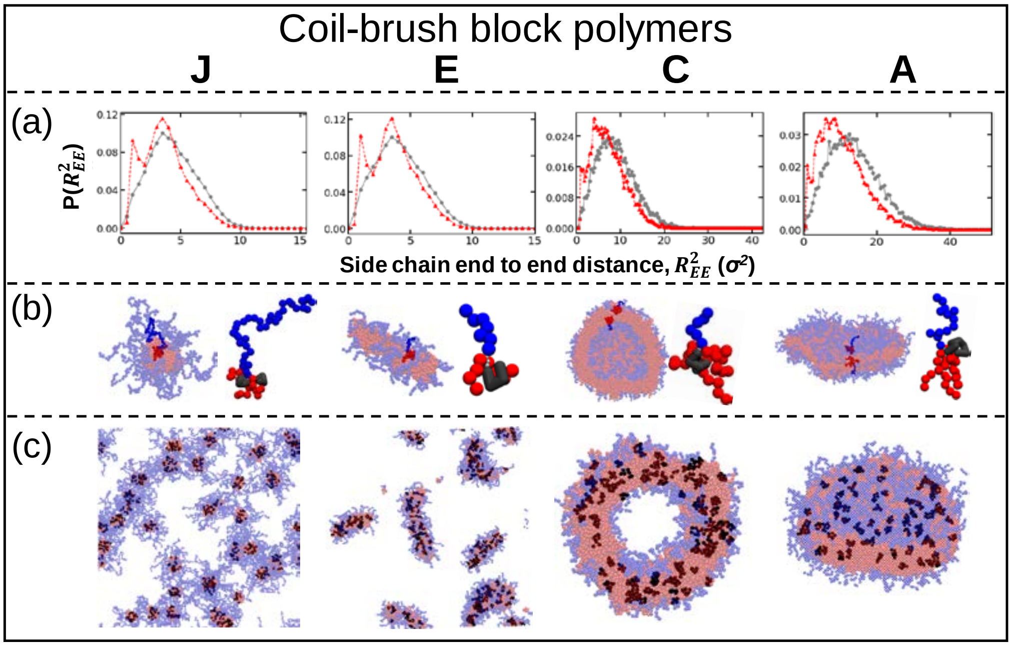

Figure III-21 Side chain conformations for coil-brush polymers **J**, **E**, **C** and **A**. (a) The probability distributions of the side chain squared end to end distances, $\mathbf{P(R_{EE}^2)}$ *versus* $\boldsymbol{R_{EE}^2}$, at low solvophobicity (in disordered state, gray) and at high solvophobicity (upon assembly, red). (b) Representative assembled micelle structure and chain conformations; in black are side chains that loop back to the backbone with an $\boldsymbol{R_{EE}^2} < 2\sigma^2$. (c) Representative snapshots of the assembled state with all side chains that adopt $\boldsymbol{R_{EE}^2} < 2\sigma^2$ shown in black. All images are at different scales for visual clarity.

the total micelle sizes are larger in the simulation than in the experiments, which is expected to be due to complications with identification of the outer surface of the micelles by the TEM imaging using negative staining. The technique of measuring the center-to-center distances for particle pairs that appeared to be in contact may have generated artificially low radii values, originating from particle-particle interactions and compression of the shell during the drying process.

Intermediate Resolution Coarse-grained Model of P(NB-COOH)-b-P(NB-g-PGC) Coil-brush Block Polymers. To mimic the length and time scales of the experimental assembly in the simulations of the amphiphilic PGC-based coil-brush block polymers, we developed a coarse-grained (CG) model that captures the key physical characteristics of the coil-brush block polymer architecture and yet prevents the simulations from being as computationally-expensive as atomistic resolution simulations. In our intermediate resolution CG model (*i.e.*, somewhere between atomistic model and coarser bead spring[148-149] models), we used three types of CG beads (B, A and N) varying in sizes and interaction. Each solvophobic side chain (B) bead (shown in red in **Figure III-22**) represented 4 glucose-derived polycarbonate repeat units in the solvophobic side chains; the B diameter was set to 1.00d in simulations units where 1d corresponds to around 2.8 nm based on the approximate length between four repeat units. One norbornene backbone (N) bead (shown in gray in **Figure III-22**) with diameter 0.25d represented one repeat unit in the polynorbornene backbone. One solvophilic (A) bead (in blue) represented either 1, 2, or 4 repeat units in the solvophilic linear polymer coil; these different bead sizes for the solvophilic beads each representing a different number of (solvophilic) norbornene-based repeat units were tested to determine which more accurately captured the excluded volume of the solvophilic coil upon assembly. The A beads representing 1, 2, or 4 repeat units had diameters of 0.25*d*, 0.50*d* or 1.00*d*, respectively. The best choice of solvophilic bead representation is based on how closely the resulting assembled morphologies from simulations match those from experiments. Our results (**Figure III-22**) show that the best representation is one where each solvophilic A bead of diameter of 1.00*d* represented 4 repeat units in the solvophilic linear polymer coil.

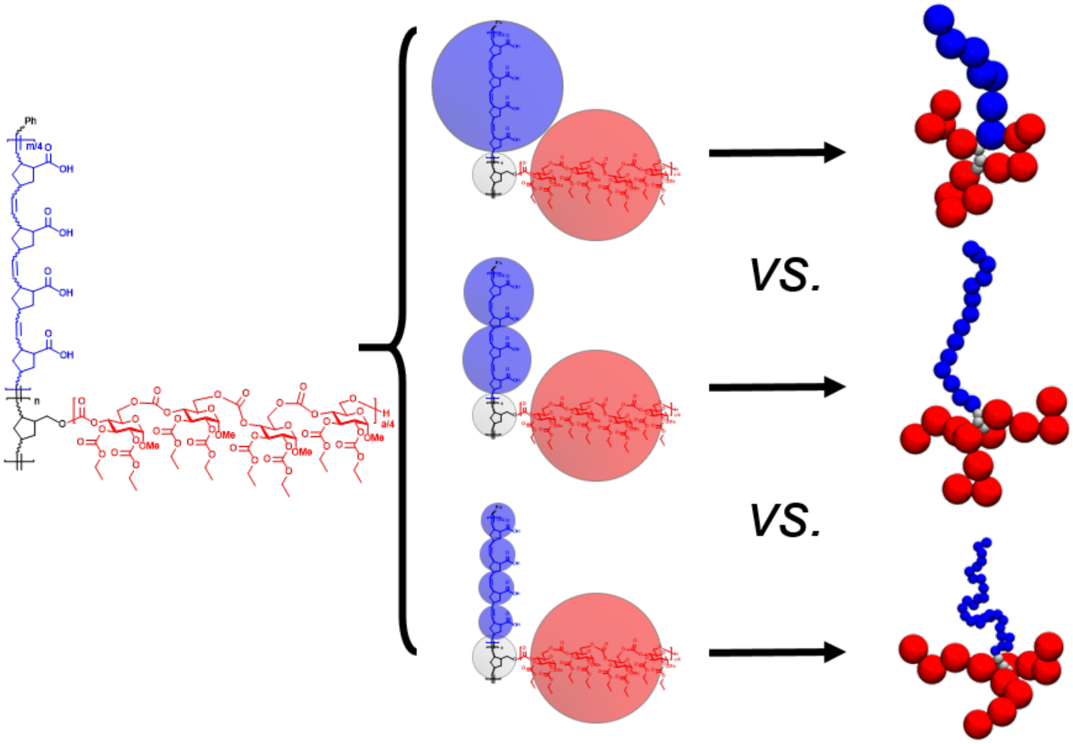

Figure III-22 Coarse grained representations of the coil-brush chemistry (left) for coil-brush block polymer **E** P(NB-COOH)$_{29}$-*b*-P(NB-*g*-PGC$_{17}$)$_3$ (right column). Different coarse-grained representations (center column) and representative simulation snapshots (right column) of the (solvophilic) linear norbornene-based coils with every 4 repeat units represented by a bead of 1.00*d* diameter (top row), every 2 repeat units represented by a bead of 0.50*d* diameter (middle row) and every repeat unit represented by a bead of 0.25*d* diameter (bottom row).

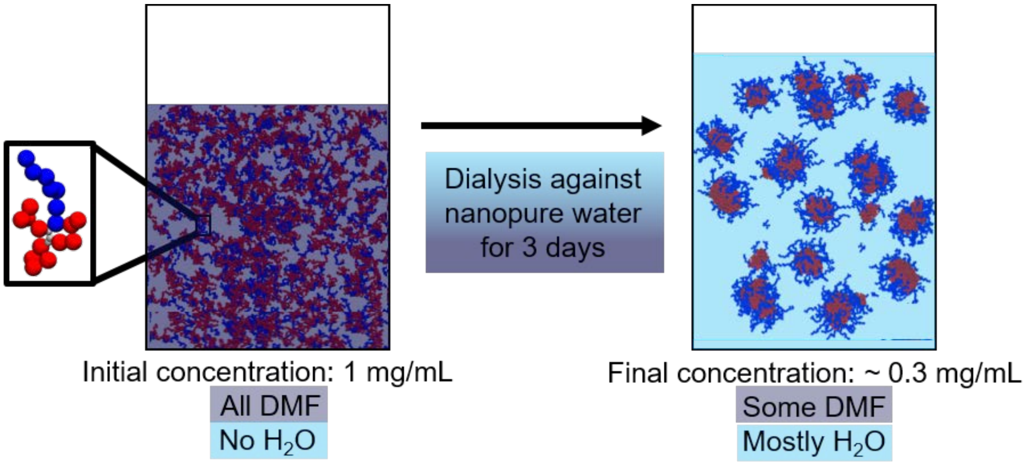

Figure III-23 Schematic illustration of the assembly procedure. To mimic the gradual solvent exchange in experiments, in the simulations the solvent quality was altered by changing ε_{BB}. The simulation volume was kept constant and the effect of the changing volume on the assembly was tested with separate simulations at the initial and final concentrations (1.0 and 0.3 mg/mL, respectively).

Irrespective of CG bead type, each bead was bonded to its neighboring bead *via* a harmonic bond potential, with a force constant of 50 ε/d^2 where ε is the energy in reduced Lennard-Jones (LJ)[150] units and had an equilibrium bond distance equal to the arithmetic mean of the bonded bead sizes. The A-A, A-B, A-N, and B-N non-bonded interactions were modeled using purely repulsive Weeks-Chandler-Andersen,[151] WCA, potential, where the values for the WCA parameters ε and σ, were 1 (in reduced energy units) and the arithmetic mean of the interacting bead sizes, respectively. The cut-off distance was equal to $2^{1/6}$ multiplied by the σ of the interacting pair. The effect of solvent quality or *solvophobicity*, ε_{BB}, was captured implicitly *via* the strength of attraction between the solvophobic side chain B beads, modeled using a LJ interaction potential that was shifted to have a value of 0 at the cut-off distance 2.5*d*. The values of the ε and σ parameters were set to ε_{BB} and 1σ. Increasing the value of ε_{BB} indicates a worsening solvent for the solvophobic block.

Simulation of the Self-assembly of P(NB-COOH)-b-P(NB-g-PGC). The self-assembly of the coil-brush block polymers in implicit solvent was studied using MD simulations in the NVT ensemble using the Nose-Hoover thermostat with the LAMMPS package.[152] In the simulations, the solvophobicity, ε_{BB}, of the system (the degree to which the solvent is poor for the solvophobic components) was gradually increased, driving the assembly of the polymers, similar to a gradual change in solvent composition through dialysis in experiments in **Figure III-23**. As the exact solvophobicity corresponding to each solution

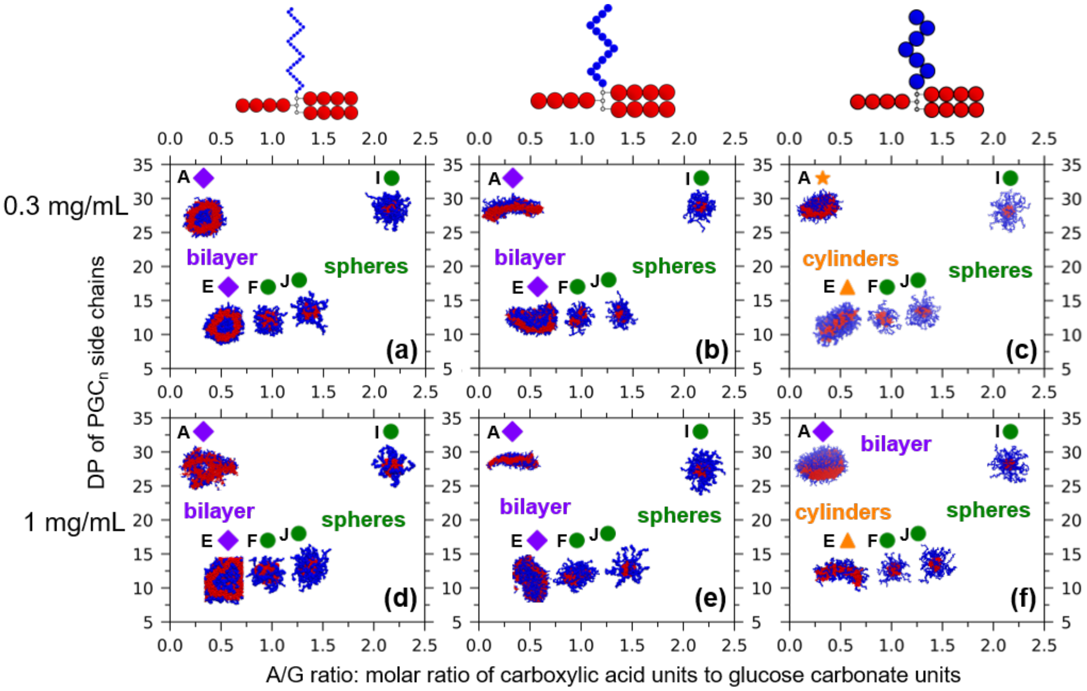

Figure III-24 Phase diagram of assembled morphologies from simulations of coil-brush block polymers **A**, **E**, **F**, **J**, **I** at 0.3 mg/mL (a, b and c) and 1.0 mg/mL (d, e and f). The models used to produce the phase diagrams are shown at the top of the column.

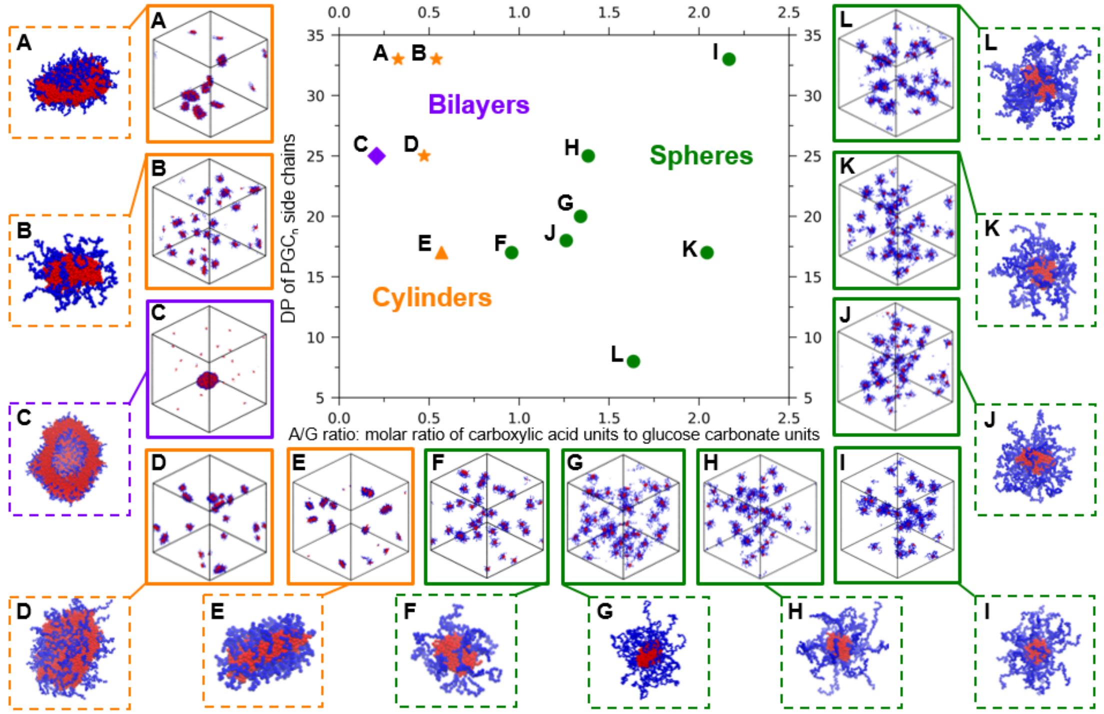

Figure III-25 Phase diagram of assembled morphologies from simulations of coil-brush block polymers (**A-L**) at a polymer concentration of 0.3 mg/mL. The assembled states including cylinders (orange triangles), disc-like structures (orange stars), bilayers (purple diamonds), and spheres (green spheres) are shown as a function of the side chain length and hydrophobic-hydrophilic ratio. In addition to representative assembled states (boxes with solid borders), one representative assembled micelle for each state is also shown (boxes with dashed borders) at different scales for visual clarity.

concentration throughout the dialysis process was unknown, we gradually changed the solvent quality at both the initial 1.0 mg/mL and the final 0.3 mg/mL polymer concentrations (see **Figures III-22**, **III-23**). Since the micelles assembled at a concentration between the initial 1.0 mg/mL and the final 0.3 mg/mL in experiments during dialysis, we expected that the experimental assembled results would lie in between the assembled results between these two simulation regimes.

We created an initial configuration by randomly placing 600 chains in a cubic simulation box larger than the final size we sampled at, to prevent overlap between the chains. We simulated that large simulation box at a temperature of $T^* = 1.0$ and at low solvophobicity ($\varepsilon_{BB} = 0.055$) to relax the configuration away from that initial placement. During this stage, we linearly reduced each of the simulation box sides until we achieved the simulation box size that had the desired polymer concentration; this was done over 3,000,000 timesteps where each timestep corresponded to $\Delta t = 0.005$ (in reduced time units). After an additional 3,000,000 timesteps, to equilibrate at $\varepsilon_{BB} = 0.055$ in the simulation box at the desired polymer concentration, the solvophobicity was increased in a step-wise fashion, $\varepsilon_{BB,\mathrm{i}} = \varepsilon_{BB,\mathrm{i-1}} + \Delta\varepsilon_{BB}$ with $\Delta\varepsilon_{BB} = 0.009$. At each value of ε_{BB} we run the simulation for 3,000,000 and 10,000,000 timesteps for 1.0 and 0.3 mg/mL, respectively. The choice of $\Delta\varepsilon_{BB}$ and the number of timesteps at each of ε_{BB} was chosen after extensive testing that ensured the same equilibrium assembly morphologies were sampled and kinetically trapped morphologies were avoided. These tests included doubling the number of timesteps at each solvophobicity as well as running replicate simulations for a select few coil-brush polymers to ensure that these tests resulted in the same morphologies irrespective of the number of timesteps or the system size. Overall, the simulation procedure was similar to previously reported protocols.[153-154]

Simulation Analyses. We visualized the simulations using VMD.[155] Additionally, we investigated the changes in the chain conformations during assembly and calculated the packing parameter of the chains within the simulation as a function of solvophobicity, ε_{BB}.

Packing Parameter. We calculated the packing parameter, *p*, as

$$p = \frac{V}{l_c A} \qquad (1)$$

after visually confirming that the clusters had assembled and did not change with increasing solvophobicity. The volume of the solvophobic block per chain, *V*, the length of the solvophobic block per chain within the micelle core, l_c, and the interfacial area between the micelle core and corona per chain, *A*, were calculated after assembly, depicted in **Figure III-27**.

The volume of the solvophobic block per chain, *V*, was calculated as

$$V = \frac{\sum_1^{N_B} V_B + \sum_1^{N_N} V_N}{0.64} \qquad (2)$$

where the first summation term is the total volume of the solvophobic B side chain beads, V_B is the volume of a B bead and N_B is the number of B beads per chain, and the second summation term is the total volume backbone N beads per chain, V_N is the volume of an N bead and N_N is the number of N beads per chain, and 0.64 is the random sphere packing. By dividing the total volume by 0.64, we can account for void volume during random sphere packing of the spherical beads within the micelle core.

The value of l_c calculated as

$$l_c = \left(\frac{1}{N_{chains}\,(N_B+N_N-1)} \sum_i^{N_{chains}} \sum_j^{(N_B+N_N-1)} \left(\boldsymbol{r}_{int,i} - \boldsymbol{r}_{ij}\right)^2\right)^{0.5} \qquad (3)$$

is the average distance from the N backbone CG bead sitting at the interface to the rest of the beads in the backbone and solvophobic block of chain i averaged over all chains, N_{chains}, in the simulation. For chain i, $r_{int,i}$ is the position vector of the its N bead sitting at the interface and r_{ij} is the position vector of another j bead that is B or another N bead; N_B and N_N are the number of B and N beads, respectively in every chain. Determination of l_c for the coil-brush polymers is not straightforward, as the solvophobic bottlebrush block is unlike a generic linear chain that stretches into the micelle core. Depending on how we chose to determine l_c, the values of the packing parameter changed, but the qualitative trends between the packing parameters with changing side chain length and A/G ratio remained the same (data not shown).

The solvent accessible surface area (SASA)[156-157] was calculated with a solvent probe radius of 1σ; the probe size was chosen to exclude voids in the micelle core as we desire to quantify the core-corona interface to determine the packing parameter. The green beads in **Figure III-27** visualize the SASA. The interfacial area per chain

$$A = \frac{SASA}{N_{chains}} \tag{4}$$

was then determined by dividing the calculated area, SASA, by the number of chains, N_{chains}, in the simulation.

Chain Conformations. We calculated the average and the probability distribution of the squared radius of gyration, R_g^2 and the squared end to end distance, R_{EE}^2, of each side chain, the solvophilic block comprised of the A beads, $R_{g,A}^2$, and solvophobic block comprised of the B and N beads, $R_{g,B}^2$, of each chain similarly as previously reported.[158]

Additional discussion of chain conformations during assembly.

We investigated the conformations of the polymer chains during assembly, and the results are shown in **Figure III-26**. As the results follow a similar qualitative trend for all coil-brush block polymers, we show the results for one of each of the assembled morphologies as an example, where a representative micelle and chain are shown in **Figure III-26**a. We determined the chain conformations as a function of solvophobicity (**Figure III-26**b) by considering the average and the probability distribution of the squared radius of gyration, R_g^2, at low and high solvophobicity, as indicated in (**Figure III-26**b), for each solvophobic (**Figure III-26**c) and solvophilic block (**Figure III-26**d), and for each chain (**Figure III-26**e).

The average $R_{g,B}^2$ of the solvophobic block decreases with increasing solvophobicity, (**Figure III-26**b), as chains collapse with worsening solvent quality. This is also reflected in the $R_{g,B}^2$ probability distribution (**Figure III-26**c). The average and the probability distribution of $R_{g,A}^2$ of the solvophilic block do not change significantly with increasing solvophobicity (**Figure III-26**b and d).

The average R_g^2 of the chains decreases with increasing solvophobicity as chains collapse with worsening solvent quality, until clusters start to form (**Figure III-26**b). After clusters start to form, the average R_g^2 of the chains increases with increasing solvophobicity (**Figure III-26**b), as the solvophobic and solvophilic block separate to the micelle core and corona, respectively.

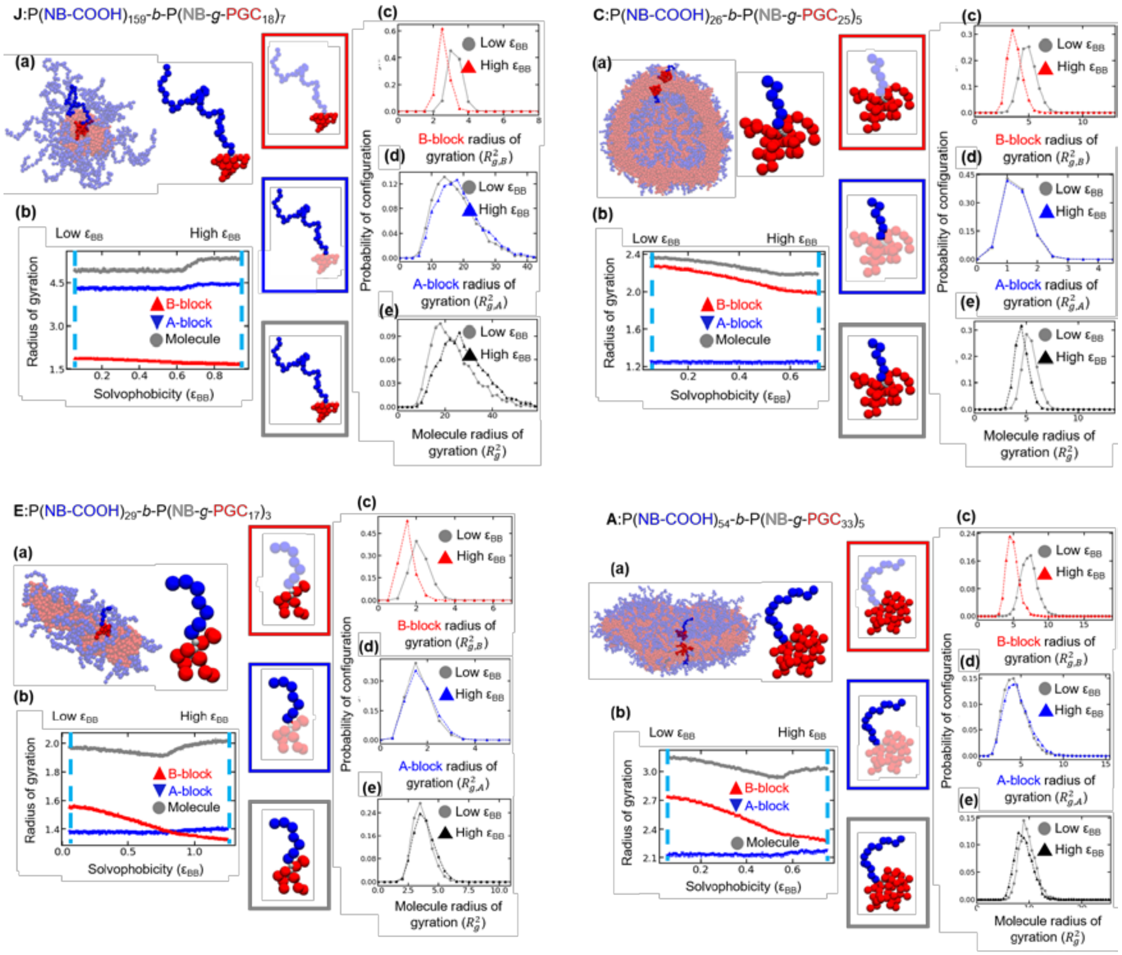

Figure III-26 Chain conformations during micellization for coil-brush block polymers **J**, **E**, **C** and **A**. Part (a) shows representative simulation snapshots of a micelle and a chain within the micelle core. The radius of gyration as a function of solvophobicity for different components of the polymer chain (b) as shown in (c), (d) and (e). The radius of gyration probability distribution at low and high solvophobicity for the whole molecule (c), the solvophobic B-block (d), and the solvophilic A-block (e). The low and high solvophobicity values, ε_{BB}, are indicated with dashed lines on (b).

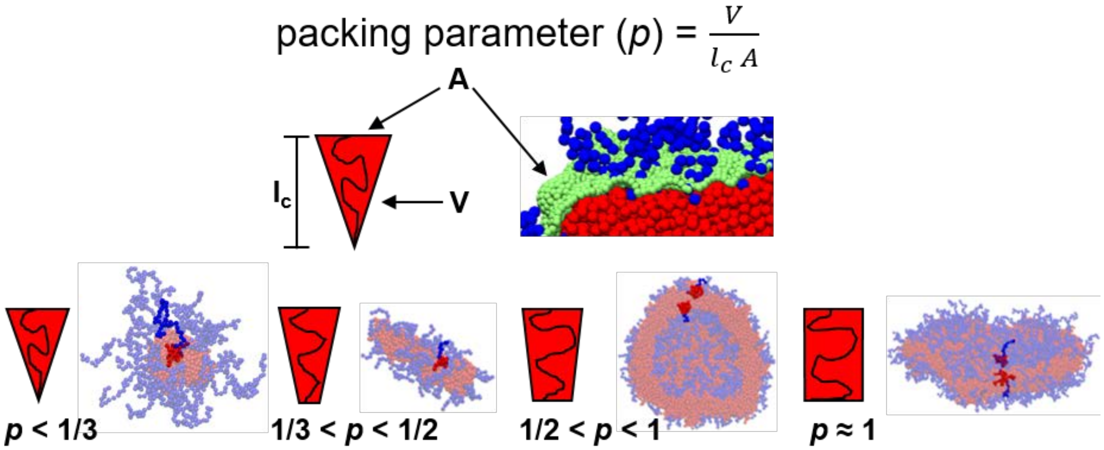

Figure III-27 Schematic of the chain packing parameter (p) calculation. Values of $p <$ 1/3 indicate spherical morphologies, values between 1/3 and 1/2 indicate cylindrical morphologies, values between 1/2 and 1 indicate vesicle morphologies and values around 1 indicate bilayers.

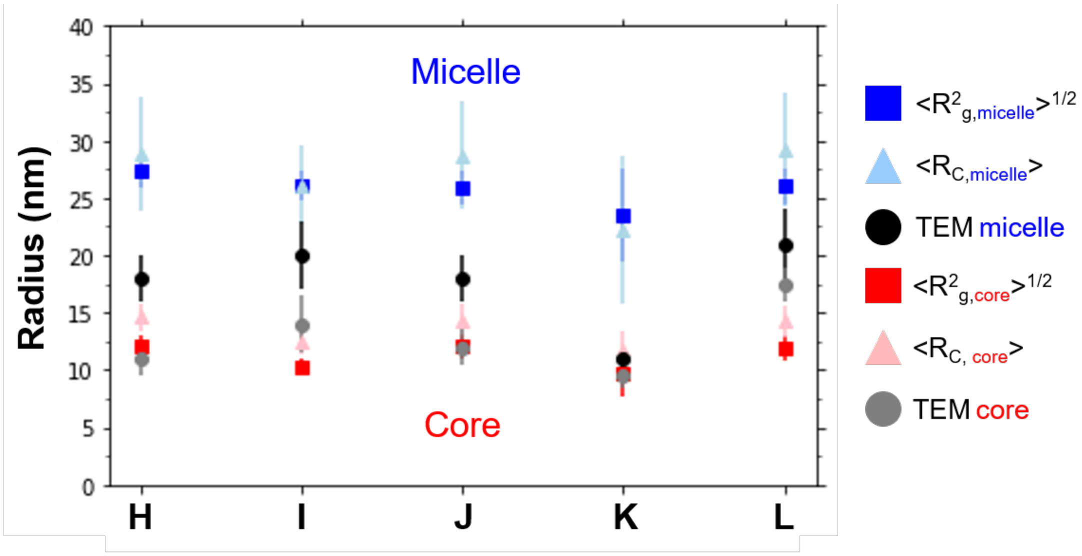

Figure III-28 Comparison of micelle sizes and core sizes for spherical micelle forming coil-brush polymers **H**, **I**, **J**, **K** and **L**. From simulations, the ensemble average radius of gyration, $<R^2_g>^{1/2}$, and the ensemble average value of the distance from the micelle center of mass at which the concentration profile of the micelle from its center of mass reaches 50% of its maximum value, $<R_C>$, were calculated for the core and total micelle dimensions. The micelle core and total dimensions were also determined from TEM images (larger images coinciding with the zoomed in regions shown in **Figure III-19** for **H**, **I**, **J**, **K**, and **L**), by measuring the core and entire micelle radii for *ca*. 50 particles. Due to complications with visualization of the outer micelle surface, the entire micelle radii were estimated by measuring the center-to-center distances for contact pairs of micelles and dividing by 2. Error bars indicate the standard deviation. The standard deviations from the simulation results were determined from multiple uncorrelated configurations from one trial.

Conclusions

With the rapidly growing interest in the manufacture of materials that are translated from fundamental development to practical implementation to address societal needs, there is an increasing opportunity to harness the powerful advances that can come from integrating experimental techniques with computational tools. In this work, a series of well-defined P(NB-COOH)-*b*-P(NB-*g*-PGC) coil-brush block polymers that possess interesting features, including broad compositional, structural and morphological design space, were prepared through a combination of ROP and ROMP, and their self-assembly behaviors in aqueous solutions were explored by experiments and simulations. We probed the impact of altering the side chain length and overall hydrophilic-hydrophobic ratio on the nanoscopic morphology. In general, the less hydrophilic coil-brush block polymers tended to form vesicles or cylinders, while the more hydrophilic polymers yielded spherical structures and pearl necklace-like nanostructures; pearl necklace-like nanostructures were observed at intermediate hydrophilic-hydrophobic compositions. The length of the hydrophobic side chains was found to determine the interfacial curvature between the hydrophilic corona and hydrophobic core and, thereby, impact morphology. The qualitative agreement between experiments and simulations validates the coarse-grained model and enables the predictive design of nanostructures from this glucose-based coil-brush polymer platform while providing a fundamental understanding of interactions within solution assembly of complex polymer building blocks. Our findings expand the library of brush polymer assemblies and probe the architecture-morphology relationships of these glucose-based coil-brush block polymers through experimental and simulation tools.

Moreover, the degradable sugar-based coil-brush component as well as facile assembly in aqueous environment make these coil-brush block polymers promising nanomaterials for biological and environmental impact. For instance, toward biomedical applications, diverse morphologies are known to impart various benefits: conventional spherical micelles are able to load hydrophobic cargos, whereas vesicles have the potential to carry both hydrophobic and hydrophilic cargos at the same time, and have even been employed as nanoreactors by accommodating hydrophobic cargo in the membrane and hydrophilic cargo in the interior.[79, 159] Cylindrical nanostructures are of great interest owing to their large contact area with target tissues, longer *in vivo* circulation times, preference for altered cell-internalization pathways compared to spheres, *etc*.[160-162] With respect to the architecture of coil-brush building blocks, hydrophilic coronas consisting of linear-shaped segments are known to provide highly-tunable pathways for cargo release, for instance, crosslinking or grafting additional side chains to hinder release of encapsulated compounds.[163] Additionally, PGC-based cores with the potential to break down into natural by-products are anticipated to enable controlled cargo release upon degradation. With respect to limiting the long-term environmental impact of polymer materials, increasing attention is being directed toward the construction of functional polymers from natural building blocks and also to building in mechanisms for degradation or recycling.[147, 164-169] These poly(glucose carbonate)s offer advantages in both directions. Further studies involve the utilization of these combined experiments and simulations to produce increasingly complex nanostructures, derived from natural building blocks to afford functional properties and allow for mechanisms for their subsequent breakdown.

CHAPTER IV

SUGAR-BASED DEGRADABLE MAGNETIC TRIBLOCK POLYMER NANOCOMPOSITES FOR ENVIRONMENTAL REMEDIATION[*]

Introduction

Oil spills endanger marine and human life, threaten drinking water and natural resources, damage parts of the food chain, and pose serious hazards to the aquatic environment, public health, and global economy.**[170-172]** Several methods (*e.g.* physical, mechanical, chemical and biological, *etc.*) are available to contain oil spills in addition to natural processes, such as evaporation, oxidation, and biodegradation.**[173-174]** Common physical methods for oil spill clean-up include pressure washing, raking and bulldozing, which are time-consuming and require extensive equipment and personnel resources. Mechanical containment methods, such as booms and skimmers, are used at an earlier stage to block the spread of oil, limit its area, and remove it from the water.**[173]** Chemical and biological treatment of oil, such as dispersing agents and gelling agents, can be used followed by, or even in place of, mechanical methods, especially in areas where untreated oil may reach shorelines and in sensitive habitats where clean-up processes become difficult and environmentally damaging.**[175-176]** Among these methods and techniques, synthetic sorbents and dispersing agents are more attractive and commonly used to remove final

---

[*] Reprinted (adapted) with permission from "Degradable Sugar-based Magnetic Hybrid Nanoparticles for Recovery of Crude Oil from Aqueous Environments" by Dong, M.; Song, Y.; Wang, H.; Su, L.; Shen, Y.; Tran, D. K.; Letteri, R. A.; Flores, J. A.; Lin, Y-N.; Li, J.; Wooley, K. L., *Polym. Chem.* **2020**, Advanced Article, DOI: 10.1039/D0PY00029A. https://pubs.rsc.org/no/content/articlelanding/2020/py/d0py00029a/unauth#!divAbstract. Copyright 2020 Royal Society of Chemistry (RSC).

traces of oil or to remove oil in areas where mechanical containment and clean-up are difficult.[177-178]

With the growing awareness of the persistence of plastics in the environment, including microplastics, there has been a rising concern about the materials used in the commercially-available sorbents and dispersing agents on the market.[179-182] Synthetic polymer-based sorbents or dispersants have been reported to generate micro- and nano-plastics in aquatic environments.[183-185] Transfer of these persistent micro- and nano-plastics across the food chain can cause serious and far-reaching threat to the global health of wildlife and human populations.[182-183, 186] Moreover, agents that are deployed are often not recovered, which may not only contribute to the contamination but also represent a wasteful approach to material resources, as occurs for a traditional linear, take-make-dispose economy.[187] One of the key strategies to solve these problems is the development of materials that can undergo passive degradation if discarded and active recycling or upcycling processes if recovered. By such processes, it is possible to evolve towards a more sustainable circular economic system, in which plastics can be make-use-reuse with reduction of waste.[188-190]

In addition to long-term environmental problems, previous synthetic polymeric sorbents present several challenges that include difficulty in retrieval from water, proper storage after use, and thorough cleaning for reuse, even though they demonstrate outstanding performance in pollutant absorption.[191-194] To address these limitations, magnetic actuation has been introduced to facilitate the collection of deployed conventional oil sorbents.[195-199] For instance, Gui and co-workers reported the fabrication of magnetic carbon nanotube sponges that have porous structures consisting of interconnected carbon nanotubes with Fe encapsulation.[197] Pan and co-workers designed a series of ultralow-density Fe_2O_3/C, Co/C, and Ni/C magnetic poly(acrylic acid) (PAA)-grafted polyurethane foams modified by reaction with methyltrichlorosilane for oil-water separation.[200] Dispersed, discrete nanoparticles are expected to exhibit optimal small molecule uptake performance because they have high surface areas for contact, while maintaining adequate core volume for packaging of hydrophobic hydrocarbon components of crude oil or other pollutants. It is a common observation that oil, when spilled on water, tends to spread on the water surface in the form of a thin continuous layer of less than 5 μm thickness within a short time.[201-202] Therefore, a large surface area-to-volume ratio is likely to be beneficial to increase the efficiency and lower the amount of absorbent required, which may also reduce the energy and economic costs.[50-51, 203] Moreover, the existence of submarine seepage during offshore drilling operations can cause long-term damage to the environment.[204] Amphiphilic dispersant-based materials have potential to recover both surface and sub-surface oil populations.[205-206] Assimilating all of these factors, a degradable magnetically-active dispersant-based material is considered to be highly desirable for the design of oil recovery materials, which may have limited adverse environmental impact, themselves, while also contributing to a plastic circular economy.

Previously, well-defined magnetic shell cross-linked knedel-like nanoparticles (MSCKs) were constructed through the co-assembly and intramicellar cross-linking of amphiphilic block copolymers poly(acrylic acid)$_{20}$-*block*-polystyrene$_{280}$ (PAA$_{20}$-*b*-PS$_{280}$) and oleic acid-stabilized MIONs.[51] The co-assembly process provided a large number of magnetic nanoparticles incorporated non-covalently within each polymeric micelle formed by PAA_{20}-*b*-PS_{280}, which was further cross-linked to increase stability and loading capability by creating a sturdy vessel that could undergo reversible expansion and contraction. However, the polymeric scaffold in this former design was comprised of two non-degradable components, PAA and PS, which have been widely used in cosmetics, personal care, and plastics industries for years and present an emerging threat in marine and aquatic ecosystems as microplastics.[207] To tackle these environmental concerns, our group has developed glucose-derived polycarbonates containing labile carbonate linkages to construct functional materials that are able to degrade into natural products, including glucose, carbon dioxide, and ethanol.[66, 208-209] In this current work, we have taken advantage of several interesting recent developments toward chemistries[210-212] that allow for the preparation of degradable polycarbonates containing diverse functional groups and derived from natural products,[59, 62, 213-220] to design a sustainable polycarbonate system that incorporates glucose, ethanol and dopamine as natural building blocks to assemble hybrid inorganic-organic nanoparticles that achieve effective oil uptake performance due to steric bulk and hydrophobicity, with magnetic recovery, and hydrolytic degradability.

Materials and Methods

Materials

The bicyclic glucose-based carbonate monomer, methyl-2,3-*O*-ethyloxycarbonyl-4,6-*O*-carbonyl-α-D-glucopyranoside (GC) and Grubbs' G3 catalyst were synthesized according to previously-published procedures.[75,76] α-Methoxy-ω-amino polyethylene glycol (PEG) was purchased from Rapp Polymere GmbH (Tübingen, Germany). 3-(3-

Dimethylaminopropyl)-1-ethyl-carbodiimide hydrochloride (EDC hydrochloride) and 1,5,7-triazabicyclo[4.4.0]dec-5-ene (TBD) were purchased from TCI America (Portland, OR), and TBD was degassed and stored in a glovebox under Ar atmosphere. Other chemicals and reagents were purchased from Sigma-Aldrich, Co. (St. Louis, MO) and were used as received, unless otherwise noted. Tetrahydrofuran (THF), dichloromethane (DCM), and *N*,*N*-dimethylformamide (DMF) were purified by passage through a solvent purification system (J. C. Meyer Solvent Systems, Inc., Laguna Beach, CA). Nanopure water (18 MΩ·cm) was obtained from a Milli-Q water filtration system (Millipore Corp, USA). Dialysis membrane tubing with a molar mass cut off (MWCO) of 6-8 kDa was purchased from Spectrum Laboratories, Inc. (Rancho Dominguez, CA) and soaked for 5 min in nanopure water at room temperature (rt) before use. Column chromatography was performed on a CombiFlash Rf4x (Teledyne ISCO) with RediSep Rf columns (Teledyne ISCO).

Instrumentation

^{1}H NMR and ^{13}C NMR spectra were recorded on Varian Inova 500 spectrometer (Varian, Inc., Palo Alto, CA) interfaced to a UNIX computer using the VnmrJ software. Chemical shifts for ^{1}H NMR and ^{13}C NMR signals were referenced to the solvent resonance frequencies. Fourier transform infrared (FT-IR) spectra were recorded on an IR Prestige 21 system, equipped with a diamond attenuated total reflection (ATR) lens (Shimadzu Corp., Japan), and analyzed using IRsolution v. 1.40 software.

Size exclusion chromatography (SEC) eluting with tetrahydrofuran (THF) was performed on a Waters Chromatography, Inc. (Milford, MA) system equipped with an isocratic pump (model 1515), a differential refractometer (model 2414), and column set comprised of a PLgel 5 μm guard column (50 × 7.5 mm), a PLgel 5 μm Mixed C column (300 × 7.5 mm, Agilent Technologies) and two Styragel® columns (500 Å and 104 Å, 300 × 7.5 mm, Waters Chromatography, Inc.). The system was operated at 40 °C with a flow rate of 1 mL/min. Data were analyzed using Breeze software from Waters Chromatography, Inc. (Milford, MA). Molar masses were determined relative to polystyrene standards (580–3,250,000 Da) purchased from Polymer Laboratories, Inc. (Amherst, MA). Polymer solutions were prepared at a concentration of *ca.* 3 mg/mL with 0.05 vol% toluene as the flow rate marker; an injection volume of 200 μL was used.

Glass transition temperatures (T_g) were measured by differential scanning calorimetry (DSC) on a Mettler-Toledo DSC3/700/1190 (Mettler-Toledo, Inc., Columbus, OH) under a nitrogen gas atmosphere. Measurements were performed with a heating and cooling rate of 10 °C/min, and three heating and cooling cycles were conducted. Measurements were analyzed using Mettler-Toledo STAR^e v. 15.00a software. The T_g was taken as the midpoint of the inflection tangent of the third heating scan.

Thermogravimetric analysis (TGA) was performed under N_2 atmosphere using a Mettler-Toledo TGA2/1100/464, with a heating rate of 10 °C/min. Data were analyzed using Mettler-Toledo STAR^e v. 15.00a software.

Electrospray ionization mass spectrometry (ESI-MS) was performed using an Applied Biosystems PE SCIEX QSTAR instrument.

Magnetic measurements were carried out on a Quantum Design MPMS XL superconducting quantum interference device (SQUID) magnetometer at room temperature.

Transmission electron microscopy (TEM) images were collected on a JEOL 1200EX operated at 100 kV, and micrographs were recorded using an SIA-15C CCD camera. Samples for TEM were prepared as follows: 20 μL of polymer solution in nanopure water (1 mg/mL) was deposited onto a carbon-coated copper grid, and after 1 min, excess solution was quickly wicked away by a piece of filter paper. The samples were then negatively stained with a 1 wt% phosphotungstic acid (PTA) aqueous solution (20 µL). After 30 s, excess staining solution was quickly wicked away by a piece of filter paper and the samples were left to dry under ambient conditions prior to imaging. High-resolution scanning transmission electron microscopy (STEM) and elemental mapping were conducted on a FEI TECNAI G2 F20 ST FE-TEM – MATERIALS coupled with Oxford instruments energy-dispersive X-ray spectroscopy (EDS) detector, operating at a voltage of 200 kV with a Gatan 2k x 2k CCD camera.

Atomic force microscopy (AFM) was performed using the Multimode 8 system (Bruker) in PeakForce™ tapping mode using a ScanAsyst-Air Silicon Nitride probe ($k = 0.4$ N/m, $f_0 = 70$ kHz, Bruker). AFM samples were prepared by depositing nanocomposites (1 mg/mL in nanopure water, 20 µL) on freshly cleaved mica surface. The mica surface was allowed to dry in air. AFM images were analyzed using Nanoscope Analysis software from Bruker.

Dynamic light scattering (DLS) measurements were conducted using a Zetasizer Nano ZS instrument (Malvern Panalytical Ltd., Malvern, United Kingdom) equipped with a laser diode operating at 633 nm. Scattered light was detected at 175° and analyzed using a log correlator for a 0.5 mL of sample in a disposable cell (capacity = 0.9 mL). The photomultiplier aperture and attenuator were adjusted automatically. The particle size distribution and distribution averages were calculated using particle size distribution analysis routines in Zetasizer 7.13 software. The number of accumulations and measurement duration were adjusted automatically. All measurements were repeated 3 times. The average diameter of the particles is reported as the intensity-, volume- and number-average particle diameter from three measurements.

Experimental Procedures

Synthesis of Fe_3O_4 nanoparticles via thermal decomposition method.[221] A flame-dried, 50 mL three-neck flask equipped with a magnetic stir bar and condenser was charged with iron(III) acetylacetonate, $Fe(acac)_3$ (1 equiv, 720.1 mg, 2.039 mmol), oleic acid (3 equiv, 2.3 g, 6.0 mmol) and oleyl amine (3 equiv, 2.0 g, 6.0 mmol). After the addition of solvent benzyl ether (20 mL) and 1,2-hexadecanediol (5 equiv, 2.6 g, 10 mmol), the reaction mixture was deoxygenated by a flow of nitrogen for 30 min. The reaction temperature was then increased to 140 °C for 1 h. After an hour, the reaction temperature was taken to 200 °C for one hour and then, under a blanket of nitrogen, heated to reflux at 250 - 300 °C for an additional hour. Once the reaction mixture was cooled to room temperature, it was transferred into a centrifuge tube and centrifugation (8000 rpm, 10 min) was applied to remove any undispersed residue. The black-colored mixture was then precipitated with

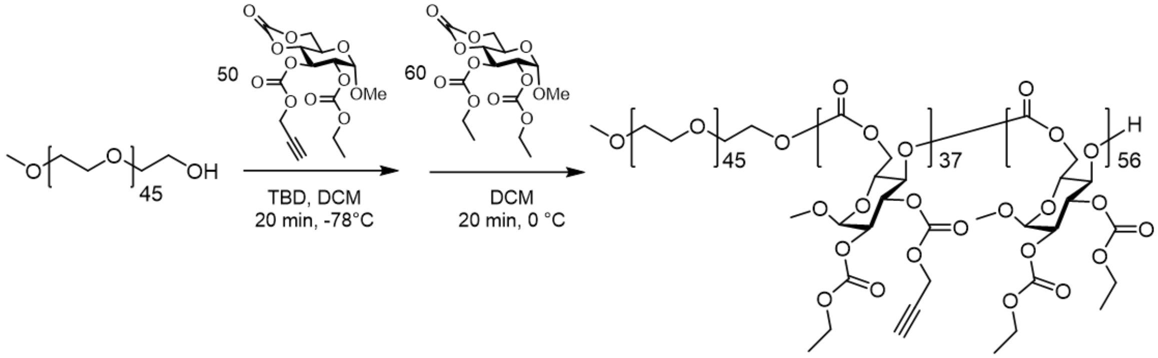

Scheme IV-1 Synthetic procedure for **1**.

ethanol, centrifuged (8000 rpm, 10 min) to remove the solvent, and resuspended into THF for more than three cycles, until the supernatant became clear (Yield: 81%).

*Synthesis of PEG-b-PGC(EPC)-b-PGC(EC) triblock terpolymers 1 (***Scheme IV-1***).* Monomers GC(EPC) and GC(EC) were dried under vacuum over P_2O_5 for 3 days before transferring to a glovebox for storage under an inert atmosphere. All stock solutions were prepared in the glovebox under Ar atmosphere and the reaction conducted in a fume hood.

To a solution of GC(EPC) (52 equiv., 48.0 mg, 128 μmol) and α-methoxy-ω-hydroxy poly(ethylene glycol)$_{45}$ (1 equiv., 4.9 mg, 2.5 μmol) in anhydrous DCM (3.0 mL), organocatalyst TBD (0.38 mg, 2.7 μmol) in DCM (200 μL) was added under Ar atmosphere at -78 °C. After stirring for 20 min, the DCM solution (500 μL) of GC(EC) (58 equiv., 52.8 mg, 145 μmol) was added and allowed to stir for 20 min at 0 °C, then quenched by addition of acetic acid. The polymer was purified by precipitation from THF into diethyl ether (3×) and dried under vacuum to give a white powder. Yield = 90%. ^{1}H NMR (500 MHz, $CDCl_3$) δ ppm 5.45 – 5.26 (m, C^3H), 5.02 (m, C^1H), 4.95 – 4.79 (m, C^4H), 4.77 – 4.64 (m, C^2H, OCH_2CCH), 4.36 – 4.23 (m, C^6H_2), 4.19 (m, OCH_2CH_3), 4.02

(m, C^5H), 3.64 (s, OCH_2CH_2 in PEG unit), 3.45 – 3.34 (s, OCH_3 in glucose unit), 2.59 (s, OCH_2CCH), 1.35 – 1.24 (m, OCH_2CH_3). ^{13}C NMR (126 MHz, $CDCl_3$) δ ppm 154.08, 154.02, 153.73, 153.62, 153.53, 96.40, 76.18, 74.11, 73.65, 73.39, 72.70, 72.18, 70.52, 66.68, 65.99, 65.69, 64.77, 64.67, 64.58, 55.87, 55.74, 55.60, 46.88, 37.71, 25.58, 20.84, 15.23, 14.08. FT-IR (ATR, cm^{-1}) 3707−3356, 3335−3145, 2889, 1767, 1464, 1450, 1373, 1344, 1238, 1142, 1099, 1016, 993, 961, 869, 841, 781. M_n (NMR) = 36200 g/mol. M_n (SEC) = 30400 g/mol. $Đ$ = 1.08. T_g = 70 °C. TGA in N_2, 172-189 °C, 8% mass loss; 230-275 °C, 50% mass loss; 363−407 °C, 16% mass loss.

*Synthesis of PEG-b-PGC(EPC-MPA)-b-PGC(EC) 2 by post-polymerization modification of 1 with 3-mercaptopropionic acid (**Scheme IV-2**).* Terpolymer **1** (1 equiv., 80.3 mg, 2.21 μmol), 3-mercaptopropionic acid (742 equiv., 174 mg, 143 μL, 1.64 mmol), and 2,2-dimethoxy-2-phenylacetophenone (DMPA) (371 equiv., 210 mg, 0.818 mmol) were dissolved in anhydrous DMF (10 mL), deoxygenated under N_2 for 30 min, and irradiated under UV light (365 nm) for 2 h. The resulting mixture was transferred to dialysis tubing and dialyzed against sodium bicarbonate solution followed by nanopure water for 3 days to remove excess thiol and solvent residue. The solution was lyophilized and further

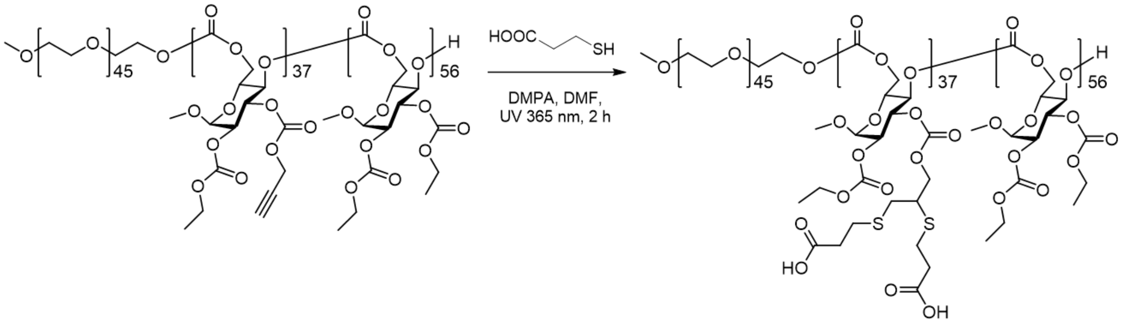

Scheme IV-2 Synthetic procedure for **2**.

purified by precipitation from THF into diethyl ether (3×) to remove excess impurities, then dried under vacuum to give the polymer PEG-*b*-PGC(EPC-MPA)-*b*-PGC(EC) as a white powder. Yield = 92%. ^{1}H NMR (500 MHz, DMSO-d_6) δ ppm 5.12 (m, C^1*H*), 4.99 (m, C^4*H*), 4.95 – 4.71 (m, C^2*H*), 4.44 – 4.22 (m, C^5*H*), 4.13 (m, OCH_2CHS, OCH_2CH_3), 3.99 (m, C^6*H*), 3.50 (s, OCH_2CH_2 in PEG unit), 3.31 (s, OCH_3), 2.72 (m, SCH_2CH_2COOH), 2.49 (m, OCH_2CHCH_2S), 1.19 (m, OCH_2CH_3). ^{13}C NMR (126 MHz, DMSO-d_6) δ ppm 173.40, 154.30, 153.96, 76.14, 70.23, 67.47, 64.90, 62.63, 60.73, 55.36, 49.04, 35.26, 34.92, 31.14, 25.57, 14.33. FT-IR (ATR, cm^{-1}) 3696−3206, 3055−2733, 1753, 1466, 1450, 1395, 1371, 1342, 1244, 1144, 1101, 1032, 1018, 964, 872, 781. T_g = 5 °C, 60 °C. TGA in N_2, 298−329 °C, 38% mass loss; 379-402 °C, 24% mass loss.

*Synthesis of PEG-b-PGC[(EPC-MPA)-co-(EPC-DOPA)]-b-PGC(EC) 3 by conjugation of dopamine hydrochloride with 2 (**Scheme IV-3**).* PEG-*b*-PGC(EPC-MPA)-*b*-PGC(EC) (1 equiv., 15 mg, 0.34 µmol), dopamine hydrochloride (0.7 equiv. relative to carboxylic acid groups, 3.5 mg, 19 µmol), and EDC hydrochloride (2 equiv. relative to carboxylic acid groups, 9.5 mg, 50 µmol) were dissolved in 10 mL dry DMF and added with triethyl amine (TEA, 1 equiv. relative to carboxylic acid groups, 2.55 mg, 3.51 µL, 25 µmol)

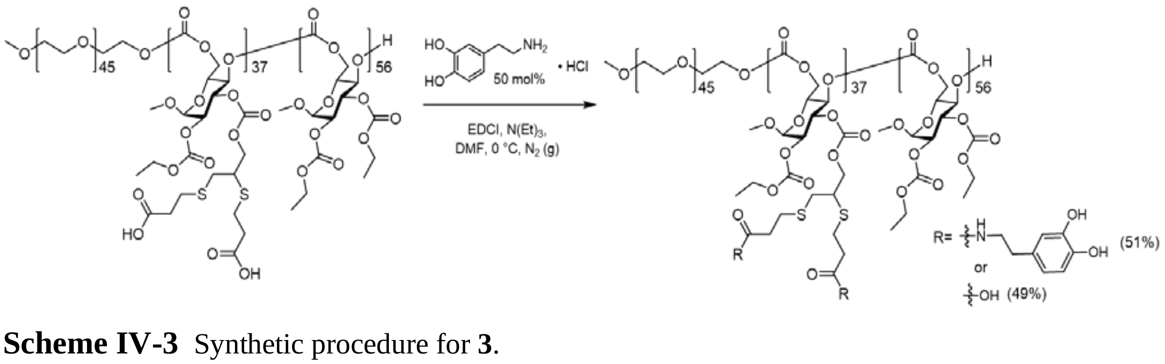

Scheme IV-3 Synthetic procedure for **3**.

solution afterwards in the glovebox under Ar atmosphere. The mixture was transferred to the fume hood and allowed to react at 0 °C for 20 min, then slowly turn back to room temperature and react for another 10 h under nitrogen flow and aluminum foil to avoid polymerization of dopamine. The resulting mixture was transferred to a 6 – 8 kDa dialysis tubing and dialyzed against nanopure water to remove solvent residues for 3 days. The solution was lyophilized and further purified by precipitation from THF into diethyl ether (3×) to remove impurities insoluble in water, then dried under vacuum to give the polymer PEG-*b*-PGC[(EPC-MPA)-*co*-(EPC-DOPA)]-*b*-PGC(EC) as a white powder. Yield = 87%. Dopamine conjugation percentage = 51%. ^{1}H NMR (400 MHz, DMSO-d_6) δ ppm 11.42 (s, SCH_2CH_2COOH), 8.95 (m, protons from dopamine diol), 7.94 (m, $CONHCH_2$), 6.94 – 6.01 (m, *Ar*), 5.35 – 4.59 (m, $C^{1}H$, $C^{4}H$, $C^{2}H$), 4.49 – 3.88 (m, $C^{5}H$, OCH_2CHS, OCH_2CH_3, $C^{6}H$), 3.50 (s, OCH_2CH_2 in PEG unit), 1.09 (m, OCH_2CH_3). ^{13}C NMR (126 MHz, $CDCl_3$) δ ppm 195.17, 154.10, 136.85, 134.23, 132.86, 129.99, 128.91, 128.52, 128.13, 126.93, 103.58, 96.33, 73.69, 72.70, 70.55, 64.69, 55.63, 50.05, 28.30, 23.58, 19.32, 14.11. FT-IR (ATR, cm^{-1}) 3688-3186, 3071-2823, 2754-2167, 1929, 1759, 1659, 1620, 1366, 1242, 995, 879, 833, 779, 702. T_g = 93 °C. TGA in N_2, 213−260 °C, 38% mass loss; 393-401 °C, 12% mass loss.

Preparation of nanocomposites 4 by co-assembly of triblock polymer 3 and iron oxide nanoparticles. PEG-*b*-PGC(MPA)-*b*-PGC(EC) was dissolved in DMF (4 mg/mL, 5 mL, 1 vol%), and mixed with 0.2 mg/mL iron oxide nanoparticle solution in THF (5 mL, 1 vol%). The mixture was sonicated for 10 min. Nanopure water (10 mL, 2 vol%) was added into the sonicated mixture dropwise by a syringe pump at 2 mL/h. Additional nanopure water (10 mL, 2 vol%) was added afterwards within 15 min. The resulting solution mixture was transferred to 6 – 8 kDa molecular weight cut-off dialysis tubing immediately and dialyzed against nanopure water for 1 day. The solution was lyophilized and resuspended in nanopure water directly to afford a 1 mg/mL solution.

Representative Procedure for Oil Sequestration Experiments. Weathered crude oil from the Texas−Oklahoma pipeline (light sweet crude oil, density = *ca.* 0.76 g/mL) was added to a 4 mL shell vial containing nanopure water (2 mL). Powdered glucose-based magnetic nanoparticles (2 mg) were added to the oil-contaminated water and allowed to rest with minimal movement. After *ca.* 10 h, the loaded material was attracted by an external magnetic field for *ca.* 10 min, followed by decanting of the contaminated water for oil extraction.

Oil Recovery Experiments. The crude oil trapped within the nanocomposites was extracted with diethyl ether (1 mL) twice. The nanocomposites were vortexed and sonicated for *ca.* 1 min to allow complete recovery of crude oil. The composite materials were recovered using magnet (neodymium magnet, 90 lb pull) and the crude oil-containing organic phase was transferred to a pre-weighed clean vial. After the evaporation of diethyl ether, the mass of the extracted crude oil was recorded. Experiments were conducted in triplicate.

Recyclability Tests. The composite materials with 15 mg initial amount were reused for another two cycles of oil sequestration after the extraction of captured crude oil. For each cycle, 150 µL of crude oil was applied. The recovered composite materials were redeployed into contaminated water (2 mL) and exposed to the external magnetic field followed by the same procedure as previously described. The experiment was repeated for three times, and the loading capacity of the reused materials [sequestered crude oil/nanocomposite (mg/mg)] was recorded.

Degradation Study. Degradation study in organic media: PEG-*b*-PGC[(EPC-MPA)-*co*-(EPC-DOPA)]-*b*-PGC(EC) (5.0 mg) were added in DMSO-d_6 to an NMR tube containing 0.2 mL D_2O, and 6 mg TEA to yield a 5 mg/mL solution. The solution was incubated at 37 °C, and the degradation process was monitored by ^1H NMR spectroscopy. There was no obvious change in NMR spectra over 100 days, 100 μL of the reaction mixture was removed and directly analyzed by ESI-MS.

Hydrolytic degradation study in aqueous media: PEG-*b*-PGC[(EPC-MPA)-*co*-(EPC-DOPA)]-*b*-PGC(EC) (5.0 mg) was added to D_2O in an NMR tube containing NaOD to yield a 5 mg/mL solution (pH = 10). The solution was incubated at 37 °C, and the degradation process was monitored by ^1H NMR spectroscopy. No obvious change in NMR spectra over 60 d, reaction mixture (100 μL) was removed and directly analyzed by ESI-MS.

Degradation study in an environmental chamber: Nanocomposites (5 mg) were applied into crude oil (20 μL)-contaminated water (2 mL), which was adjusted to pH 8 with NaOH to mimic sea water. Crude oil sequestration experiments by nanocomposites were conducted as previously stated. The mixture of uncovered crude oil, alkaline water, and nanocomposites remaining in water was transferred to an environmental chamber that was set to 22 °C and 70% relative humidity. An aliquot of the reaction mixture (100 μL) was removed and directly analyzed by ESI-MS immediately and after 20, 50, and 100 d.

Results and Discussions

Design of the sugar-based magnetic hybrid nanoparticles. The magnetic nanocomposites were constructed by an overall three step sequence that involved independent preparation of amphiphilic triblock terpolymers, poly(ethylene glycol)-*b*-dopamine-functionalized poly(ethyl propargyl glucose carbonate)-*b*-poly(ethyl glucose carbonate, PEG-*b*-PGC[(EPC-MPA)-*co*-(EPC-DOPA)]-*b*-PGC(EC), and magnetic iron oxide nanoparticles (MIONs), followed by their co-assembly, as illustrated in **Scheme IV-1**. Using

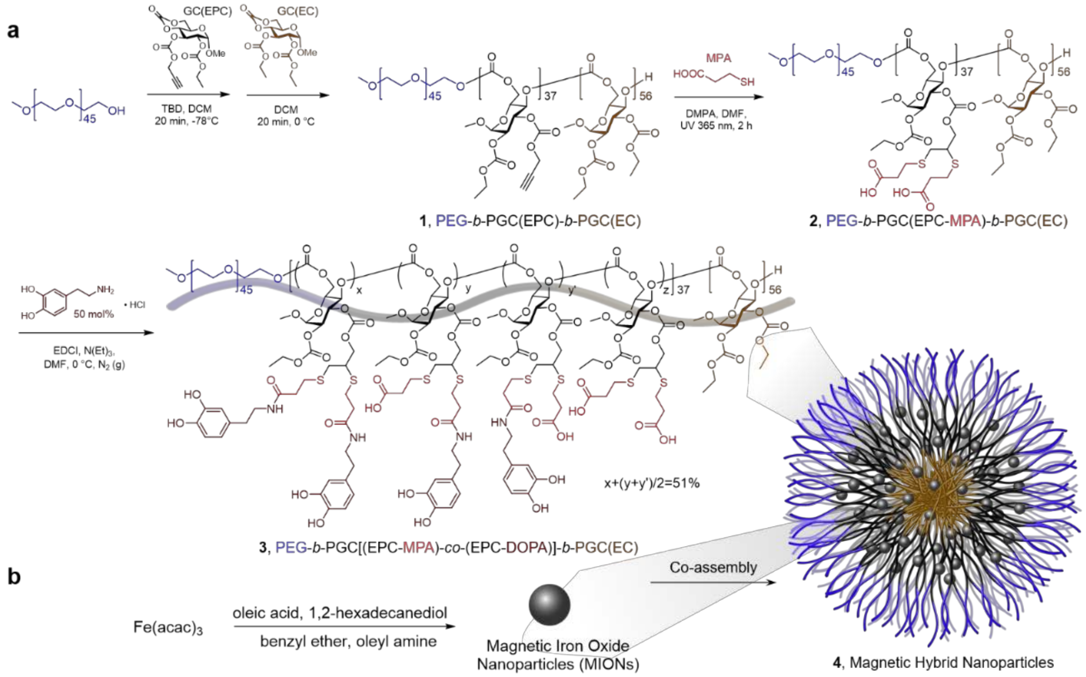

Scheme IV-1 (a) Synthesis of polymer **1**, PEG-*b*-PGC(EPC)-*b*-PGC(EC) by sequential ROPs of glucose carbonate monomers from a PEG macroinitiator, followed by post-polymerization modification *via* thiol-yne reaction with 3-mercaptopropionic acid (MPA) to prepare polymer **2**, PEG-*b*-PGC(EPC-MPA)-*b*-PGC(EC), and functionalization of polymer **2** with dopamine hydrochloride to afford polymer 3, PEG-*b*-PGC[(EPC-MPA)-*co*-(EPC-DOPA)]-*b*-PGC(EC). (b) Synthesis of magnetic iron oxide nanoparticles (MIONs), and co-assembly of **3** and MIONs to afford magnetic hybrid nanoparticles **4**.

poly(ethylene glycol) (PEG) as the hydrophilic component and macroinitiator, sequential ring-opening polymerizations (ROPs) of two glucose-derived cyclic carbonate monomers afforded amphiphilic PEG-*b*-PGC with two hydrophobic segments carrying either ethyl+propargyl or ethyl+ethyl side chain functionalities. The resulting triblock terpolymers **1**, PEG-*b*-PGC(EPC)-*b*-PGC(EC), dispersed readily in water but were unable to produce co-assembled nanostructures with MIONs. Because it was hypothesized that the chemical composition of **1** provided insufficient interactions with MIONs, dopamine moieties were introduced as high-affinity anchor groups to facilitate MION encapsulation.[222-224] Thiol-yne click chemistry[225-227] of **1** with 3-mercaptopropionic acid (MPA) yielded intermediate **2**, PEG-*b*-PGC(EPC-MPA)-*b*-PGC(EC), which was then followed by amidation with dopamine to afford PEG-*b*-PGC[(EPC-MPA)-*co*-(EPC-DOPA)]-*b*-PGC(EC), **3**. Finally, co-assembly of **3** with MIONs upon exchange from organic solvent to water resulted in formation of the magnetic nanocomposites **4**.

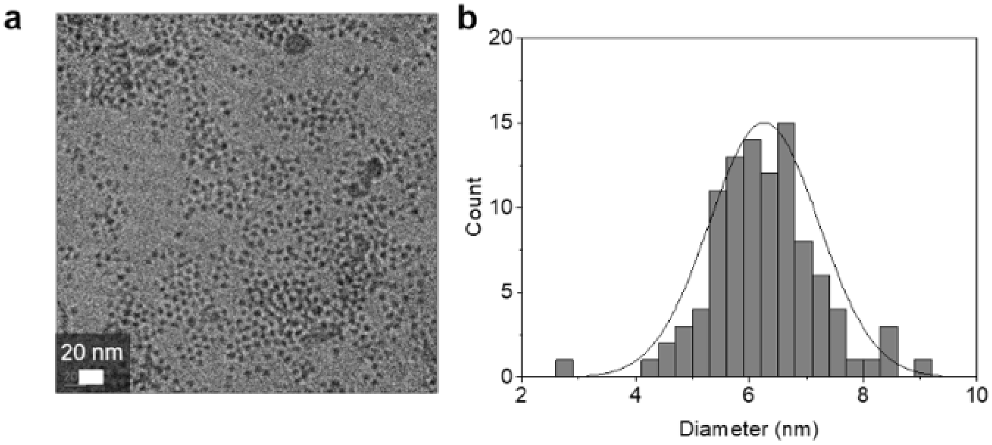

Figure IV-2 (a) Transmission electron microscopy (TEM) image of MIONs. The TEM sample was drop-cast from a THF solution (*ca.* 5 mg/mL, 5 µL) with no stain; the average diameter was determined by measurement of > 100 nanoparticles. (b) Histogram of MIONs showing a D_{av} of 6 ± 1 nm.

Thermal synthesis of MIONs. The synthesis of MIONs was carried out following a standard air-free procedure, where a high-temperature solution-phase reaction of iron(III) acetylacetonate [Fe(acac)$_3$] and 1,2-hexadecanediol was conducted in the presence of oleic acid and oleylamine as (co-)surfactants.[221, 228] The as-synthesized MIONs were characterized by transmission electron microscopy (TEM) imaging and superconducting quantum interference device (SQUID) magnetometry measurements. TEM showed nanoparticles with a number-averaged diameter (D_{av}) of 6 ± 1 nm, upon analysis of more than 100 nanoparticles (**Fig. IV-2**). SQUID magnetometry on MIONs indicated that the particles were in the superparamagnetic regime at room temperature, *i.e.* the particles became magnetic in the presence of an applied magnetic field, enabling magnetic separation and recycling (**Fig. IV-3**).

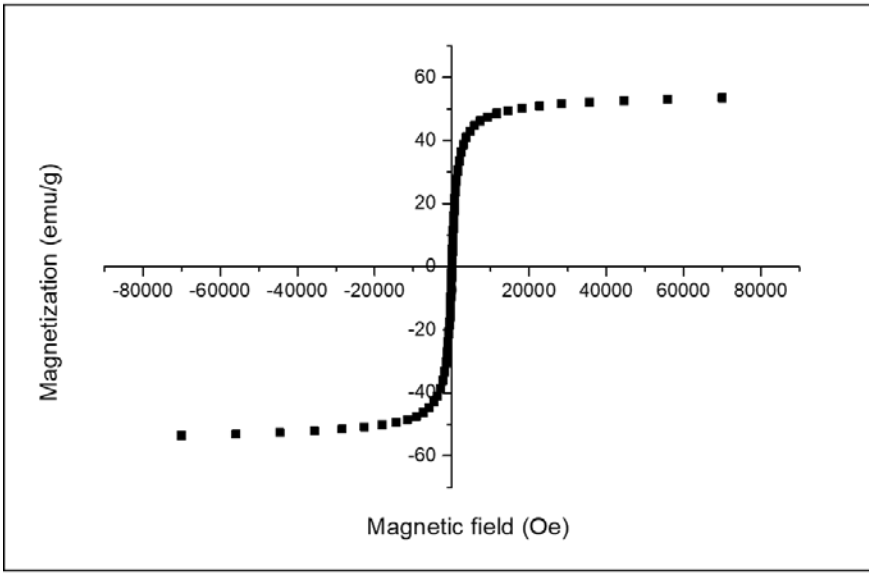

Figure IV-3 SQUID magnetometry analysis showing magnetization vs. applied magnetic field for iron oxide nanoparticles.

Synthesis and post-polymerization modification of functional sugar-based degradable amphiphilic block terpolymers. The functional triblock terpolymer **1** was synthesized by rapid organobase-catalyzed sequential ROPs of the glucose-based monomers GC(EPC) and GC(EC) in dichloromethane (DCM) with $mPEG_{45}$ as the hydrophilic macroinitiator and 1,5,7-triazabicyclo[4.4.0]-dec-5-ene (TBD) as the organocatalyst (**Scheme IV-1**). The PGC(EPC) block carried alkyne functional groups allowing for further chemical modification by click chemistry to install functionalities and afford hydrophilicity; while the PGC(EC) block was incorporated to serve as a constant hydrophobic segment. The polymerization of GC(EPC) was allowed to proceed in a -78 °C dry ice/acetone bath for 6-10 min, according to previous literature.[213] The reaction flask was then transferred to an ice water bath, the GC(EC) monomer was added, and growth of the PGC(EC) block was conducted over a period of 20 min to achieve quantitative chain extension. The reaction was quenched by adding an excess amount of acetic acid, and the polymer product was isolated by precipitation in diethyl ether three times and dried *in vacuo* to yield a white powder. Analysis of the size exclusion chromatography (SEC) trace of the resulting polymer **1** relative to that of mPEG$_{45}$ confirmed a controlled polymerization to afford a block polymer structure having an increased hydrodynamic diameter and a monomodal molar mass distribution with low dispersity ($Đ$ = 1.08) (**Fig. IV-4a**). The block length ratio between PEG, PGC(EPC) and PGC(EC) of the block terpolymer **3** was determined by ^{1}H NMR spectroscopy to be 45:37:56 by comparing the integration of the methylene protons resonating at 3.63 ppm from the macroinitiator PEG with the integrations of the proton resonances at 3.40 ppm from methoxy groups and at 2.58 ppm from the terminal alkynes in the PGC segments (**Fig. IV-4b**).

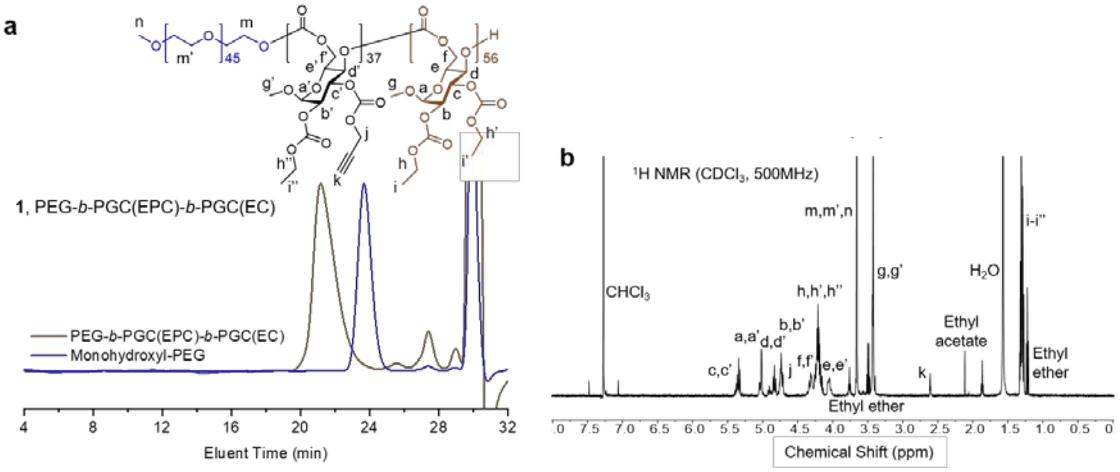

Fig. IV-4 (a) SEC trace (THF as eluent, 1mL/min) and (b) ^{1}H NMR (500 MHz, $CDCl_3$) spectrum of sugar-based triblock terpolymer **1** with alkyne functional groups.

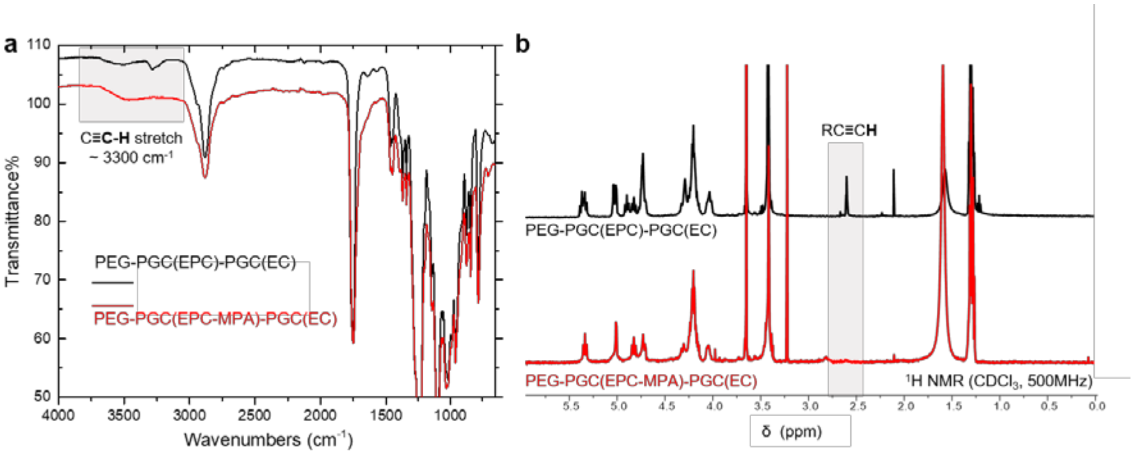

Figure IV-5 (a) FT-IR spectra of triblock polymers **1** (black line) and **2** (red line) before and after the thiol-yne click reaction with MPA, showing the disappearance of the alkynyl C-H stretch at 3300 cm^{-1}. (b) ^{1}H NMR spectra (500 Hz, CDCl$_3$) of polymers **1** and **2**, showing the disappearance of the proton resonance from the alkyne group at 2.60 ppm.

The alkyne-containing polymer **1** was further reacted with MPA in the presence of photoinitiator 2,2-dimethoxy-2-phenylacetophenone (DMPA) under UV irradiation for 2 h to afford the carboxylic acid-functionalized block terpolymer **2** (**Scheme IV-2**). The reaction mixture was transferred to dialysis tubing and dialyzed against nanopure water at room temperature for 3 d to remove excess thiol and solvent residues, followed by lyophilization. The polymer was re-dissolved in THF and precipitated into diethyl ether to remove DMPA residues, then dried under vacuum to yield block terpolymer **2** as a white powder. The disappearance of the proton resonance at 2.58 ppm in the ^{1}H NMR spectrum, as shown in **Fig. IV-5b**, demonstrated the successful consumption of the terminal alkynyl groups during the post-polymerization modification *via* thiol-yne click chemistry. Fourier transform infrared (FT-IR) spectroscopy further supported that this reaction had occurred together with the introduction of carboxylic acid groups by the appearance of a broad O-

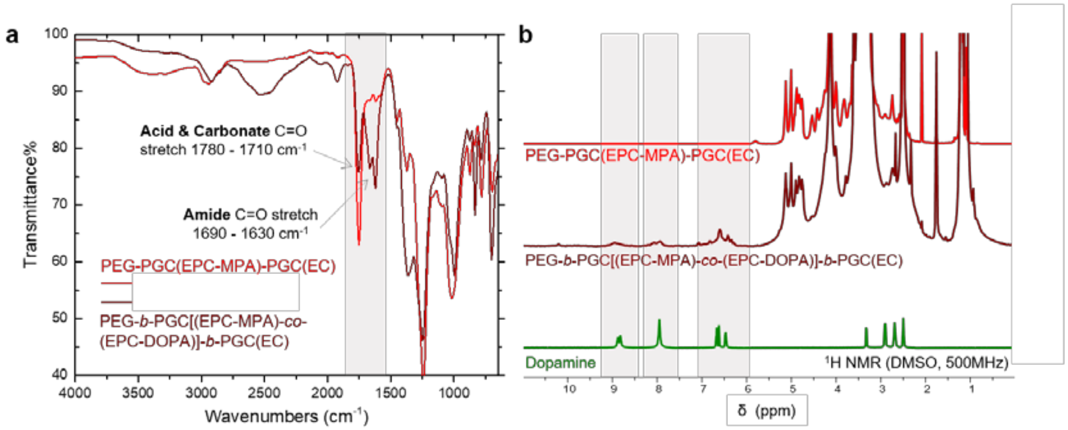

Figure IV-6 (a) FT-IR spectra of triblock polymer **2** (red line) and **3** (maroon line) before and after the amidation reaction with dopamine, showing the shift of the C=O stretch from the carboxylic acid to amide carbonyl groups. (b) ^{1}H NMR spectra (500 Hz, DMSO-d$_6$) of triblock polymers **2**, **3,** and dopamine hydrochloride (green line), showing the appearance of proton resonance from dopamine at 6.25 – 6.75 ppm, 7.75 - 8.25 ppm, and 8.75 – 9.25 ppm.

H stretching band from 3700 to 3000 cm^{-1} coincident with the disappearance of a sharper alkynyl C-H stretch at 3300 cm^{-1} (**Fig. IV-5a**).

The DOPA-functionalized block terpolymer **3** was obtained by amidation of the carboxylic acids on **2** with dopamine, as shown in **Scheme 1 and Scheme S3**.[229] Polymer **2** and dopamine hydrochloride were allowed to undergo reaction at 0 °C in the presence of 1-ethyl-3-(3-dimethylaminopropyl)-1-ethyl-carbodiimide hydrochloride (EDC hydrochloride) and triethyl amine in anhydrous DMF. The reaction vessel was under continuous nitrogen flow and wrapped with aluminium foil to avoid potential side reactions, *e.g.* polymerization of dopamine. FT-IR spectroscopy showed a shift of a portion of the C=O stretch intensity from 1750 cm^{-1} to 1660 cm^{-1} upon amidation, corresponding to transformation of the carboxylic acids to amides with retention of the carbonate carbonyl groups (**Fig. IV-6a**). The appearance of resonances from the dopamine aromatic protons between 6.25 – 6.75 ppm in the ^{1}H NMR spectrum (**Fig. IV-6b**), indicated *ca.* 50% functionalization of the carboxylic acids of the polymer backbone by dopamine moieties. Taken together, these results demonstrated the successful synthesis of the sugar-based amphiphilic triblock terpolymer **3**, having the complex compositional profile illustrated in **Scheme IV-1**.

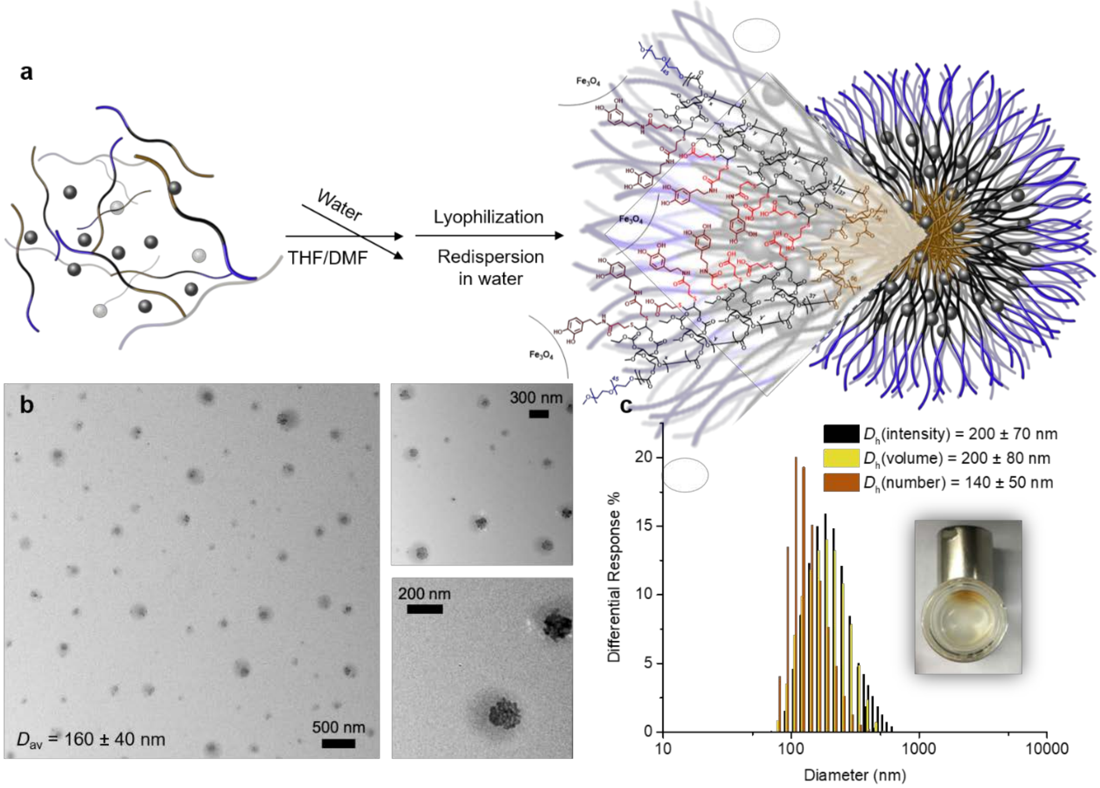

Figure IV-7 (a) Schematic representation of the construction of nanocomposites 4. (b) TEM of **4** was drop-casted from an aqueous dispersion (without stain); the scale bars in TEM images are 500, 300 and 200 nm. The average diameter was measured by counting > 50 particles. (c) Intensity-, volume-, and number-average DLS histograms of 4 dispersed in aqueous solution (*ca.* 1 mg/mL), and the inset photo shows the top view of nanocomposites 4 collected on a vial wall by application of an external magnet.

Co-assembly of MIONs and sugar-based polymeric scaffolds. The co-assembly of MIONs and **3** was performed through a solvent exchange process, modified from previous reports (**Fig. IV-7a**).[51, 230] The block lengths of the PEG and PGC-based blocks were tuned to balance the dispersion in water and interactions of dopamine with MIONs. MIONs and **3** were first dispersed in THF and DMF, respectively, to form homogeneously-distributed solutions. The two solutions were thoroughly mixed at a volume ratio of 1:1 by vortex and sonication to afford a clear brown mixture. Afterwards, nanopure water (2× relative to organic solution volume) was added dropwise *via* a syringe pump, followed by a rapid addition of another 2× nanopure water, where the water served as a selective poor solvent for both the hydrophobic PGC(EC) block and the MIONs, inducing the formation of micelles with capture of the nanoparticles. This technique was hypothesized to first allow quasi-equilibrium assembly through slow addition, and then kinetically trap the morphology *via* rapid addition.[231-232] Excess organic solvent was then removed by dialysis against nanopure water for 24 h. Finally, the magnetic nanocomposite solution was lyophilized to yield a brown powder. TEM analysis showed that each globular polymeric micelle had encapsulated multiple MIONs with a D_{av} of 160 ± 40 nm, after measuring > 50 nanoparticles (**Fig. IV-7b**). Dark-field scanning transmission electron microscopy

(STEM) and elemental mapping measurements were performed on the MION-loaded nanocomposites using an energy-dispersive X-ray spectroscopy (EDS) detector showing the co-localization of iron oxide and nanocomposites, according to the iron (Fe) intensity profile and dark field STEM images, respectively, which further demonstrated that MIONs were loaded into the polymeric matrix (**Fig. IV-8a-d**). In addition, thermogravimetric analysis (TGA) of MIONs and **3** under nitrogen atmosphere showed less than 30% and more than 90% mass loss for MIONs and polymeric scaffold upon heating to 500 °C, respectively, whereas the nanocomposites were found to retain 20% of mass, suggesting *ca.* 20% thermally stable inorganic components were contained inside the nanocomposites (**Fig. IV-8e**). Narrowly dispersed nanocomposites with a number-average hydrodynamic diameter (D_h(number)) of 140 ± 50 nm were also observed by

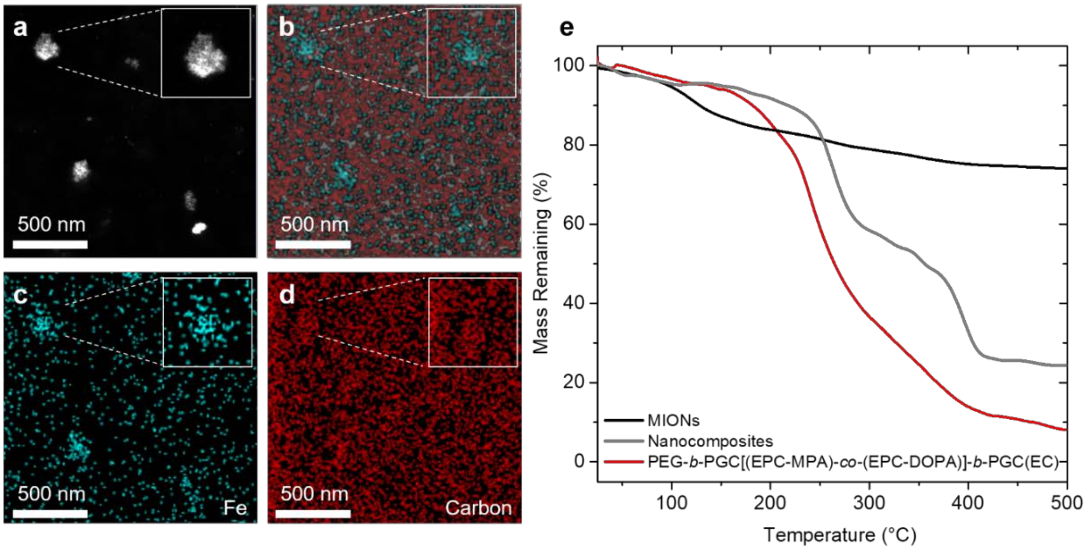

Figure IV-8 Dark-field STEM image and elemental mapping of nanocomposite **4** by EDS detector in STEM mode (a) dark-field STEM image, (b) merged elemental mapping images of iron (Fe) and carbon, (c) elemental mapping images of iron and (d) carbon. (e) Thermogravimetric analysis of MIONs (black line), polymer **3** (red line), and nanocomposites (grey line).

dynamic light scattering (DLS). The slightly larger dry-state diameter measured by TEM is expected to be caused by some degree of deformation upon deposition and drying on the carbon-coated copper grid for TEM imaging (**Fig. IV-7c**). Further support for reorganization and flattening of the globular nanostructures on substrates was found by measurement of an average height of *ca.* 17.6 ± 1.7 nm by atomic force microscopy (AFM) (**Fig. IV-9**).

Quantitative evaluation of crude oil loading capacity and recyclability of the sugar-based magnetic nanocomposites. Following the full characterization of the sugar-based magnetic nanocomposites, their ability to sequester complex oil pollutants was assessed qualitatively and quantitatively. Crude oil (density = *ca.* 0.76 mg/mL) was obtained from the Texas-Oklahoma Enbridge pipeline and then weathered according to a previously

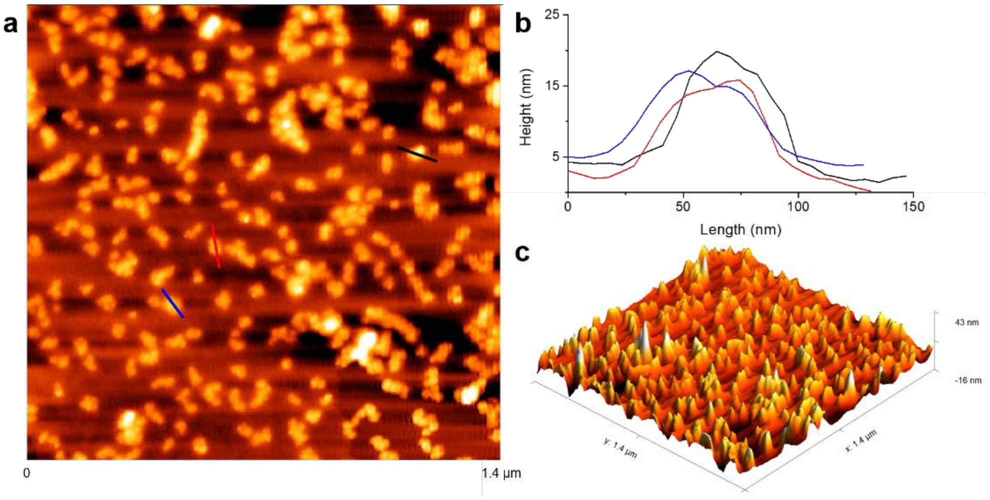

Figure IV-9 (a) AFM micrographs, (b) height profile, (c) 3D image of nanocomposites **4**. Sample was drop cast onto the freshly cleaved mica, and then left to dry under the ambient condition. The height profiles were measured along the colored lines shown on the micrographs.

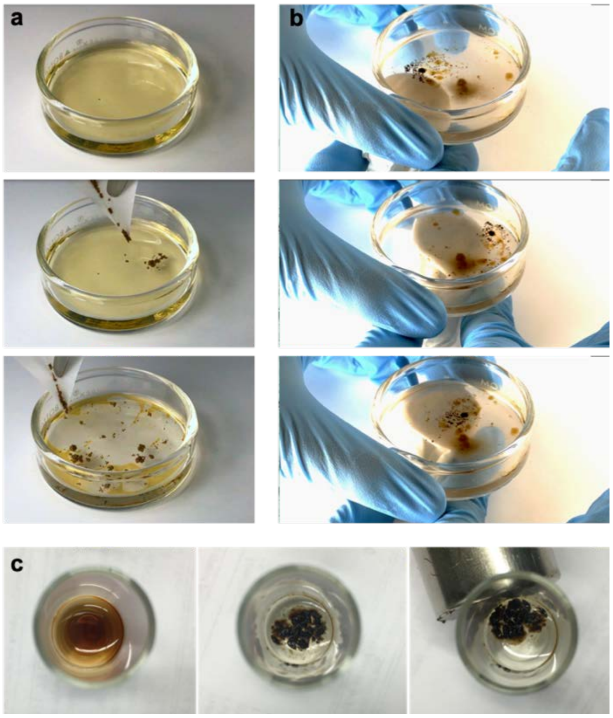

Figure IV-10 Representative photographs of (a) crude oil sheen before and during addition of nanocomposites **4**, (b) the crude oil-loaded nanocomposites 4 attracted by a moving magnet at the bottom of the container, and (c) quantitative oil sequestration experiments showing that the vial containing crude-oil contaminated water before and after oil sorption by **4**. (Videos illustrating (a) and (b) are available in the Supporting Information.)

established procedure.[233] As shown in **Fig. IV-10a**, firstly, several drops of crude oil were added to water in order to mimic the oil sheen on the water surface. Secondly, lyophilized samples of sugar-based magnetic nanocomposites were applied, which floated on the surface. Within several seconds, the nanocomposites had uptake sufficient crude oil to break up the oil sheen, as shown in the video of **Fig. IV-11** included in the Supporting Information. Results from experiments that are shown by the panels of images captured within **Fig. IV-10b** and **IV-10c** indicated that the crude oil-loaded nanocomposites were capable of following the motion of the external magnet remotely (see also the video of **Fig. IV-12**), eventually being separated from the water together with the oil pollutants. Quantitative oil sequestration experiments were also pursued by deploying the lyophilized nanocomposite powder to crude oil-contaminated water samples at nanocomposite/crude oil (mg/µL) ratios of 1:5, 1:10, 1:15, 1:20, 1:25, and 1:30 (**Fig. IV-13a**, **Table IV-1**). The nanocomposite-oil-water mixtures were allowed to stand for *ca.* 10 h, a time period far in excess of that needed to reach a visually-apparent steady state of crude oil capture. As the crude oil was taken up by the magnetic nanocomposites, the oil layer on the surface of the water diminished while the originally light brown nanocomposite powder darkened in colour (**Fig. IV-10a-c** and **Fig. IV-11**). Quantitative assessments were performed after an external magnet (neodymium magnet, 90 lb pull) was used to attract the loaded nanocomposites. A rapid magnetic response was observed – just several seconds were required to collect the nanocomposites and decant the purified water into a new vial. The loaded nanocomposites were then washed twice with diethyl ether to extract the crude oil and the magnet was used to collect the recovered nanocomposites. The resulting crude oil and diethyl ether mixture was transferred to another pre-weighed clean vial and concentrated. The amounts of crude oil pollutants captured by nanocomposites were thereby quantified. **Fig. IV-13b** shows that the crude oil uptake ability of the

Table IV-1 Quantitative evaluation of crude oil loading capacity by nanocomposites

	1:5[a]	1:10	1:15	1:20	1:25	1:30
1st experiment	4.4[b] mg	8.9 mg	13.9 mg	14.5 mg	15.3 mg	18.9 mg
2nd experiment	3.8 mg	7.6 mg	10.4 mg	16.8 mg	15.5 mg	14.8 mg
3rd experiment	4.2 mg	8.8 mg	12.2 mg	20.6 mg	15.3 mg	16.7 mg
Average (mg per mg of nanocomposites).	2.1 ± 0.1	4.2 ± 0.3	6.1 ± 0.7	8.7 ± 1.3	7.7 ± 0.1	8.4 ± 1.7
$\frac{Sequestered\ Oil\ (mg)}{Initial\ Oil\ (mg)}$	0.54	0.56	0.53	0.57	0.40	0.37

[a] The actual amount of nanocomposites and initial volume of crude oil used for 1:5, 1:10, 1:15, 1:20, 1:25, 1:30 are 2 mg nanocomposites and 10, 20, 30, 40, 50, 60 μL crude oil;

[b] The amount of crude oil (mg) recovered from 2 mL water by diethyl ether wash.

nanocomposites increased significantly from 1:5, 1:10, 1:15, to 1:20 of initial

Supplementary
video clip - crude oi

Figure IV-11 By clicking the .mp4 file above, or on the next page, see a video of the addition of lyophilized magnetic nanocomposites to a weathered mixture of crude oil and water in a petri dish.

Supplementary
video clip - magneti

Figure IV-12 By clicking the .mp4 file above, or on the next page, see a video of the magnetic action of lyophilized magnetic nanocomposites after absorption of crude oil from a weathered mixture of crude oil and water in a petri dish.

nanocomposite-to-oil ratio, then increased slowly when higher excesses of crude oil were deployed. Based on the results from sequestration experiments using 1:20, 1:25 and 1:30 initial nanocomposite-to-oil ratios, the sugar-based nanocomposites were able to recover 8× to 9× their initial dry weight of crude oil pollutants.

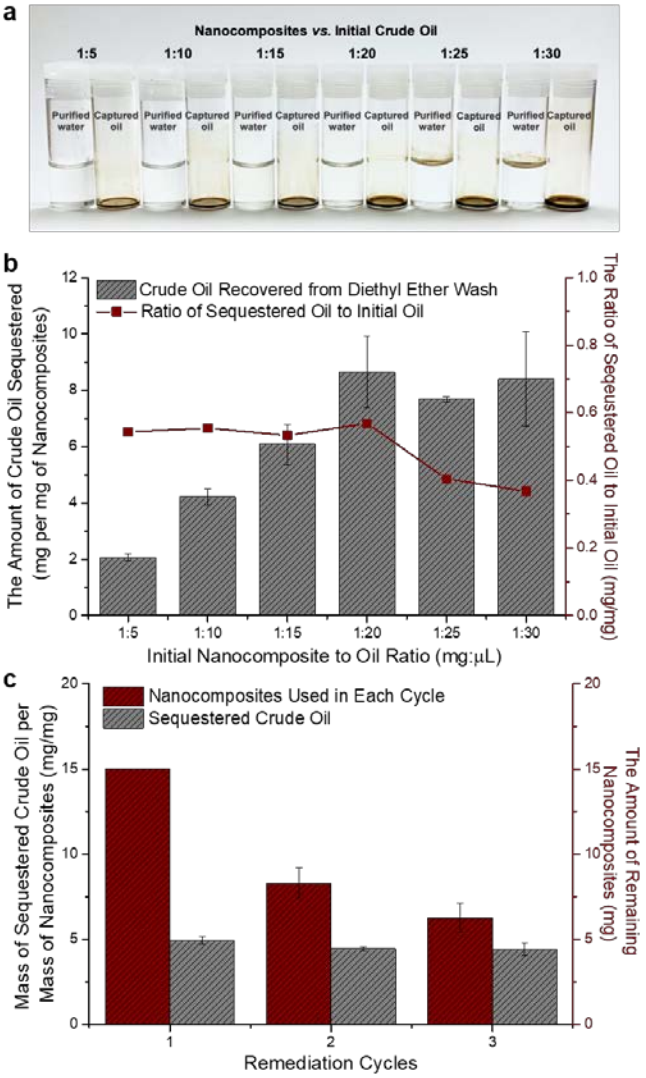

Figure IV-13 Quantitative evaluation of crude oil loading capacity and recyclability: (a) Photograph of recovered crude oil (left) and purified water (right) with different nanocomposites-to-crude oil ratios; (b) the amount of crude oil sequestered by nanocomposites **4** with different initial nanocomposites-to-crude oil ratios; (c) recycling performance of nanocomposites **4** evaluated by comparing the total amount of crude oil sequestered, nanocomposites used in each cycle, and crude oil sequestered per unit mass of nanocomposites **4**.

Recyclability of the nanocomposites was assessed by repeating the oil sequestration experiments for three cycles. The amount of crude oil used for each cycle was set as 150 μL and the initial nanocomposite was 15 mg. It was noted that 60 – 80 wt% of the nanocomposites were able to be retrieved each cycle, the loss of which was due to the sacrifice during deployment and organic solvent washing (**Fig. IV-13c**, **Table IV-2**). It was observed that the loading capacity of the reused nanocomposites maintained at *ca.* 5 mg/mg, suggesting the potential of sugar-based magnetic nanocomposites as recyclable agents for crude oil sequestration.

Table IV-2 Quantitative evaluation of nanocomposite recyclability

	1st cycle[a]			2nd cycle			3rd cycle		
	M[b] (mg)	N[c] (mg)	M/N[d]	M (mg)	N (mg)	M/N	M (mg)	N (mg)	M/N
1st experiment	78.9	15.0	5.3	43.0	9.5	4.5	29.0	7.4	3.9
2nd experiment	73.0	15.0	4.9	34.5	8.0	4.3	27.1	6.0	4.5
3rd experiment	70.3	15.0	4.7	33.4	7.4	4.5	26.2	5.4	4.9
Average	74.1 ± 3.6	15.0 ± 0	4.9 ± 0.2	37.0 ± 4.3	8.3 ± 0.9	4.5 ± 0.1	27.4 ±1.2	6.3 ± 0.8	4.4 ± 0.4

[a] The amount of nanocomposites and initial volume of crude oil for each cycle are 15 mg and 150 μL.

[b] The amount of crude oil (mg) recovered by diethyl ether wash;

[c] The actual amount of nanocomposite **4** (mg) retrieved from last cycle and used to recover oil for next cycle;

[d] The amount of recovered crude oil (mg) per unit mass of nanocomposite **4** (mg).

Degradation study in organic media, aqueous media, and an environmental chamber. Due to the fact that some of the nanocomposites may not be retrieved, it was pivotal to further study their degradation profile under different environmental conditions. A series of studies was performed over months in organic solvent, water, and an environmental chamber to simulate the degradation process of the nanocomposites in crude oil, aqueous media, and climatic conditions (**Fig. IV-14** and **IV-15**).

The degradation of **3** was investigated using ^{1}H NMR spectroscopy following incubation at 37 °C under basic conditions in D_2O and DMSO-d_6. A pristine polymer sample was dissolved into D_2O and DMSO-d_6 (5 mg/mL) containing NaOD and triethylamine,

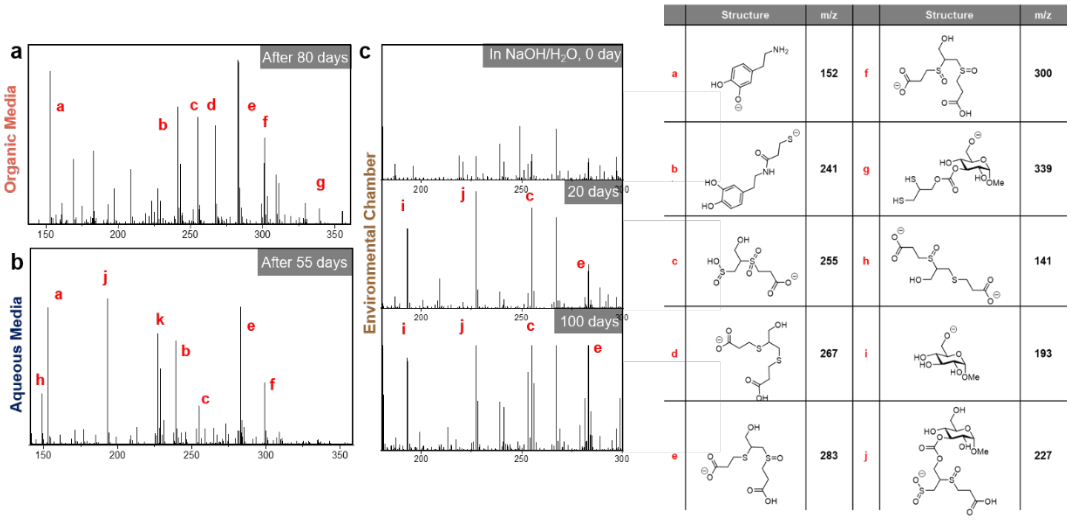

Figure IV-14 ESI-MS analysis of the degradation products of (a) triblock terpolymer **3** in DMSO-d_6 (5 mg/mL) with addition of D_2O (20% vol/vol) and triethylamine (6 mg/mL) during incubation with shaking at 37 °C over a period of 80 days; (b) triblock terpolymer **3** in D_2O (5 mg/mL) with addition of NaOD adjusted to pH 10 during incubation with shaking at 37 °C over a period of 55 days; (c) nanocomposites **4** in H_2O (5 mg/mL) with addition of NaOH adjusted to pH 8 in an environmental chamber (T = 22 °C, RH = 70%) over 100 days. Mass spectra are in negative-ion mode.

respectively. In both conditions, sharp peaks appeared and accumulated over time, as shown in **Fig. IV-15**, suggesting the generation of oligomers and small molecules from the original polymer backbone. The degradation products were analysed by electrospray ionisation mass spectrometry (ESI-MS), as shown in **Fig. IV-14a-b**. Additionally, environmental chamber testing was conducted to expose nanocomposites **4** to the climatic conditions that simulate the temperature and humidity of the Texas Gulf Coast, with an average annual temperature of 22 °C and an average annual relative humidity (RH) of 70%.[234] After retrieval of the loaded nanocomposites, the mixture of unrecovered crude oil and remaining nanocomposites in water was analysed by ESI-MS (**Fig. IV-14c**). The ESI-MS analysis shown in **Fig. IV-14a-c** suggested that the sugar-based polymer degraded into moieties with smaller molar masses, and the possible degradation products were presumed based on cleavage of labile carbonate backbone and carbonate, ester and

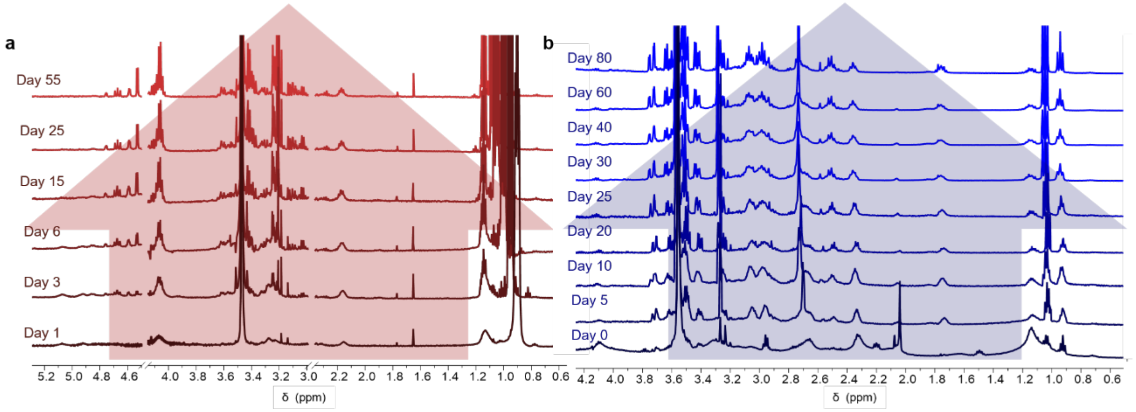

Figure IV-15 ^{1}H NMR (500 MHz) spectra of triblock polymers **3** acquired in (a) DMSO-d_6 (5 mg/mL) with addition of D_2O (20 vol %) and TEA (6 mg/mL) during incubation at 37 °C over 55 days and (b) in D_2O (5 mg/mL) with addition of NaOD adjusted to pH 10 during incubation at 37 °C over 80 days. It is noted that resonance of TEA was cut in spectrum (a).

amide side chain linkages in the presence of aqueous NaOH, as well as oxidation of thioethers into sulfoxides and sulfones during this long period of degradation.[235-236] The final degradation products and corresponding mechanism are under further investigation.

Conclusions

With an urgent need to develop sustainable and environmentally-friendly materials to tackle the threat of crude oil pollution, magnetically-responsive nanocomposites derived from sugar were designed and studied. By merging polymer materials and nanotechnology, this composite material served as nano-sized carriers for pollutant absorption. It was observed that these sugar-based magnetic nanocomposites act as a dispersible agent to effectively absorb crude oil nearly ten-fold their initial dry weight. Besides, the nanocomposites are able to carry versatile functionalities by virtue of the scalable and translatable chemical synthetic approach, enabling their utilization in the clean-up of other polluted resources. For example, fracking produced water has long been facing a major disposal challenge, given their large volumes as well as high levels of salinity, toxic metals, and radioactivity.[237] Upon modification with chelating agents, such as ethylenediaminetetraacetic acid, the nanocomposites hold promise for this problem. Furthermore, the pollutant-loaded composite materials can be remotely controlled and reused for multiple cycles, thereby, increasing their resource efficiency and lowering their energy and economic costs. Moreover, their degradability allows these nanocomposites to eventually break down into their natural building blocks and derivative small molecules, alleviating the production and persistence of microplastics. Therefore, the design of this material makes a significant contribution not only in pollution control and resource recovery, but also in developing a roadmap from our existing linear economy, towards a more sustainable and resource-efficient circular plastics economy.

CHAPTER V

CONCLUSIONS

This research dissertation has presented (1) the self-assembly of amphiphilic bottlebrush copolymers with a series of comparisons regarding various macromolecular topological parameters; (2) experimental and computational investigation of nanostructures obtained from self-assembly of amphiphilic coil-brush copolymers; (3) functional and degradable nanomaterial design by co-assembly of amphiphilic block copolymers and inorganic nanoparticles.

We firstly designed, synthesized and compared the nanoassemblies obtained from amphiphilic diblock copolymers with tunable backbone length, hydrophilic and hydrophobic side chain length, hydrophobic side chain chemistry and polymer architectures. It came to the conclusion that as the hydrophilic volume fraction increases or hydrophobic volume fraction decreases, the interfacial curvature between hydrophilic and hydrophobic blocks increases, resulting in a smaller-size and more distinct nanostructure in aqueous solution, such as spherical micelles. Whereas, as the hydrophilic volume fraction decreases or hydrophobic volume fraction increases, the interfacial curvature decreases, resulting in a bilayer nanostructure in water, one typical example is vesicles. Moreover, differences in the chemical structures of PGC and PDLLA, *i.e.*, bulky *vs.* linear, affect the morphology and size of resulting nanostructures as well.

Experimental synthesis and self-assembly of amphiphilic block copolymers have long been the major way to investigate the structure-property relationship of nanoscopic structures. However, as the complexity of polymers has been largely explored and many factors that are not dependent on polymer structures, such as kinetic factors, have appeared to be important essentials to consider regarding the self-assembly studies. Therefore, integration of experimental techniques and computational tools emerged as a demanding approach to better understand the underlying rules of solution assembly of macromolecules. Remarkably, there is a qualitative agreement in experimental and computational results of the nanostructures obtained from a series of well-defined P(NB-COOH)-*b*-P(NB-*g*-PGC) coil-brush block polymers. Generally, coil-brush block polymers with lower hydrophilicity tend to produce vesicles or cylinders, while polymers with higher hydrophilicity are likely to form spherical structures and pearl necklace-like nanostructures. Pearl necklace-like nanostructures were observed at intermediate hydrophilic-hydrophobic compositions. It is found that the length of the hydrophobic side chains also impacts the curvature of the interface between the hydrophilic corona and hydrophobic core, therefore affecting their morphology. In addition, poly(glucose carbonate)s also offer advantages in producing increasingly complex nanostructures, derived from natural building blocks to afford functional properties and allow for subsequent breakdown.

The advantages brought from degradable glucose-derived polycarbonates have also shown towards the need of developing sustainable and environmentally-friendly materials to tackle the threat of crude oil pollution. By hybridization of polymer materials and inorganic nanoparticles, magnetically-responsive nanocomposites were designed and studied this composite material served as nano-sized carriers for pollutant recovery. These glucose-based magnetic nanocomposites mainly serve as dispersible agents to recover crude oil nearly ten-fold their initial dry weight, due to it sophisticated core-shell structure. Besides, the pollutant-loaded nanocomposites can be remotely retrieved and reused for multiple cycles, therefore promoting their resource efficiency and reducing their energy and economic costs. Moreover, these nanocomposites are able to eventually break down into environmentally benign small molecules after their service life, relieving the pressure caused by the production and persistence of microplastics.

In summary, this dissertation has discussed the fundamental research on the self-assembly and co-assembly behaviours of amphiphilic polymers, and their application in the design of functional materials. It shows that by tailoring the composition and structure of amphiphilic block copolymers, there is a great potential that diversified functions can be incorporated into the functional and degradable polymeric materials.

REFERENCES

1. Riess, G., Micellization of block copolymers. *Prog. Polym. Sci.* **2003,** *28* (7), 1107-1170.
2. Zhang, S., Fabrication of novel biomaterials through molecular self-assembly. *Nat Biotech* **2003,** *21* (10), 1171-1178.
3. Mendes, A. C.; Baran, E. T.; Reis, R. L.; Azevedo, H. S., Self-assembly in nature: using the principles of nature to create complex nanobiomaterials. *WIREs Nanomedicine and Nanobiotechnology* **2013,** *5* (6), 582-612.
4. Blanazs, A.; Armes, S. P.; Ryan, A. J., Self‐assembled block copolymer aggregates: from micelles to vesicles and their biological applications. *Macromol. Rapid Commun.* **2009,** *30* (4‐5), 267-277.
5. Israelachvili, J. N., *Intermolecular and surface forces*. Academic press: 2011.
6. Israelachvili, J. N.; Mitchell, D. J.; Ninham, B. W., Theory of self-assembly of hydrocarbon amphiphiles into micelles and bilayers. *Journal of the Chemical Society, Faraday Transactions 2: Molecular and Chemical Physics* **1976,** *72* (0), 1525-1568.
7. Nagarajan, R., Molecular Packing Parameter and Surfactant Self-Assembly: The Neglected Role of the Surfactant Tail. *Langmuir* **2002,** *18* (1), 31-38.
8. Blanazs, A.; Madsen, J.; Battaglia, G.; Ryan, A. J.; Armes, S. P., Mechanistic insights for block copolymer morphologies: how do worms form vesicles? *J. Am. Chem. Soc.* **2011,** *133* (41), 16581-16587.

9. Yu, K.; Eisenberg, A., Bilayer Morphologies of Self-Assembled Crew-Cut Aggregates of Amphiphilic PS-b-PEO Diblock Copolymers in Solution. *Macromolecules* **1998,** *31* (11), 3509-3518.

10. Jain, S.; Bates, F. S., Consequences of Nonergodicity in Aqueous Binary PEO−PB Micellar Dispersions. *Macromolecules* **2004,** *37* (4), 1511-1523.

11. Hayward, R. C.; Pochan, D. J., Tailored Assemblies of Block Copolymers in Solution: It Is All about the Process. *Macromolecules* **2010,** *43* (8), 3577-3584.

12. Zhong, S.; Cui, H.; Chen, Z.; Wooley, K. L.; Pochan, D. J., Helix self-assembly through the coiling of cylindrical micelles. *Soft Matter* **2008,** *4* (1), 90-93.

13. Cui, H.; Chen, Z.; Wooley, K. L.; Pochan, D. J., Origins of toroidal micelle formation through charged triblock copolymer self-assembly. *Soft Matter* **2009,** *5* (6), 1269-1278.

14. Cui, H.; Chen, Z.; Zhong, S.; Wooley, K. L.; Pochan, D. J., Block copolymer assembly via kinetic control. *Science* **2007,** *317* (5838), 647-650.

15. Zhu, J.; Hayward, R. C., Spontaneous generation of amphiphilic block copolymer micelles with multiple morphologies through interfacial instabilities. *J. Am. Chem. Soc.* **2008,** *130* (23), 7496-7502.

16. Shen, L.; Wang, H.; Guerin, G.; Wu, C.; Manners, I.; Winnik, M. A., A micellar sphere-to-cylinder transition of poly (ferrocenyldimethylsilane-b-2-vinylpyridine) in a selective solvent driven by crystallization. *Macromolecules* **2008,** *41* (12), 4380-4389.

17. Chen, Q.; Zhao, H.; Ming, T.; Wang, J.; Wu, C., Nanopore extrusion-induced transition from spherical to cylindrical block copolymer micelles. *J. Am. Chem. Soc.* **2009,** *131* (46), 16650-16651.

18. Pochan, D. J.; Zhu, J.; Zhang, K.; Wooley, K. L.; Miesch, C.; Emrick, T., Multicompartment and multigeometry nanoparticle assembly. *Soft Matter* **2011,** *7* (6), 2500-2506.

19. Christian, D. A.; Tian, A.; Ellenbroek, W. G.; Levental, I.; Rajagopal, K.; Janmey, P. A.; Liu, A. J.; Baumgart, T.; Discher, D. E., Spotted vesicles, striped micelles and Janus assemblies induced by ligand binding. **2009,** *8*, 843.

20. Zhang, K.; Rossin, R.; Hagooly, A.; Chen, Z.; Welch, M. J.; Wooley, K. L., Folate-mediated cell uptake of shell-crosslinked spheres and cylinders. *J. Polym. Sci., Part A: Polym. Chem.* **2008,** *46* (22), 7578-7583.

21. Zhang, K.; Fang, H.; Chen, Z.; Taylor, J.-S. A.; Wooley, K. L., Shape Effects of Nanoparticles Conjugated with Cell-Penetrating Peptides (HIV Tat PTD) on CHO Cell Uptake. *Bioconjugate Chem.* **2008,** *19* (9), 1880-1887.

22. Lee, N. S.; Lin, L. Y.; Neumann, W. L.; Freskos, J. N.; Karwa, A.; Shieh, J. J.; Dorshow, R. B.; Wooley, K. L., Influence of Nanostructure Morphology on Host Capacity and Kinetics of Guest Release. *Small* **2011,** *7* (14), 1998-2003.

23. Li, Z.; Sun, L.; Zhang, Y.; Dove, A. P.; O'Reilly, R. K.; Chen, G., Shape Effect of Glyco-Nanoparticles on Macrophage Cellular Uptake and Immune Response. *ACS Macro Lett.* **2016,** *5* (9), 1059-1064.

24. Hu, X.; Zhang, Y.; Xie, Z.; Jing, X.; Bellotti, A.; Gu, Z., Stimuli-Responsive Polymersomes for Biomedical Applications. *Biomacromolecules* **2017,** *18* (3), 649-673.

25. Discher, D. E.; Ortiz, V.; Srinivas, G.; Klein, M. L.; Kim, Y.; Christian, D.; Cai, S.; Photos, P.; Ahmed, F., Emerging Applications of Polymersomes in Delivery: from Molecular Dynamics to Shrinkage of Tumors. *Prog. Polym. Sci.* **2007,** *32* (8-9), 838-857.

26. Thurmond, K. B.; Kowalewski, T.; Wooley, K. L., Water-Soluble Knedel-like Structures: The Preparation of Shell-Cross-Linked Small Particles. *J. Am. Chem. Soc.* **1996,** *118* (30), 7239-7240.

27. Thurmond, K. B.; Kowalewski, T.; Wooley, K. L., Shell Cross-Linked Knedels: A Synthetic Study of the Factors Affecting the Dimensions and Properties of Amphiphilic Core-Shell Nanospheres. *J. Am. Chem. Soc.* **1997,** *119* (28), 6656-6665.

28. Nystrom, A. M.; Xu, Z.; Xu, J.; Taylor, S.; Nittis, T.; Stewart, S. A.; Leonard, J.; Wooley, K. L., SCKs as nanoparticle carriers of doxorubicin: investigation of core composition on the loading, release and cytotoxicity profiles. *Chem. Commun.* **2008,** (30), 3579-3581.

29. Du, W.; Xu, Z.; Nyström, A. M.; Zhang, K.; Leonard, J. R.; Wooley, K. L., 19F- and Fluorescently Labeled Micelles as Nanoscopic Assemblies for Chemotherapeutic Delivery. *Bioconjugate Chem.* **2008,** *19* (12), 2492-2498.

30. Lin, L. Y.; Lee, N. S.; Zhu, J.; Nyström, A. M.; Pochan, D. J.; Dorshow, R. B.; Wooley, K. L., Tuning core vs. shell dimensions to adjust the performance of

nanoscopic containers for the loading and release of doxorubicin. *J. Control. Release* **2011,** *152* (1), 37-48.

31. Verduzco, R.; Li, X.; Pesek, S. L.; Stein, G. E., Structure, function, self-assembly, and applications of bottlebrush copolymers. *Chem. Soc. Rev.* **2015,** *44* (8), 2405-2420.
32. Rzayev, J., Molecular bottlebrushes: new opportunities in nanomaterials fabrication. ACS Publications: 2012.
33. Müllner, M.; Müller, A. H. E., Cylindrical polymer brushes – Anisotropic building blocks, unimolecular templates and particulate nanocarriers. *Polymer* **2016,** *98* (Supplement C), 389-401.
34. Rzayev, J., Molecular Bottlebrushes: New Opportunities in Nanomaterials Fabrication. *ACS Macro Lett.* **2012,** *1* (9), 1146-1149.
35. Müllner, M.; Müller, A. H., Cylindrical polymer brushes–Anisotropic building blocks, unimolecular templates and particulate nanocarriers. *Polymer* **2016,** *98*, 389-401.
36. Tonge, C. M.; Hudson, Z. M., Interface-Dependent Aggregation-Induced Delayed Fluorescence in Bottlebrush Polymer Nanofibers. *J. Am. Chem. Soc.* **2019,** *141* (35), 13970-13976.
37. Pyun, J., Nanocomposite Materials from Functional Polymers and Magnetic Colloids. *Polymer Reviews* **2007,** *47* (2), 231-263.

38. Zhang, H.; Liu, Y.; Yao, D.; Yang, B., Hybridization of inorganic nanoparticles and polymers to create regular and reversible self-assembly architectures. *Chem. Soc. Rev.* **2012,** *41* (18), 6066-6088.

39. Burda, C.; Chen, X.; Narayanan, R.; El-Sayed, M. A., Chemistry and properties of nanocrystals of different shapes. *Chem. Rev.* **2005,** *105* (4), 1025-1102.

40. Ferrando, R.; Jellinek, J.; Johnston, R. L., Nanoalloys: from theory to applications of alloy clusters and nanoparticles. *Chem. Rev.* **2008,** *108* (3), 845-910.

41. Wang, J.; Li, W.; Zhu, J., Encapsulation of inorganic nanoparticles into block copolymer micellar aggregates: Strategies and precise localization of nanoparticles. *Polymer* **2014,** *55* (5), 1079-1096.

42. Yuan, J.; Müller, A. H. E., One-dimensional organic–inorganic hybrid nanomaterials. *Polymer* **2010,** *51* (18), 4015-4036.

43. Caruso, F.; Susha, A. S.; Giersig, M.; Möhwald, H., Magnetic Core–Shell Particles: Preparation of Magnetite Multilayers on Polymer Latex Microspheres. *Adv. Mater.* **1999,** *11* (11), 950-953.

44. Deng, Y. H.; Yang, W. L.; Wang, C. C.; Fu, S. K., A Novel Approach for Preparation of Thermoresponsive Polymer Magnetic Microspheres with Core–Shell Structure. *Adv. Mater.* **2003,** *15* (20), 1729-1732.

45. Pich, A.; Bhattacharya, S.; Ghosh, A.; Adler, H. J. P., Composite magnetic particles: 2. Encapsulation of iron oxide by surfactant-free emulsion polymerization. *Polymer* **2005,** *46* (13), 4596-4603.

46. Guo, J.; Yang, W.; Deng, Y.; Wang, C.; Fu, S., Organic-Dye-Coupled Magnetic Nanoparticles Encaged Inside Thermoresponsive PNIPAM Microcapsules. *Small* **2005,** *1* (7), 737-743.

47. Hickey, R. J.; Haynes, A. S.; Kikkawa, J. M.; Park, S.-J., Controlling the Self-Assembly Structure of Magnetic Nanoparticles and Amphiphilic Block-Copolymers: From Micelles to Vesicles. *J. Am. Chem. Soc.* **2011,** *133* (5), 1517-1525.

48. Zhang, F.; Smolen, J. A.; Zhang, S.; Li, R.; Shah, P. N.; Cho, S.; Wang, H.; Raymond, J. E.; Cannon, C. L.; Wooley, K. L., Degradable polyphosphoester-based silver-loaded nanoparticles as therapeutics for bacterial lung infections. *Nanoscale* **2015,** *7* (6), 2265-2270.

49. Lim, Y. H.; Tiemann, K. M.; Heo, G. S.; Wagers, P. O.; Rezenom, Y. H.; Zhang, S.; Zhang, F.; Youngs, W. J.; Hunstad, D. A.; Wooley, K. L., Preparation and in vitro antimicrobial activity of silver-bearing degradable polymeric nanoparticles of polyphosphoester-block-poly (L-lactide). *ACS nano* **2015,** *9* (2), 1995-2008.

50. Flores, J. A.; Pavía-Sanders, A.; Chen, Y.; Pochan, D. J.; Wooley, K. L., Recyclable Hybrid Inorganic/Organic Magnetically Active Networks for the Sequestration of Crude Oil from Aqueous Environments. *Chem. Mater.* **2015,** *27* (10), 3775-3782.

51. Pavía-Sanders, A.; Zhang, S.; Flores, J. A.; Sanders, J. E.; Raymond, J. E.; Wooley, K. L., Robust Magnetic/Polymer Hybrid Nanoparticles Designed for Crude Oil Entrapment and Recovery in Aqueous Environments. *ACS Nano* **2013,** *7* (9), 7552-7561.

52. Zhang, F.; Zhang, S.; Pollack, S. F.; Li, R.; Gonzalez, A. M.; Fan, J.; Zou, J.; Leininger, S. E.; Pavía-Sanders, A.; Johnson, R.; Nelson, L. D.; Raymond, J. E.; Elsabahy, M.; Hughes, D. M. P.; Lenox, M. W.; Gustafson, T. P.; Wooley, K. L., Improving Paclitaxel Delivery: In Vitro and In Vivo Characterization of PEGylated Polyphosphoester-Based Nanocarriers. *J. Am. Chem. Soc.* **2015,** *137* (5), 2056-2066.
53. Zhang, S.; Zou, J.; Zhang, F.; Elsabahy, M.; Felder, S. E.; Zhu, J.; Pochan, D. J.; Wooley, K. L., Rapid and Versatile Construction of Diverse and Functional Nanostructures Derived from a Polyphosphoester-Based Biomimetic Block Copolymer System. *J. Am. Chem. Soc.* **2012,** *134* (44), 18467-18474.
54. Kristufek, S. L.; Wacker, K. T.; Tsao, Y.-Y. T.; Su, L.; Wooley, K. L., Monomer design strategies to create natural product-based polymer materials. *Natural Product Reports* **2017,** *34* (4), 433-459.
55. Noel, A.; Borguet, Y. P.; Wooley, K. L., Self-Reporting Degradable Fluorescent Grafted Copolymer Micelles Derived from Biorenewable Resources. *ACS Macro Lett.* **2015,** *4* (6), 645-650.
56. Wacker, K. T.; Kristufek, S. L.; Lim, S.-M.; Kahn, S.; Wooley, K. L., Bio-based polycarbonates derived from the neolignan honokiol. *RSC advances* **2016,** *6* (85), 81672-81679.
57. Kristufek, S. L.; Yang, G.; Link, L. A.; Rohde, B. J.; Robertson, M. L.; Wooley, K. L., Synthesis, Characterization, and Cross‐Linking Strategy of a Quercetin‐Based Epoxidized Monomer as a Naturally‐Derived Replacement for BPA in Epoxy Resins. *ChemSusChem* **2016,** *9* (16), 2135-2142.

58. Link, L. A.; Lonnecker, A. T.; Hearon, K.; Maher, C. A.; Raymond, J. E.; Wooley, K. L., Photo-cross-linked poly (thioether-co-carbonate) networks derived from the natural product quinic acid. *ACS applied materials & interfaces* **2014,** *6* (20), 17370-17375.

59. Mikami, K.; Lonnecker, A. T.; Gustafson, T. P.; Zinnel, N. F.; Pai, P.-J.; Russell, D. H.; Wooley, K. L., Polycarbonates Derived from Glucose via an Organocatalytic Approach. *J. Am. Chem. Soc.* **2013,** *135* (18), 6826-6829.

60. Su, L.; Khan, S.; Fan, J.; Lin, Y.-N.; Wang, H.; Gustafson, T. P.; Zhang, F.; Wooley, K. L., Functional sugar-based polymers and nanostructures comprised of degradable poly (D-glucose carbonate) s. *Polym. Chem.* **2017,** *8* (10), 1699-1707.

61. Lonnecker, A. T.; Lim, Y. H.; Felder, S. E.; Besset, C. l. J.; Wooley, K. L., Four different regioisomeric polycarbonates derived from one natural product, D-glucose. *Macromolecules* **2016,** *49* (20), 7857-7867.

62. Felder, S. E.; Redding, M. J.; Noel, A.; Grayson, S. M.; Wooley, K. L., Organocatalyzed ROP of a glucopyranoside derived five-membered cyclic carbonate. *Macromolecules* **2018,** *51* (5), 1787-1797.

63. Lin, Y.-N.; Khan, S.; Song, Y.; Dong, M.; Shen, Y.; Tran, D. K.; Pang, C.; Zhang, F.; Wooley, K. L., A Tale of Drug-Carrier Optimization: Controlling Stimuli Sensitivity via Nanoparticle Hydrophobicity through Drug Loading. *Nano Lett.* **2020**.

64. Su, L.; Li, R.; Khan, S.; Clanton, R.; Zhang, F.; Lin, Y.-N.; Song, Y.; Wang, H.; Fan, J.; Hernandez, S.; Butters, A. S.; Akabani, G.; MacLoughlin, R.; Smolen, J.; Wooley, K. L., Chemical Design of Both a Glutathione-Sensitive Dimeric Drug Guest and a

Glucose-Derived Nanocarrier Host to Achieve Enhanced Osteosarcoma Lung Metastatic Anticancer Selectivity. *J. Am. Chem. Soc.* **2018,** *140* (4), 1438-1446.

65. Lin, Y.-N.; Su, L.; Smolen, J.; Li, R.; Song, Y.; Wang, H.; Dong, M.; Wooley, K. L., Co-assembly of sugar-based amphiphilic block polymers to achieve nanoparticles with tunable morphology, size, surface charge, and acid-responsive behavior. *Materials Chemistry Frontiers* **2018,** *2* (12), 2230-2238.
66. Song, Y.; Ji, X.; Dong, M.; Li, R.; Lin, Y.-N.; Wang, H.; Wooley, K. L., Advancing the development of highly-functionalizable glucose-based polycarbonates by tuning of the glass transition temperature. *J. Am. Chem. Soc.* **2018,** *140* (47), 16053-16057.
67. Su, L.; Heo, G. S.; Lin, Y.-N.; Dong, M.; Zhang, S.; Chen, Y.; Sun, G.; Wooley, K. L., Syntheses of triblock bottlebrush polymers through sequential ROMPs: Expanding the functionalities of molecular brushes. *J. Polym. Sci., Part A: Polym. Chem.* **2017,** *55* (18), 2966-2970.
68. Cheng, C.; Khoshdel, E.; Wooley, K. L., ATRP from a Norbornenyl-Functionalized Initiator: Balancing of Complementary Reactivity for the Preparation of α-Norbornenyl Macromonomers/ω-Haloalkyl Macroinitiators. *Macromolecules* **2005,** *38* (23), 9455-9465.
69. Xia, Y.; Kornfield, J. A.; Grubbs, R. H., Efficient Synthesis of Narrowly Dispersed Brush Polymers via Living Ring-Opening Metathesis Polymerization of Macromonomers. *Macromolecules* **2009,** *42* (11), 3761-3766.

70. Gao, H.; Matyjaszewski, K., Synthesis of Molecular Brushes by "Grafting onto" Method: Combination of ATRP and Click Reactions. *J. Am. Chem. Soc.* **2007,** *129* (20), 6633-6639.

71. Fenyves, R.; Schmutz, M.; Horner, I. J.; Bright, F. V.; Rzayev, J., Aqueous Self-Assembly of Giant Bottlebrush Block Copolymer Surfactants as Shape-Tunable Building Blocks. *J. Am. Chem. Soc.* **2014,** *136* (21), 7762-7770.

72. Neiser, M. W.; Muth, S.; Kolb, U.; Harris, J. R.; Okuda, J.; Schmidt, M., Micelle Formation from Amphiphilic "Cylindrical Brush"—Coil Block Copolymers Prepared by Metallocene Catalysis. *Angew. Chem. Int. Ed.* **2004,** *43* (24), 3192-3195.

73. Li, Z.; Ma, J.; Lee, N. S.; Wooley, K. L., Dynamic Cylindrical Assembly of Triblock Copolymers by a Hierarchical Process of Covalent and Supramolecular Interactions. *J. Am. Chem. Soc.* **2011,** *133* (5), 1228-1231.

74. Li, Z.; Ma, J.; Cheng, C.; Zhang, K.; Wooley, K. L., Synthesis of Hetero-Grafted Amphiphilic Diblock Molecular Brushes and Their Self-Assembly in Aqueous Medium. *Macromolecules* **2010,** *43* (3), 1182-1184.

75. Su, L.; Khan, S.; Fan, J.; Lin, Y.-N.; Wang, H.; Gustafson, T. P.; Zhang, F.; Wooley, K. L., Functional Sugar-Based Polymers and Nanostructures Comprised of Degradable Poly(D-glucose carbonate)s. *Polym. Chem.* **2017,** *8*, 1699-1707.

76. Choi, T.-L.; Grubbs, R. H., Controlled Living Ring-Opening-Metathesis Polymerization by a Fast-Initiating Ruthenium Catalyst. *Angew. Chem. Int. Ed.* **2003,** *42*, 1743-1746.

77. O'Reilly, R. K.; Hawker, C. J.; Wooley, K. L., Cross-Linked Block Copolymer Micelles: Functional Nanostructures of Great Potential and Versatility. *Chem. Soc. Rev.* **2006,** *35*, 1068-1083.

78. Wooley, K. L., Shell Crosslinked Polymer Assemblies: Nanoscale Constructs Inspired from Biological Systems. *J. Polym. Sci., Part A: Polym. Chem.* **2000,** *38*, 1397-1407.

79. Blanazs, A.; Armes, S. P.; Ryan, A. J., Self-Assembled Block Copolymer Aggregates: From Micelles to Vesicles and their Biological Applications. *Macromol. Rapid Commun.* **2009,** *30*, 267-277.

80. Moughton, A. O.; O'Reilly, R. K., Thermally Induced Micelle to Vesicle Morphology Transition for A Charged Chain End Diblock Copolymer. *Chem. Commun.* **2010,** *46*, 1091-1093.

81. Ghoroghchian, P. P.; Li, G.; Levine, D. H.; Davis, K. P.; Bates, F. S.; Hammer, D. A.; Therien, M. J., Bioresorbable Vesicles Formed through Spontaneous Self-Assembly of Amphiphilic Poly(ethylene oxide)-*block*-Polycaprolactone. *Macromolecules* **2006,** *39*, 1673-1675.

82. Zhou, J.; Liu, J.; Cheng, C. J.; Patel, T. R.; Weller, C. E.; Piepmeier, J. M.; Jiang, Z.; Saltzman, W. M., Biodegradable Poly(amine-*co*-ester) Terpolymers for Targeted Gene Delivery. *Nat. Mater.* **2011,** *11*, 82-90.

83. Fan, J.; Zou, J.; He, X.; Zhang, F.; Zhang, S.; Raymond, J. E.; Wooley, K. L., Tunable Mechano-Responsive Organogels by Ring-Opening Copolymerizations of *N*-carboxyanhydrides. *Chem. Sci.* **2014,** *5*, 141-150.

84. Lu, H.; Wang, J.; Song, Z.; Yin, L.; Zhang, Y.; Tang, H.; Tu, C.; Lin, Y.; Cheng, J., Recent Advances in Amino Acid *N*-Carboxyanhydrides and Synthetic Polypeptides: Chemistry, Self-Assembly and Biological Applications. *Chem. Commun.* **2014,** *50*, 139-155.

85. Zhang, F.; Zhang, S.; Pollack, S. F.; Li, R.; Gonzalez, A. M.; Fan, J.; Zou, J.; Leininger, S. E.; Pavía-Sanders, A.; Johnson, R.; Nelson, L. D.; Raymond, J. E.; Elsabahy, M.; Hughes, D. M. P.; Lenox, M. W.; Gustafson, T. P.; Wooley, K. L., Improving Paclitaxel Delivery: *In Vitro* and *In Vivo* Characterization of PEGylated Polyphosphoester-Based Nanocarriers. *J. Am. Chem. Soc.* **2015,** *137*, 2056-2066.

86. Song, Y.; Chen, Y.; Su, L.; Li, R.; Letteri, R. A.; Wooley, K. L., Crystallization-Driven Assembly of Fully Degradable, Natural Product-Based Poly(L-lactide)-*block*-Poly(α-D-glucose carbonate)s in Aqueous Solution. *Polymer* **2017,** *122*, 270-279.

87. Osumi, S.; Felder, S. E.; Wang, H.; Lin, Y.-N.; Dong, M.; Wooley, K. L., Construction of Nanostructures in Aqueous Solution from Amphiphilic Glucose-Derived Polycarbonates. *J. Polym. Sci., Part A: Polym. Chem.* **2019,** *57*, 432-440.

88. Lin, Y.-N.; Su, L.; Smolen, J.; Li, R.; Song, Y.; Wang, H.; Dong, M.; Wooley, K. L., Co-Assembly of Sugar-Based Amphiphilic Block Polymers to Achieve Nanoparticles with Tunable Morphology, Size, Surface Charge, and Acid-Responsive Behavior. *Mater. Chem. Front.* **2018,** *2*, 2230-2238.

89. Nasongkla, N.; Chen, B.; Macaraeg, N.; Fox, M. E.; Fréchet, J. M. J.; Szoka, F. C., Dependence of Pharmacokinetics and Biodistribution on Polymer Architecture: Effect of Cyclic *versus* Linear Polymers. *J. Am. Chem. Soc.* **2009,** *131*, 3842-3843.

90. Voit, B. I.; Lederer, A., Hyperbranched and Highly Branched Polymer Architectures-Synthetic Strategies and Major Characterization Aspects. *Chem. Rev.* **2009,** *109*, 5924-5973.
91. Du, J.-Z.; Tang, L.-Y.; Song, W.-J.; Shi, Y.; Wang, J., Evaluation of Polymeric Micelles from Brush Polymer with Poly(ε-caprolactone)-*b*-Poly(ethylene glycol) Side Chains as Drug Carrier. *Biomacromolecules* **2009,** *10*, 2169-2174.
92. Lu, S.; Seong, H. G.; Yen-Nan, L.; Mei, D.; Shiyi, Z.; Yingchao, C.; Guorong, S.; L., W. K., Syntheses of Triblock Bottlebrush Polymers Through Sequential ROMPs: Expanding the Functionalities of Molecular Brushes. *J. Polym. Sci., Part A: Polym. Chem.* **2017,** *55*, 2966-2970.
93. Müllner, M.; Müller, A. H. E., Cylindrical Polymer Brushes – Anisotropic Building Blocks, Unimolecular Templates and Particulate Nanocarriers. *Polymer* **2016,** *98*, 389-401.
94. Verduzco, R.; Li, X.; Pesek, S. L.; Stein, G. E., Structure, Function, Self-Assembly, and Applications of Bottlebrush Copolymers. *Chem. Soc. Rev.* **2015,** *44*, 2405-2420.
95. Jonikaite-Svegzdiene, J.; Kudresova, A.; Paukstis, S.; Skapas, M.; Makuska, R., Synthesis and Self-Assembly of Polystyrene-Based Diblock and Triblock Coil-Brush Copolymers. *Polym. Chem.* **2017,** *8*, 5621-5632.
96. Li, C.; Ge, Z.; Fang, J.; Liu, S., Synthesis and Self-Assembly of Coil−Rod Double Hydrophilic Diblock Copolymer with Dually Responsive Asymmetric Centipede-Shaped Polymer Brush as the Rod Segment. *Macromolecules* **2009,** *42*, 2916-2924.

97. Wang, W.; Liu, R.; Li, Z.; Meng, C.; Wu, Q.; Zhu, F., Synthesis and Self-Assembly of New Double-Crystalline Amphiphilic Polyethylene-*block*-Poly[oligo(ethylene glycol) Methyl Ether Methacrylate] Coil-Brush Diblock Copolymer. *Macromol. Chem. Phys.* **2010,** *211*, 1452-1459.

98. Sun, R.; Wang, G.; Liu, C.; Huang, J., Preparation of Comb-Like Copolymers with Amphiphilic Poly(ethylene oxide)-*b*-Polystyrene Graft Chains by Combination of "Graft From" and "Graft Onto" Strategies. *J. Polym. Sci., Part A: Polym. Chem.* **2009,** *47*, 1930-1938.

99. Feng, C.; Shen, Z.; Li, Y.; Gu, L.; Zhang, Y.; Lu, G.; Huang, X., PNIPAM-*b*-(PEA-*g*-PDMAEA) Double-Hydrophilic Graft Copolymer: Synthesis and Its Application for Preparation of Gold Nanoparticles in Aqueous Media. *J. Polym. Sci., Part A: Polym. Chem.* **2009,** *47,* 1811-1824.

100. Tao, Y.; Ma, B.; Segalman, R. A., Self-Assembly of Rod−Coil Block Copolymers and Their Application in Electroluminescent Devices. *Macromolecules* **2008,** *41*, 7152-7159.

101. Ishizu, K.; Hatoyama, N.; Uchida, S., Architecture of Rod–Brush Block Copolymers Synthesized by A Combination of Coordination Polymerization and Atom Transfer Radical Polymerization. *J. Appl. Polym. Sci.* **2008,** *108,* 3346-3352.

102. Bernaerts, K. V.; Fustin, C.-A.; Bomal-D'Haese, C.; Gohy, J.-F.; Martins, J. C.; Du Prez, F. E., Advanced Polymer Architectures with Stimuli-Responsive Properties Starting from Inimers. *Macromolecules* **2008,** *41,* 2593-2606.

103. Du, J.-Z.; Chen, D.-P.; Wang, Y.-C.; Xiao, C.-S.; Lu, Y.-J.; Wang, J.; Zhang, G.-Z., Synthesis and Micellization of Amphiphilic Brush−Coil Block Copolymer Based on Poly(ε-caprolactone) and PEGylated Polyphosphoester. *Biomacromolecules* **2006,** *7*, 1898-1903.

104. Olsen, B. D.; Segalman, R. A., Structure and Thermodynamics of Weakly Segregated Rod−Coil Block Copolymers. *Macromolecules* **2005,** *38*, 10127-10137.

105. Fu, G. D.; Phua, S. J.; Kang, E. T.; Neoh, K. G., Tadpole-Shaped Amphiphilic Block−Graft Copolymers Prepared *via* Consecutive Atom Transfer Radical Polymerizations. *Macromolecules* **2005,** *38*, 2612-2619.

106. Banquy, X.; Burdyńska, J.; Lee, D. W.; Matyjaszewski, K.; Israelachvili, J., Bioinspired Bottle-Brush Polymer Exhibits Low Friction and Amontons-Like Behavior. *J. Am. Chem. Soc.* **2014,** *136*, 6199-6202.

107. Rodríguez-Hernández, J.; Chécot, F.; Gnanou, Y.; Lecommandoux, S., Toward ‘Smart’ Nano-Objects by Self-Assembly of Block Copolymers in Solution. *Prog. Polym. Sci.* **2005,** *30*, 691-724.

108. Hadjichristidis, N.; Iatrou, H.; Pitsikalis, M.; Pispas, S.; Avgeropoulos, A., Linear and Non-Linear Triblock Terpolymers. Synthesis, Self-Assembly in Selective Solvents and in Bulk. *Prog. Polym. Sci.* **2005,** *30*, 725-782.

109. Riess, G., Micellization of Block Copolymers. *Prog. Polym. Sci.* **2003,** *28*, 1107-1170.

110. Ruokolainen, J.; Saariaho, M.; Ikkala, O.; ten Brinke, G.; Thomas, E. L.; Torkkeli, M.; Serimaa, R., Supramolecular Routes to Hierarchical Structures: Comb-Coil

Diblock Copolymers Organized with Two Length Scales. *Macromolecules* **1999,** *32*, 1152-1158.

111. Bougard, F.; Giacomelli, C.; Mespouille, L.; Borsali, R.; Dubois, P.; Lazzaroni, R., Influence of the Macromolecular Architecture on the Self-Assembly of Amphiphilic Copolymers Based on Poly(N,N-dimethylamino-2-ethyl methacrylate) and Poly(ε-caprolactone). *Langmuir* **2008,** *24*, 8272-8279.
112. Xu, X.; Jia, Z.; Sun, R.; Huang, J., Synthesis of Well-Defined, Brush-Type, Amphiphilic [Poly(styrene-*co*-2-hydroxyethyl methacrylate)-*graft*-Poly(ε-caprolactone)]-*b*-Poly(ethylene oxide)-*b*-[Poly(styrene-*co*-2-hydroxyethyl methacrylate)-*graft*-Poly(ε-caprolactone)] and Its Aggregation Behavior in Aqueous Media. *J. Polym. Sci., Part A: Polym. Chem.* **2006,** *44*, 4396-4408.
113. Qi, H.; Zhong, C., Density Functional Theory Studies on the Microphase Separation of Amphiphilic Comb Copolymers in a Selective Solvent. *J. Phys. Chem. B* **2008,** *112*, 10841-10847.
114. Khelfallah, N.; Gunari, N.; Fischer, K.; Gkogkas, G.; Hadjichristidis, N.; Schmidt, M., Micelles Formed by Cylindrical Brush-Coil Block Copolymers. *Macromol. Rapid Commun.* **2005,** *26*, 1693-1697.
115. Zamurovic, M.; Christodoulou, S.; Vazaios, A.; Iatrou, E.; Pitsikalis, M.; Hadjichristidis, N., Micellization Behavior of Complex Comblike Block Copolymer Architectures. *Macromolecules* **2007,** *40*, 5835-5849.

116. Yi, Z.; Liu, X.; Jiao, Q.; Chen, E.; Chen, Y.; Xi, F., Synthesis, Characterization, and Self-Assembly of Comb-Dendronized Amphiphilic Block Copolymers. *J. Polym. Sci., Part A: Polym. Chem.* **2008,** *46*, 4205-4217.
117. Cai, C.; Zhu, W.; Chen, T.; Lin, J.; Tian, X., Synthesis and Self-Assembly Behavior of Amphiphilic Polypeptide-Based Brush-Coil Block Copolymers. *J. Polym. Sci., Part A: Polym. Chem.* **2009,** *47*, 5967-5978.
118. Zhang, Q.; Lin, J.; Wang, L.; Xu, Z., Theoretical Modeling and Simulations of Self-Assembly of Copolymers in Solution. *Prog. Polym. Sci.* **2017,** *75*, 1-30.
119. Percec, V.; Wilson, D. A.; Leowanawat, P.; Wilson, C. J.; Hughes, A. D.; Kaucher, M. S.; Hammer, D. A.; Levine, D. H.; Kim, A. J.; Bates, F. S., Self-Assembly of Janus Dendrimers into Uniform Dendrimersomes and Other Complex Architectures. *Science* **2010,** *328*, 1009-1014.
120. Zhuang, Z.; Zhu, X.; Cai, C.; Lin, J.; Wang, L., Self-Assembly of a Mixture System Containing Polypeptide Graft and Block Copolymers: Experimental Studies and Self-Consistent Field Theory Simulations. *J. Phys. Chem. B* **2012,** *116*, 10125-10134.
121. Li, Y.; Jiang, T.; Lin, S.; Lin, J.; Cai, C.; Zhu, X., Hierarchical Nanostructures Self-Assembled from a Mixture System Containing Rod-Coil Block Copolymers and Rigid Homopolymers. *Sci. Rep.* **2015,** *5*, 10137.
122. Cai, C.; Li, Y.; Lin, J.; Wang, L.; Lin, S.; Wang, X. S.; Jiang, T., Simulation‐Assisted Self‐Assembly of Multicomponent Polymers into Hierarchical Assemblies with Varied Morphologies. *Angew. Chem.* **2013,** *125*, 7886-7890.

123. Wu, W.-C.; Tian, Y.; Chen, C.-Y.; Lee, C.-S.; Sheng, Y.-J.; Chen, W.-C.; Alex, K.-Y. J., Theoretical and Experimental Studies on the Surface Structures of Conjugated Rod−Coil Block Copolymer Brushes. *Langmuir* **2007,** *23*, 2805-2814.

124. Li, N. K.; Fuss, W. H.; Tang, L.; Gu, R.; Chilkoti, A.; Zauscher, S.; Yingling, Y. G., Prediction of Solvent-Induced Morphological Changes of Polyelectrolyte Diblock Copolymer Micelles. *Soft Matter* **2015,** *11*, 8236-8245.

125. Gu, W.; Huh, J.; Hong, S. W.; Sveinbjornsson, B. R.; Park, C.; Grubbs, R. H.; Russell, T. P., Self-Assembly of Symmetric Brush Diblock Copolymers. *ACS Nano* **2013,** *7*, 2551-2558.

126. Zhulina, E. B.; Adam, M.; LaRue, I.; Sheiko, S. S.; Rubinstein, M., Diblock Copolymer Micelles in a Dilute Solution. *Macromolecules* **2005,** *38*, 5330-5351.

127. Zhulina, E.; Borisov, O., Theory of Block Polymer Micelles: Recent Advances and Current Challenges. *Macromolecules* **2012,** *45*, 4429-4440.

128. Dalsin, S. J.; Rions-Maehren, T. G.; Beam, M. D.; Bates, F. S.; Hillmyer, M. A.; Matsen, M. W., Bottlebrush Block Polymers: Quantitative Theory and Experiments. *ACS Nano* **2015,** *9*, 12233-12245.

129. Alaboalirat, M.; Qi, L.; Arrington, K. J.; Qian, S.; Keum, J. K.; Mei, H.; Littrell, K. C.; Sumpter, B. G.; Carrillo, J.-M. Y.; Verduzco, R.; Matson, J. B., Amphiphilic Bottlebrush Block Copolymers: Analysis of Aqueous Self-Assembly by Small-Angle Neutron Scattering and Surface Tension Measurements. *Macromolecules* **2019,** *52*, 465-476.

130. Ianiro, A.; Wu, H.; van Rijt, M. M. J.; Vena, M. P.; Keizer, A. D. A.; Esteves, A. C. C.; Tuinier, R.; Friedrich, H.; Sommerdijk, N. A. J. M.; Patterson, J. P., Liquid–Liquid Phase Separation During Amphiphilic Self-Assembly. *Nat. Chem.* **2019,** *11*, 320-328.
131. Wang, R.; Jiang, Z.; Yang, H.; Xue, G., Side Chain Effect on the Self-Assembly of Coil-Comb Copolymer by Self-Consistent Field Theory in Two Dimensions. *Polymer* **2013,** *54*, 7080-7087.
132. Nap, R. J.; Ten Brinke, G., Ordering at Two Length Scales in Comb− Coil Diblock Copolymers Consisting of Only Two Different Monomers. *Macromolecules* **2002,** *35*, 952-959.
133. Wang, L.; Lin, J.; Zhang, L., Hierarchically Ordered Microstructures Self-Assembled from Comb−Coil Block Copolymers. *Langmuir* **2009,** *25*, 4735-4742.
134. Wang, L.; Lin, J.; Zhang, L., Hierarchically Ordered Microstructures Self-Assembled from A (BC) n Multiblock Copolymers. *Macromolecules* **2010,** *43*, 1602-1609.
135. Vasilevskaya, V.; Gusev, L.; Khokhlov, A.; Ikkala, O.; Ten Brinke, G., Domains in Melts of Comb−Coil Diblock Copolymers: Superstrong Segregation Regime. *Macromolecules* **2001,** *34*, 5019-5022.
136. Jiang, Z.; Qian, Z.; Yang, H.; Wang, R., Disorder to Order Transition and Ordered Morphology of Coil-Comb Block Copolymer by Self-Consistent Field Theory. *Nanoscale Res. Lett.* **2015,** *10*, 328.

137. Huang, C. I.; Lin, Y. C., Hierarchical Structure‐within‐Structure Morphologies in A‐*block*‐(B‐*graft*‐C) Molecules. *Macromol. Rapid Commun.* **2007,** *28,* 1634-1639.
138. Huang, C.-I., Self-Assembling of Block Copolymers Involving Competing Length Scales. *React. Funct. Polym.* **2009,** *69,* 530-538.
139. Wang, J.; Guo, K.; An, L.; Muller, M.; Wang, Z.-G., Micelles of Coil-Comb Block Copolymers in Selective Solvents: Competition of Length Scales. *Macromolecules* **2010,** *43,* 2037-2041.
140. Cheng, L.; Cao, D., Effect of Tail Architecture on Self-Assembly of Amphiphiles for Polymeric Micelles. *Langmuir* **2009,** *25,* 2749-2756.
141. Wood, K. C.; Little, S. R.; Langer, R.; Hammond, P. T., A Family of Hierarchically Self‐Assembling Linear‐Dendritic Hybrid Polymers for Highly Efficient Targeted Gene Delivery. *Angew. Chem. Int. Ed.* **2005,** *44,* 6704-6708.
142. Lin, Y.-L.; Chang, H.-Y.; Sheng, Y.-J.; Tsao, H.-K., Photoresponsive Polymersomes Formed by Amphiphilic Linear–Dendritic Block Copolymers: Generation-Dependent Aggregation Behavior. *Macromolecules* **2012,** *45,* 7143-7156.
143. Liu, Y.; Zhang, Y.; Wang, Z.; Wang, J.; Wei, K.; Chen, G.; Jiang, M., Building Nanowires from Micelles: Hierarchical Self-Assembly of Alternating Amphiphilic Glycopolypeptide Brushes with Pendants of High-Mannose Glycodendron and Oligophenylalanine. *J. Am. Chem. Soc.* **2016,** *138,* 12387-12394.
144. Yu, W.; Inam, M.; Jones, J. R.; Dove, A. P.; O'Reilly, R. K., Understanding the CDSA of Poly(lactide) Containing Triblock Copolymers. *Polym. Chem.* **2017,** *8,* 5504-5512.

145. Israelachvili, J. N.; Mitchell, D. J.; Ninham, B. W., Theory of Self-Assembly of Hydrocarbon Amphiphiles into Micelles and Bilayers. *J. Chem. Soc. Faraday Trans.* **1976,** *72*, 1525-1568.
146. Samarajeewa, S.; Shrestha, R.; Li, Y.; Wooley, K. L., Degradability of Poly(Lactic Acid)-Containing Nanoparticles: Enzymatic Access through a Cross-Linked Shell Barrier. *J. Am. Chem. Soc.* **2012,** *134*, 1235-1242.
147. Gregory, G. L.; Jenisch, L. M.; Charles, B.; Kociok-Köhn, G.; Buchard, A., Polymers from Sugars and CO_2: Synthesis and Polymerization of a D-Mannose-Based Cyclic Carbonate. *Macromolecules* **2016,** *49*, 7165-7169.
148. Ceperley, D.; Kalos, M.; Lebowitz, J. L., Computer Simulation of the Dynamics of a Single Polymer Chain. *Phys. Rev. Lett.* **1978,** *41*, 313-316.
149. Grest, G. S.; Kremer, K., Molecular Dynamics Simulation for Polymers in the Presence of a Heat Bath. *Phys. Rev. A* **1986,** *33*, 3628-3631.
150. Jones, J. E., On the Determination of Molecular Fields.—I. From the Variation of the Viscosity of a Gas with Temperature. *Proc. R. Soc. Lond. A* **1924,** *106*, 441-462.
151. Weeks, J. D.; Chandler, D.; Andersen, H. C., Role of Repulsive Forces in Determining the Equilibrium Structure of Simple Liquids. *J. Chem. Phys.* **1971,** *54*, 5237-5247.
152. Plimpton, S., Fast Parallel Algorithms for Short-Range Molecular Dynamics. *J. Comput. Phys.* **1995,** *117*, 1-19.

153. Beltran-Villegas, D. J.; Jayaraman, A., Assembly of Amphiphilic Block Copolymers and Nanoparticles in Solution: Coarse-Grained Molecular Simulation Study. *J. Chem. Eng. Data* **2018,** *63*, 2351-2367.

154. Lyubimov, I.; Beltran-Villegas, D. J.; Jayaraman, A., PRISM Theory Study of Amphiphilic Block Copolymer Solutions with Varying Copolymer Sequence and Composition. *Macromolecules* **2017,** *50*, 7419-7431.

155. Humphrey, W.; Dalke, A.; Schulten, K., VMD: Visual Molecular Dynamics. *J. Mol. Graph.* **1996,** *14*, 33-38.

156. Lee, B.; Richards, F. M., The Interpretation of Protein Structures: Estimation of Static Accessibility. *J. Mol. Biol.* **1971,** *55*, 379-IN4.

157. Shrake, A.; Rupley, J., Environment and Exposure to Solvent of Protein Atoms. Lysozyme and Insulin. *J. Mol. Biol.* **1973,** *79*, 351-371.

158. Lin, B.; Martin, T. B.; Jayaraman, A., Decreasing Polymer Flexibility Improves Wetting and Dispersion of Polymer-Grafted Particles in a Chemically Identical Polymer Matrix. *ACS Macro Lett.* **2014,** *3*, 628-632.

159. Tanner, P.; Baumann, P.; Enea, R.; Onaca, O.; Palivan, C.; Meier, W., Polymeric Vesicles: From Drug Carriers to Nanoreactors and Artificial Organelles. *Acc. Chem. Res.* **2011,** *44*, 1039-1049.

160. Geng, Y.; Dalhaimer, P.; Cai, S.; Tsai, R.; Tewari, M.; Minko, T.; Discher, D. E., Shape Effects of Filaments *versus* Spherical Particles in Flow and Drug Delivery. *Nat. Nanotechnol.* **2007,** *2*, 249.

161. Gratton, S. E. A.; Ropp, P. A.; Pohlhaus, P. D.; Luft, J. C.; Madden, V. J.; Napier, M. E.; DeSimone, J. M., The Effect of Particle Design on Cellular Internalization Pathways. *Proc. Natl. Acad. Sci. U.S.A.* **2008,** *105*, 11613-11618.

162. Albanese, A.; Tang, P. S.; Chan, W. C. W., The Effect of Nanoparticle Size, Shape, and Surface Chemistry on Biological Systems. *Annu. Rev. Biomed. Eng.* **2012,** *14*, 1-16.

163. Unsal, H.; Onbulak, S.; Calik, F.; Er-Rafik, M.; Schmutz, M.; Sanyal, A.; Rzayev, J., Interplay Between Molecular Packing, Drug Loading, and Core Cross-Linking in Bottlebrush Copolymer Micelles. *Macromolecules* **2017,** *50*, 1342-1352.

164. Hillmyer, M. A., The Promise of Plastics from Plants. *Science* **2017,** *358*, 868-870.

165. Zhu, Y.; Romain, C.; Williams, C. K., Sustainable Polymers from Renewable Resources. *Nature* **2016,** *540*, 354-362.

166. Miller, S. A., Sustainable Polymers: Opportunities for the Next Decade. *ACS Macro Lett.* **2013,** *2*, 550-554.

167. De Hoe, G. X.; Zumstein, M. T.; Tiegs, B. J.; Brutman, J. P.; McNeill, K.; Sander, M.; Coates, G. W.; Hillmyer, M. A., Sustainable Polyester Elastomers from Lactones: Synthesis, Properties, and Enzymatic Hydrolyzability. *J. Am. Chem. Soc.* **2018,** *140*, 963-973.

168. Song, Y.; Ji, X.; Dong, M.; Li, R.; Lin, Y.-N.; Wang, H.; Wooley, K. L., Advancing the Development of Highly-Functionalizable Glucose-Based Polycarbonates by Tuning of the Glass Transition Temperature. *J. Am. Chem. Soc.* **2018,** *140*, 16053-16057.

169. Wang, H.; Dong, M.; Khan, S.; Su, L.; Li, R.; Song, Y.; Lin, Y.-N.; Kang, N.; Komatsu, C. H.; Elsabahy, M.; Wooley, K. L., Acid-Triggered Polymer Backbone Degradation and Disassembly to Achieve Release of Camptothecin from Functional Polyphosphoramidate Nanoparticles. *ACS Macro Lett.* **2018,** *7*, 783-788.
170. Kingston, P. F., Long-term Environmental Impact of Oil Spills. *Spill Sci. Technol. Bull.* **2002,** *7* (1), 53-61.
171. Patin, S. A., *Environmental Impact of the Offshore Oil and Gas Industry*. JSTOR: 1999; Vol. 1.
172. Gordon, G.; Stavi, I.; Shavit, U.; Rosenzweig, R., Oil spill effects on soil hydrophobicity and related properties in a hyper-arid region. *Geoderma* **2018,** *312*, 114-120.
173. Fingas, M., *The Basics of Oil Spill Cleanup*. CRC press: 2012.
174. Hoff, R. Z., Bioremediation: an Overview Of Its Development and Use for Oil Spill Cleanup. *Mar. Pollut. Bull.* **1993,** *26* (9), 476-481.
175. Response., U. S. E. P. A. O. o. E. a. R., *Understanding Oil Spills And Oil Spill Response*. 1999.
176. Lessard, R. R.; DeMarco, G., The Significance of Oil Spill Dispersants. *Spill Sci. Technol. Bull.* **2000,** *6* (1), 59-68.
177. Bayat, A.; Aghamiri, S. F.; Moheb, A.; Vakili-Nezhaad, G. R., Oil Spill Cleanup from Sea Water by Sorbent Materials. *Chem. Eng. Technol.* **2005,** *28* (12), 1525-1528.
178. Canevari, G., Oil Slick Dispersant and Method. *United States Patent* **1974**, No. 3,793,218.

179. Fendall, L. S.; Sewell, M. A., Contributing to marine pollution by washing your face: microplastics in facial cleansers. *Mar. Pollut. Bull.* **2009,** *58* (8), 1225-1228.

180. Eriksen, M.; Lebreton, L. C.; Carson, H. S.; Thiel, M.; Moore, C. J.; Borerro, J. C.; Galgani, F.; Ryan, P. G.; Reisser, J., Plastic pollution in the world's oceans: more than 5 trillion plastic pieces weighing over 250,000 tons afloat at sea. *PloS one* **2014,** *9* (12), e111913.

181. Windsor, F. M.; Durance, I.; Horton, A. A.; Thompson, R. C.; Tyler, C. R.; Ormerod, S. J., A catchment ‐ scale perspective of plastic pollution. *Global Change Biol.* **2019,** *25* (4), 1207-1221.

182. Van Cauwenberghe, L.; Vanreusel, A.; Mees, J.; Janssen, C. R., Microplastic pollution in deep-sea sediments. *Environ. Pollut.* **2013,** *182,* 495-499.

183. Andrady, A. L., Microplastics in the Marine Environment. *Mar. Pollut. Bull.* **2011,** *62* (8), 1596-1605.

184. Ng, K.; Obbard, J., Prevalence of Microplastics in Singapore’s Coastal Marine Environment. *Mar. Pollut. Bull.* **2006,** *52* (7), 761-767.

185. Silva, R. d. C. F.; Almeida, D. G.; Rufino, R. D.; Luna, J. M.; Santos, V. A.; Sarubbo, L. A., Applications of Biosurfactants in the Petroleum Industry and the Remediation of Oil Spills. *Int. J. Mol. Sci.* **2014,** *15* (7), 12523-12542.

186. Cole, M.; Lindeque, P.; Fileman, E.; Halsband, C.; Goodhead, R.; Moger, J.; Galloway, T. S., Microplastic Ingestion by Zooplankton. *Environ. Sci. Technol.* **2013,** *47* (12), 6646-6655.

187. Nguyen, H.; Stuchtey, M.; Zils, M., Remaking the industrial economy. *McKinsey Quarterly* **2014,** *1*, 46-63.

188. Huysman, S.; De Schaepmeester, J.; Ragaert, K.; Dewulf, J.; De Meester, S., Performance indicators for a circular economy: A case study on post-industrial plastic waste. *Resour., Conserv. Recycl.* **2017,** *120*, 46-54.

189. Van Eygen, E.; Laner, D.; Fellner, J., Circular economy of plastic packaging: Current practice and perspectives in Austria. *Waste Manage. (Oxford)* **2018,** *72*, 55-64.

190. Stahel, W. R., The circular economy. *Nature News* **2016,** *531* (7595), 435.

191. Choi, H. M.; Cloud, R. M., Natural Sorbents in Oil Spill Cleanup. *Environ. Sci. Technol.* **1992,** *26* (4), 772-776.

192. Zhu, H.; Qiu, S.; Jiang, W.; Wu, D.; Zhang, C., Evaluation of Electrospun Polyvinyl Chloride/Polystyrene Fibers as Sorbent Materials for Oil Spill Cleanup. *Environ. Sci. Technol.* **2011,** *45* (10), 4527-4531.

193. Ge, J.; Zhao, H. Y.; Zhu, H. W.; Huang, J.; Shi, L. A.; Yu, S. H., Advanced Sorbents for Oil-Spill Cleanup: Recent Advances and Future Perspectives. *Adv. Mater.* **2016,** *28* (47), 10459-10490.

194. Xiao, L.; Ling, Y.; Alsbaiee, A.; Li, C.; Helbling, D. E.; Dichtel, W. R., β-Cyclodextrin Polymer Network Sequesters Perfluorooctanoic Acid at Environmentally Relevant Concentrations. *J. Am. Chem. Soc.* **2017,** *139* (23), 7689-7692.

195. Calcagnile, P.; Fragouli, D.; Bayer, I. S.; Anyfantis, G. C.; Martiradonna, L.; Cozzoli, P. D.; Cingolani, R.; Athanassiou, A., Magnetically Driven Floating Foams for the Removal of Oil Contaminants from Water. *ACS Nano* **2012,** *6* (6), 5413-5419.
196. Pyun, J., Nanocomposite Materials from Functional Polymers and Magnetic Colloids. *Polym. Rev.* **2007,** *47* (2), 231-263.
197. Gui, X.; Zeng, Z.; Lin, Z.; Gan, Q.; Xiang, R.; Zhu, Y.; Cao, A.; Tang, Z., Magnetic and Highly Recyclable Macroporous Carbon Nanotubes for Spilled Oil Sorption and Separation. *ACS Appl. Mater. Interfaces* **2013,** *5* (12), 5845-5850.
198. Ge, B.; Zhu, X.; Li, Y.; Men, X.; Li, P.; Zhang, Z., Versatile Fabrication of Magnetic Superhydrophobic Foams and Application for Oil–Water Separation. *Colloids Surf., A* **2015,** *482*, 687-692.
199. Yoon, K. Y.; Li, Z.; Neilson, B. M.; Lee, W.; Huh, C.; Bryant, S. L.; Bielawski, C. W.; Johnston, K. P., Effect of Adsorbed Amphiphilic Copolymers on the Interfacial Activity of Superparamagnetic Nanoclusters and the Emulsification of Oil in Water. *Macromolecules* **2012,** *45* (12), 5157-5166.
200. Chen, N.; Pan, Q., Versatile Fabrication of Ultralight Magnetic Foams and Application for Oil–Water Separation. *ACS nano* **2013,** *7* (8), 6875-6883.
201. Lehr, W.; Cekirge, H.; Fraga, R.; Belen, M., Empirical Studies of the Spreading of Oil Spills. *Oil Petrochem. Pollut.* **1984,** *2* (1), 7-11.
202. Fay, J. A., The Spread of Oil Slicks on a Calm Sea. In *Oil on the Sea*, Springer: 1969; pp 53-63.

203. Fingas, M.; Brown, C., Review of Oil Spill Remote Sensing. *Mar. Pollut. Bull.* **2014,** *83* (1), 9-23.

204. Kvenvolden, K. A.; Cooper, C. K., Natural seepage of crude oil into the marine environment. *Geo-Mar. Lett.* **2003,** *23* (3), 140-146.

205. Blumer, M., Submarine Seeps: Are They a Major Source of Open Ocean Oil Pollution? *Science* **1972,** *176* (4040), 1257-1258.

206. Kujawinski, E. B.; Kido Soule, M. C.; Valentine, D. L.; Boysen, A. K.; Longnecker, K.; Redmond, M. C., Fate of Dispersants Associated with the Deepwater Horizon Oil Spill. *Environ. Sci. Technol.* **2011,** *45* (4), 1298-1306.

207. Pedrotti, M. L.; Petit, S.; Elineau, A.; Bruzaud, S.; Crebassa, J.-C.; Dumontet, B.; Martí, E.; Gorsky, G.; Cózar, A., Changes in the floating plastic pollution of the Mediterranean Sea in relation to the distance to land. *PloS one* **2016,** *11* (8), e0161581.

208. Su, L.; Li, R.; Khan, S.; Clanton, R.; Zhang, F.; Lin, Y.-N.; Song, Y.; Wang, H.; Fan, J.; Hernandez, S., Chemical Design of Both a Glutathione-Sensitive Dimeric Drug Guest and a Glucose-Derived Nanocarrier Host to Achieve Enhanced Osteosarcoma Lung Metastatic Anticancer Selectivity. *J. Am. Chem. Soc.* **2018,** *140* (4), 1438-1446.

209. Lin, Y.-N.; Su, L.; Smolen, J.; Li, R.; Song, Y.; Wang, H.; Dong, M.; Wooley, K. L., Co-Assembly of Sugar-Based Amphiphilic Block Polymers to Achieve Nanoparticles with Tunable Morphology, Size, Surface Charge, and Acid-Responsive Behavior. *Mater. Chem. Front.* **2018,** *2* (12), 2230-2238.

210. Lohmeijer, B. G. G.; Pratt, R. C.; Leibfarth, F.; Logan, J. W.; Long, D. A.; Dove, A. P.; Nederberg, F.; Choi, J.; Wade, C.; Waymouth, R. M.; Hedrick, J. L., Guanidine and Amidine Organocatalysts for Ring-Opening Polymerization of Cyclic Esters. *Macromolecules* **2006,** *39* (25), 8574-8583.

211. Pratt, R. C.; Lohmeijer, B. G. G.; Long, D. A.; Waymouth, R. M.; Hedrick, J. L., Triazabicyclodecene: A Simple Bifunctional Organocatalyst for Acyl Transfer and Ring-Opening Polymerization of Cyclic Esters. *J. Am. Chem. Soc.* **2006,** *128* (14), 4556-4557.

212. Maikawa, C. L.; Sevit, A.; Lin, B.; Wallstrom, R. J.; Mann, J. L.; Yu, A. C.; Waymouth, R. M.; Appel, E. A., Block copolymer composition drives function of self-assembled nanoparticles for delivery of small-molecule cargo. *J. Polym. Sci., Part A: Polym. Chem.* **2019,** *57* (12), 1322-1332.

213. Su, L.; Khan, S.; Fan, J.; Lin, Y.-N.; Wang, H.; Gustafson, T. P.; Zhang, F.; Wooley, K. L., Functional Sugar-Based Polymers and Nanostructures Comprised of Degradable Poly(ᴅ-Glucose Carbonate)s. *Polym. Chem.* **2017,** *8* (10), 1699-1707.

214. Gregory, G. L.; López-Vidal, E. M.; Buchard, A., Polymers From Sugars: Cyclic Monomer Synthesis, Ring-Opening Polymerisation, Material Properties and Applications. *Chem. Commun.* **2017,** *53* (14), 2198-2217.

215. McGuire, T. M.; López-Vidal, E. M.; Gregory, G. L.; Buchard, A., Synthesis of 5- to 8-membered cyclic carbonates from diols and CO2: A one-step, atmospheric pressure and ambient temperature procedure. *J. CO_2 Util.* **2018,** *27*, 283-288.

216. Gregory, G. L.; Kociok-Köhn, G.; Buchard, A., Polymers from sugars and CO 2: ring-opening polymerisation and copolymerisation of cyclic carbonates derived from 2-deoxy-d-ribose. *Polym. Chem.* **2017,** *8* (13), 2093-2104.

217. Shen, Y.; Chen, X.; Gross, R. A., Polycarbonates from Sugars: ring-opening polymerization of 1, 2-O-isopropylidene-d-xylofuranose-3, 5-cyclic carbonate (IPXTC). *Macromolecules* **1999,** *32* (8), 2799-2802.

218. Pati, D.; Feng, X.; Hadjichristidis, N.; Gnanou, Y., Hydrophobic, Hydrophilic, and Amphiphilic Polyglycocarbonates with Linear and Macrocyclic Architectures from Bicyclic Glycocarbonates Derived from CO2 and Glucoside. *Macromolecules* **2017,** *50* (4), 1362-1370.

219. Beharaj, A.; McCaslin, E. Z.; Blessing, W. A.; Grinstaff, M. W., Sustainable polycarbonate adhesives for dry and aqueous conditions with thermoresponsive properties. *Nat. Commun.* **2019,** *10* (1), 5478.

220. Fanjul-Mosteirín, N.; Jehanno, C.; Ruipérez, F.; Sardon, H.; Dove, A. P., Rational Study of DBU Salts for the CO2 Insertion into Epoxides for the Synthesis of Cyclic Carbonates. *ACS Sustainable Chem. Eng.* **2019,** *7* (12), 10633-10640.

221. Sun, S.; Zeng, H.; Robinson, D. B.; Raoux, S.; Rice, P. M.; Wang, S. X.; Li, G., Monodisperse MFe_2O_4 (M = Fe, Co, Mn) Nanoparticles. *J. Am. Chem. Soc.* **2004,** *126* (1), 273-279.

222. Chen, L. X.; Liu, T.; Thurnauer, M. C.; Csencsits, R.; Rajh, T., Fe_2O_3 Nanoparticle Structures Investigated by X-Ray Absorption Near-Edge Structure, Surface Modifications, and Model Calculations. *J. Phys. Chem. B* **2002,** *106* (34), 8539-8546.

223. Xu, C.; Xu, K.; Gu, H.; Zheng, R.; Liu, H.; Zhang, X.; Guo, Z.; Xu, B., Dopamine as a Robust Anchor to Immobilize Functional Molecules on the Iron Oxide Shell of Magnetic Nanoparticles. *J. Am. Chem. Soc.* **2004,** *126* (32), 9938-9939.

224. Schmidt, G.; Hamaker, B. R.; Wilker, J. J., High Strength Adhesives from Catechol Cross-Linking of Zein Protein and Plant Phenolics. *Adv. Sustainable Syst.* **2018,** *2* (3), 1700159.

225. Kolb, H. C.; Finn, M. G.; Sharpless, K. B., Click Chemistry: Diverse Chemical Function from a Few Good Reactions. *Angew. Chem. Int. Ed.* **2001,** *40* (11), 2004-2021.

226. Hoyle, C. E.; Lee, T. Y.; Roper, T., Thiol–enes: Chemistry of the past with promise for the future. *J. Polym. Sci., Part A: Polym. Chem.* **2004,** *42* (21), 5301-5338.

227. Killops, K. L.; Campos, L. M.; Hawker, C. J., Robust, Efficient, and Orthogonal Synthesis of Dendrimers via Thiol-ene “Click” Chemistry. *J. Am. Chem. Soc.* **2008,** *130* (15), 5062-5064.

228. Bao, N.; Shen, L.; Wang, Y.; Padhan, P.; Gupta, A., A Facile Thermolysis Route to Monodisperse Ferrite Nanocrystals. *J. Am. Chem. Soc.* **2007,** *129* (41), 12374-12375.

229. Li, Z.; Davidson-Rozenfeld, G.; Vázquez-González, M.; Fadeev, M.; Zhang, J.; Tian, H.; Willner, I., Multi-triggered Supramolecular DNA/Bipyridinium Dithienylethene Hydrogels Driven by Light, Redox, and Chemical Stimuli for Shape-Memory and Self-Healing Applications. *J. Am. Chem. Soc.* **2018,** *140* (50), 17691-17701.

230. Kim, B.-S.; Qiu, J.-M.; Wang, J.-P.; Taton, T. A., Magnetomicelles: Composite Nanostructures from Magnetic Nanoparticles and Cross-Linked Amphiphilic Block Copolymers. *Nano Lett.* **2005,** *5* (10), 1987-1991.

231. Beltran-Villegas, D. J.; Jayaraman, A., Assembly of Amphiphilic Block Copolymers and Nanoparticles in Solution: Coarse-Grained Molecular Simulation Study. *J. Chem. Eng. Data* **2018,** *63* (7), 2351-2367.

232. Yan, L.-T.; Xie, X.-M., Computational modeling and simulation of nanoparticle self-assembly in polymeric systems: Structures, properties and external field effects. *Prog. Polym. Sci.* **2013,** *38* (2), 369-405.

233. Lehr, B.; Bristol, S.; Possolo, A. Oil Budget Calculator: Deepwater Horizon. https://www.restorethegulf.gov/sites/default/files/documents/pdf/OilBudgetCalc_Full_HQ-Print_111110.pdf (accessed 11/2/2019).

234. (NOAA), N. O. a. A. A. Climate Data Online Search. https://www.climate.gov/maps-data/dataset/past-weather-zip-code-data-table (accessed 11/4/2019).

235. Barnes, I.; Bastian, V.; Becker, K. H.; Fink, E. H.; Nelsen, W., Oxidation of Sulphur Compounds in the Atmosphere: I. Rate Constants of OH Radical Reactions with Sulphur Dioxide, Hydrogen Sulphide, Aliphatic Thiols and Thiophenol. *J. Atmos. Chem.* **1986,** *4* (4), 445-466.

236. Schoeneich, C.; Aced, A.; Asmus, K. D., Mechanism of Oxidation of Aliphatic Thioethers to Sulfoxides by Hydroxyl Radicals. the Importance of Molecular Oxygen. *J. Am. Chem. Soc.* **1993,** *115* (24), 11376-11383.

237. Warner, N. R.; Christie, C. A.; Jackson, R. B.; Vengosh, A., Impacts of Shale Gas Wastewater Disposal on Water Quality in Western Pennsylvania. *Environ. Sci. Technol.* **2013,** *47* (20), 11849-11857.